JOURNAL OF THE

AERONAUTICAL SCIENCES

VOLUME 25 FEBRUARY, 1958 NUMBER 2

ST. LOUIS
FEB 5 1958
PUBLIC LIBRARY

CONTENTS

Theory of Stagnation Point Heat Transfer in Dissociated Air
J. A. FAY AND F. R. RIDDELL 73

Stagnation Point Heat-Transfer Measurements in Dissociated Air
P. H. ROSE AND W. I. STARK 86

Analysis of Elliptical Rings for Monocoque Fuselages STANLEY KAUFMAN 98

The Effects of Afterbody Length and Mach Number on the Normal Force and Center of Pressure of Conical and Ogival Nose Bodies WILLIAM E. BUFORD 103

On the Numerical Calculation of Detached Bow Shock Waves in Hypersonic Flow
P. R. GARABEDIAN AND H. M. LIEBERSTEIN 109

Effect of Quasi-Steady Air Forces on Incompressible Bending-Torsion Flutter
J. DUGUNDJI 119

An Investigation of Two-Dimensional Supersonic Base Pressures
A. F. CHARWAT AND J. K. YAKURA 122

Readers' Forum 129

Published by
INSTITUTE OF THE AERONAUTICAL SCIENCES, INC.

JOURNAL OF THE AERONAUTICAL SCIENCES

Editor: W. R. Sears
Director, Graduate School of Aeronautical Engineering, Cornell University

Associate Editor: Robert R. Dexter *Managing Editor:* Rita J. Turino
Editorial Assistant: Caroline Taylor

Editorial Committee

Aerodynamics and Fluid Mechanics

Holt Ashley
H. Julian Allen
Dean R. Chapman
Francis H. Clauser
Hugh L. Dryden
John C. Evvard
Antonio Ferri
Alexander Flax
Wallace D. Hayes
R. T. Jones
Carl Kaplan
H. W. Liepmann
C. C. Lin
H. F. Ludloff
Harold Luskin
Clark B. Millikan
Henry T. Nagamatsu
H. J. E. Reid
George S. Schairer
G. B. Schubauer
John Stack
Theodore Theodorsen
Arthur N. Tifford
Th. von Kármán

Flight Testing

R. R. Gilruth
Melvin N. Gough
W. L. Howland
W. F. Milliken, Jr.

Rotating Wing Aircraft

F. B. Gustafson
K. H. Hohenemser
Bartram Kelley
R. B. Maloy
Ralph McClarren
R. H. Miller
R. H. Prewitt
Igor I. Sikorsky

Structures

John E. Duberg
R. R. Heldenfels
N. J. Hoff
Samuel Levy
J. F. McBrearty
W. Ramberg
E. E. Sechler
F. R. Shanley
C. R. Strang
S. Timoshenko

Meteorology

C. F. Brooks
D. M. Little
F. W. Reichelderfer
K. C. Spengler

Vibration and Flutter

Lee Arnold
M. A. Biot
R. L. Bisplinghoff
Harold A. Cheilek
I. E. Garrick
Martin Goland

Aircraft Design

W. E. Beall
E. H. Heinemann
Hall L. Hibbard
Richard Hutton
C. L. Johnson
A. A. Kartveli
F. K. Teichmann

Electronics

K. C. Black
M. V. Kiebert, Jr.
David S. Little
Paul Rosenberg
Giles J. Strickroth

Physiologic Problems

H. G. Armstrong
Louis H. Bauer
Robert J. Benford
W. Randolph Lovelace, II
Ross A. MacFarland

Flight Propulsion

William Bollay
George W. Brady
R. P. Kroon
Frank E. Marble
Abe Silverstein
E. S. Taylor

Instruments

Alan G. Binnie
Charles H. Colvin
Frank R. Cook
C. S. Draper
S. G. Eskin
C. F. Savage
R. C. Sylvander

SUBSCRIPTION RATES

Journal of the Aeronautical Sciences, Published Monthly. United States and Possessions: 1 Year, $15.00; Single Copies, $1.50. Foreign Countries Including Canada (American Currency Rates): 1 Year, $16.00; Single Copies, $1.50.

Aeronautical Engineering Review, Published Monthly. United States and Possessions: 1 Year, $5.00; Single Copies, $0.50. Foreign Countries Including Canada (American Currency Rates): 1 Year, $6.00; Single Copies, $0.50.

Notices of change of address should be sent to the Institute at least 30 days prior to actual change of address.

Manuscripts for publication, proofs, and all correspondence should be addressed to the Editorial Office of the Journal.

Publication Office, 20th and Northampton Sts., Easton, Pa. Correspondence regarding subscriptions may be addressed to the Editorial Office of the Journal of the Aeronautical Sciences, 2 East 64th Street, New York 21, N.Y.

© *Copyright, 1958, by the Institute of the Aeronautical Sciences, Inc.*

Second-Class Mail Privileges Authorized at Easton, Penna. Acceptance for mailing at a special rate of Postage provided for in the Act of August 24, 1912. Authorized April 29, 1937.

JOURNAL OF THE AERONAUTICAL SCIENCES

VOLUME 25 FEBRUARY, 1958 NUMBER 2

Theory of Stagnation Point Heat Transfer in Dissociated Air†

J. A. FAY* AND F. R. RIDDELL**

Avco Research Laboratory

SUMMARY

The boundary-layer equations are developed in general for the case of very high speed flight where the external flow is in a dissociated state. In particular the effects of diffusion and of atom recombination in the boundary layer are included. It is shown that at the stagnation point the equations can be reduced exactly to a set of nonlinear ordinary differential equations even when the chemical reactions proceed so slowly that the boundary layer is not in thermochemical equilibrium.

Two methods of numerical solution of these stagnation point equations are presented, one for the equilibrium case and the other for the nonequilibrium case. Numerical results are correlated in terms of the parameters entering the numerical formulation so as not to depend critically on the physical assumptions made.

For the nonequilibrium boundary layer, both catalytic (to atom recombination) and noncatalytic wall surfaces are considered. A solution is represented which shows the transition from the "frozen" boundary layer (very slow recombination rates) to the equilibrium boundary layer (fast recombination rates). A recombination rate parameter is introduced to interpret the nonequilibrium results, and it is shown that a scale factor is involved in relating the equilibrium state of a boundary layer on bodies of different sizes.

It is concluded that the heat transfer through the equilibrium stagnation point boundary layer can be computed accurately by a simple correlation formula [see Eq. (63)] and that the heat transfer is almost unaffected by a nonequilibrium state of the boundary layer provided the wall is catalytic and the Lewis Number near unity.

Received May 14, 1957.

† This work was sponsored by the Ballistic Missile Division, ARDC, USAF, under Contract AF 04(645)-18. Many members of the staff of the Avco Research Laboratory have contributed to this paper. In particular, thanks are due to A. R. Kantrowitz, who initiated the work, and to N. H. Kemp, who meticulously reviewed the results and suggested several improvements.

In carrying out the computations the work of D. Goldberg, R. D. Laubner, J. Levin, and W. M. Wolf is gratefully acknowledged.

* Consultant, Avco Research Laboratory, and Professor, Department of Mechanical Engineering, Massachusetts Institute of Technology.

** Principal Research Scientist.

SYMBOLS

c_i	=	mass fraction of component i
c_{pi}	=	specific heat per unit mass at constant pressure of component i, Eq. (19)
c	=	$\bar{c}_p/\bar{c}_{pw}$, Eq. (A-11)
$\bar{c}_p$		defined by Eq. (19)
C_1	=	recombination rate parameter, Eq. (57)
C_2	=	$h_D/\bar{c}_{pw}T_s$
C_3		defined by Eq. (A-14)
d		defined by Eqs. (A-4), and (A-7)
D	=	diffusion coefficient
D^T	=	thermal diffusion coefficient
e		defined by Eq. (A-13)
e_i	=	internal energy per unit mass of component i
f		defined by Eq. (24)
F		defined by Eq. (A-9)
g		defined by Eq. (25)
h	=	enthalpy per unit mass of mixture, Eq. (16)
h_i	=	perfect gas enthalpy per unit mass of component i, Eq. (10)
h_i^0	=	heat evolved in the formation of component i at 0°K. per unit mass
h_A^0	=	dissociation energy per unit mass of atomic products, Eq. (59)
h_D	=	average atomic dissociation energy times atom mass fraction in external flow, Eq. (61)
k	=	thermal conductivity
K_1	=	recombination rate constant, Eq. (50)
K_2	=	dissociation rate constant, Eq. (51)
l		defined by Eqs. (33), (A-5), and (A-9)
L_i	=	$D_i\rho\bar{c}_p/k$, Lewis Number
L_i^T	=	$D_i^T\rho\bar{c}_p/k$, thermal Lewis Number
L	=	Lewis Number for atom-molecule mixture
M	=	molecular weight of molecules in atom-molecule mixture
N	=	number density, moles per unit volume
Nu	=	Nusselt Number, Eq. (43)
p	=	pressure
q	=	heat flux
$\vec{q}$	=	vector mass velocity
$\vec{q_i}$	=	vector diffusion velocity, Eq. (2)
r	=	cylindrical radius of body
R	=	body nose radius
Re	=	Reynolds Numbers, Eq. (44)

R_i = gas constant of component i
R_m = gas constant of mixture
$\mathfrak{R}$ = universal gas constant
s defined by Eq. (27)
T = absolute temperature
T_V = vibrational temperature for molecules, taken as 800° K.
u = x component of velocity
v = y component of velocity
w_i = mass rate of formation of component i per unit volume and time
x = distance along meridian profile
y = distance normal to the surface
α_1, α_2 defined by Eq. (A-5)
β_1, β_2 defined by Eq. (A-7)
γ_1, γ_2 defined by Eq. (A 6)
η defined by Eq. (22)
θ defined by Eq. (26)
μ = absolute viscosity
ν = kinematic viscosity
ξ defined by Eq. (23)
ρ = mass density
σ = Prandtl Number $\bar{c}_p\mu/k$, taken as 0.71 in numerical calculations
Φ = dissipation function

Subscripts

A = atom
i = ith component of mixture
e = external flow conditions
w = wall
s = stagnation point in external flow
M = molecule
m = mixture
E = equilibrium

(1) Introduction

The process of aerodynamic heat transfer at hypersonic velocities is complicated by two features not normally present at low velocities. The first is the possible dissociation and ionization of air due to high static temperatures encountered where the air is decelerated by shock waves, by viscous forces in the boundary layer, or at a stagnation point. Because dissociation and ionization (and their reverse processes, recombination) proceed at finite rates, thermochemical equilibrium is not necessarily achieved throughout the flow field, and such rates are therefore an essential ingredient of the flow process. Secondly, diffusion of atoms and ions, which subsequently recombine with a high specific energy release, may appreciably add to the heat transferred by normal molecular conduction. While there may be other physical phenomena also present, such as radiative effects, it is the purpose of the present analysis to include only the two effects previously noted in an otherwise classical viscous flow problem.

Some aspects of this problem have already received attention. Moore[1] considered a dissociated laminar boundary layer on a flate plate in air with a local composition determined by the thermochemical equilibrium—i.e., a recombination rate constant sufficiently great to maintain local equilibrium. Hansen[2] noted that Moore had miscalculated the Prandtl Number for dissociated air and an analysis similar to Moore's but following Hansen's suggestion was made by Romig and Dore.[3] Beckwith[4] considered the heat transfer to the stagnation region of a blunt nosed body, using integral methods.* Crown[5] also considered the stagnation point problem, using a modified Crocco method for solving the boundary-layer equations. Finally, Mark[6] treated the stagnation point equilibrium boundary layer with variable fluid properties.†

In all these analyses no detailed distinction is made between the roles of atomic diffusion and molecular conduction in transporting energy to the wall.‡ If one considers the energy transport through a motionless dissociated gas with temperature and concentration gradients, the energy flux is approximately

$$q = k \text{ grad } T + h_A{}^0 D\rho \text{ grad } c_A$$

where k is the ordinary thermal conductivity, T is the temperature, $h_A{}^0$ is the dissociation energy per unit mass of atomic products, D is the atomic diffusion coefficient, ρ the density, and c_A the atomic mass fraction. The first term is the usual transport of kinetic, vibrational and rotational energy and the second is the transport of potential (recombination) energy. Even in the "equilibrium" boundary layer, the latter term should be taken into account in the energy equation, and will constitute a significant contribution where the atom concentration and diffusional velocities are noticeable.

These distinctions were first pointed out by Fay.[11] Subsequently, Lees[7] considered in detail the laminar heat-transfer problem in dissociated air, including the effects of atomic diffusion, and suggested several approximations to facilitate the solution of the boundary-layer equations. He considered the limiting extremes of the recombination rate constant which (as discussed below) lead to simpler solutions than the general case, and suggested expressions for the heat transfer for both cases. Similar arguments, but in less detail, are advanced by Kuo.[14]

Apart from the physical mechanism of heat transfer, there are several relevant aerodynamic considerations, the foremost of which is the question of shock-wave boundary-layer interaction at a sharp leading edge. From a mechanical point of view, it does not appear possible to maintain sharp leading edges with their attendant high heat-transfer rates, so that a finite radius of curvature appears mandatory. Under these conditions a distinct layer will exist independent of the detached bow shock wave if the boundary-layer thickness is much less than the shock detachment distance.

* It is noted that the variation of viscosity through the boundary layer, which materially affects the heat-transfer rate, cannot be accounted for by the integral method.

† For a more detailed discussion of numerical results, see Fay, Riddell, and Kemp.[12]

‡ Crown,[5] for example, assumes that the potential energy of dissociation (which is actually carried by diffusion of atoms) is transported in the same manner as the internal energy of the molecules, which implies equal diffusivities of molecules and atoms.

Since the former varies as the inverse square root of the Reynolds Number and the latter is independent of Reynolds Number, there is a minimum Reynolds Number below which the shock wave and boundary layer merge. However, since low Reynolds Numbers at hypersonic velocities can only be attained by reducing the density (and hence increasing the mean free path), this limit may not be reached before free molecule flow ensues. It thus appears that stagnation point boundary layers are quite relevant to hypersonic continuum flows.

Boundary layers at locations other than the stagnation point are also of interest, but will not be considered herein in detail. There are certain difficulties inherent in such solutions when the recombination rate is finite which will be discussed more fully below.

For any boundary-layer calculation, the behavior of the free stream outside the boundary layer must be known. If the boundary-layer thickness is small compared with the nose (and also detached shock wave) radius of curvature, then only fluid which has passed through the normal shock wave close to the axis (or plane) of symmetry will enter the boundary layer, and this constitutes the "free stream." If it is assumed that this stream has attained thermochemical equilibrium by the time it reaches the stagnation point, then the free-stream conditions for the stagnation point boundary layer are those of an equilibrium gas. This would appear to be the case most likely to be encountered.*

Whether the free stream in regions other than the stagnation point remains at equilibrium again depends upon the recombination rate since, in flowing to regions of lower pressure, the gas is expanded and cooled. Again, there will be no general solution which will include all possible situations.

The two extremes of recombination rate give rise to simpler solutions than the general case. For sufficiently small recombination rate, the concentration of atoms (or ion pairs) is determined by the diffusive flow from the free stream to the wall where recombination would occur, and would bear no relation to the thermochemical equilibrium concentration corresponding to the local temperature. In such a "frozen" boundary layer, the temperature and concentration distributions are practically independent of one another. On the other hand, for a sufficiently large recombination rate, constant thermochemical equilibrium would prevail throughout and either the temperature or concentration distribution is a sufficient description of the thermodynamic state of the boundary layer. It is, therefore, to be expected that the distribution of atoms in the "frozen" and "equilibrium" boundary layers will be quite different.

Despite the importance of the processes of dissociation and recombination in determining the thermodynamic state of the air throughout the flow field, their effect on heat transfer is secondary. This is most easily seen by again considering the heat flux through a stagnant gas as given above, and replacing grad T by $(1/c_p)$ grad h, where h is the perfect gas enthalpy. If we also make the approximation that $D\rho c_p/k$ (Lewis number) is unity, the heat flux becomes

$$q = (k/c_p) \text{ grad } (h + c_A h_A^0)$$

that is, the heat flux is determined by the chemical enthalpy (perfect gas enthalpy plus enthalpy of formation) difference between free stream and wall. Whether atoms recombine in the boundary layer or on the wall makes no great difference since the energy is conducted about as readily by normal conduction as by diffusion when the Lewis Number is approximately one. On the other hand, if the heat transfer is to be known more exactly, then such relevant effects as variation of transport coefficients with temperature, variation in heat capacities, actual Lewis Number, etc., must be accounted for properly. It will be seen that it is the influence of these effects which constitutes the principal departure from an extrapolation of the classical theory.

Since a considerable fraction of the heat may be transported by atomic diffusion toward the wall followed by recombination on the surface, it would be possible to eliminate this fraction of the heat transfer by using a noncatalytic surface. However, such a scheme is useful only if the atoms do not first recombine in the gas before reaching the wall. The flight conditions under with the gas phase recombination is slow enough to permit atoms to reach the wall, and the resulting heat transfer with both catalytic and noncatalytic surface, have been determined for the stagnation point flow.

For a discussion of experimental techniques and results of shock tube measurements of stagnation point heat transfer in dissociated air, see reference 15.

(2) Laminar Boundary-Layer Equations in a Dissociated Gas

The general equation of continuity for any species i is

$$\text{div}\{\rho(\vec{q} + \vec{q}_i)c_i\} = w_i \qquad (1)$$

where ρ is the mixture density, c_i is the mass fraction of species i, w_i is the mass rate of formation of species i per unit volume, $\vec{q}$ is the mass averaged velocity and q_i the diffusional velocity of species i measured with respect to $\vec{q}$. $\vec{q}_i$ may be given by

$$\vec{q}_i = -(D_i/c_i) \text{ grad } c_i - (D_i^T/T) \text{ grad } T \qquad (2)$$

where D_i and D_i^T are, respectively, the molecular and thermal diffusion coefficients of species i, and T is the temperature. The first term on the right of Eq. (2) is

* The time for the gas to come to equilibrium behind the normal shock wave depends upon the kinetics of the dissociation process. It is merely noted here that immediately behind the shock wave, before dissociation begins, the translational temperature is extremely high and thereby promotes high dissociation rates. Even at high temperatures equilibrium may not be attained soon enough if the density is sufficiently low, but this would probably occur only near the free molecule flow regime.

due to concentration diffusion and the second is due to thermal diffusion (pressure diffusion is neglected).

The use of the gradient of mass fraction instead of mole fraction is particularly useful since, in the case of a bimolecular mixture, D_i becomes the bimolecular diffusion coefficient (D_{12}) which is practically independent of composition. For multicomponent mixtures, the diffusional velocity of any one component depends, in general, upon the concentration gradients of all the components, and a method for determining the diffusional velocities has been suggested by Hirschfelder, Curtiss, and Bird.[8] In such a case Eq. (2) is not exact (except for equal diffusivities and molecular weights of all components), but is a useful approximation. A dissociated gas (such as air) in which all the molecules (or atoms) have nearly the same molecular weight and probably similar collision diameters may be considered primarily a two-component mixture with atoms and molecules as species, for which Eq. (2) is adequate.

In order to conserve mass in any chemical change it is necessary that

$$\Sigma w_i = 0 \tag{3}$$

and from the definition of the mass averaged velocity it follows that

$$\Sigma \vec{q_i} c_i = 0 \tag{4}$$

Hence, Eq. (1) summed over all species gives the usual form for the continuity equation,

$$\text{div}\,(\rho \vec{q}) = 0 \tag{5}$$

The energy equation may be written for a moving element of fluid

$$\rho \vec{q} \cdot \text{grad}(\Sigma c_i e_i) = \text{div}(k\ \text{grad}\ T) - \text{div}(\Sigma \rho \vec{q}_i c_i h_i) + \Sigma w_i h_i^0 + p\ \text{div}\ \vec{q} + \Phi \tag{6}$$

where e_i, h_i, and h_i^0 are, respectively, the specific internal energy, enthalpy, and heat of formation of species i, k is the thermal conductivity for transport of kinetic, rotational, and vibrational energy, p is the pressure, and Φ is the dissipation function.

The first term on the right of Eq. (6) is the internal energy increase due to normal heat conduction, the second that due to fluid diffusing across the boundary of the element, the third that due to chemical reaction,* and the fourth and fifth that due to the work of the pressure and the viscous forces, respectively.

It will be assumed that the gas is a mixture of perfect gases, so that for each component

$$p_i = \rho_i R_i T \tag{7}$$

where R_i is the gas constant for species i, and for the mixture

$$p = \rho R_m T \tag{8}$$

where the gas constant for the mixture (R_m) is given by

$$R_m = \Sigma c_i R_i \tag{9}$$

It then follows that the enthalpy and internal energy are related by

$$h_i = e_i + R_i T \tag{10}$$

By combining Eqs. (5) and (7) through Eq. (10) with Eq. (6), the steady-state energy equation reduces to

$$\rho \vec{q} \cdot \text{grad}(\Sigma c_i h_i) = \text{div}(k\ \text{grad}\ T - \Sigma \rho \vec{q_i} c_i h_i) + \Sigma w_i h_i^0 + \vec{q} \cdot \text{grad}\ p + \Phi \tag{11}$$

A further simplification occurs by combining Eqs. (1) and (11) to eliminate the term $\Sigma w_i h_i^0$:

$$\rho \vec{q} \cdot \text{grad}\{\Sigma c_i (h_i - h_i^0)\} = \text{div}\{k\ \text{grad}\ T - \Sigma \rho \vec{q_i} c_i (h_i - h_i^0)\} + \vec{q} \cdot \text{grad}\ p + \Phi \tag{12}$$

By making the usual boundary-layer assumptions Eqs. (1), (5), and (12) reduce to the following form for a body of revolution, if the boundary-layer thickness is small compared with the radius of curvature and centrifugal forces are neglected:†

$$(\rho r u)_x + (\rho r v)_y = 0 \tag{13}$$

$$\rho u c_{ix} + \rho v c_{iy} = \{D_i \rho c_{iy} + D_i^T \rho c_i T_y / T\}_y + w_i \tag{14}$$

$$\rho u h_x + \rho v h_y = (kT_y)_y + u p_x + \mu (u_y)^2 + \{\Sigma D_i \rho (h_i - h_i^0) c_{iy} + \Sigma D_i^T \rho c_i (h_i - h_i^0) T_y / T\}_y \tag{15}$$

where r is the radial distance of the body surface from the axis of revolution, u and v are the velocity components in the x and y directions (tangential and normal to the surface, respectively), μ is the absolute viscosity and the enthalpy for the mixture is

$$h = \Sigma c_i (h_i - h_i^0) \tag{16}$$

The corresponding equation of motion is

$$\rho u u_x + \rho v u_y = -p_x + (\mu u_y)_y \tag{17}$$

Since the transport coefficients are, in general, functions of temperature and composition, it may be desirable to use T rather than h as the dependent variable in the energy equation. Noting that h_i is a function of temperature alone, we have

$$\text{grad}\ h = \{\Sigma c_i (dh_i/dT)\}\ \text{grad}\ T + \Sigma (h_i - h_i^0)\ \text{grad}\ c_i \tag{18}$$

Letting

$$\bar{c}_p \equiv \Sigma c_i (dh_i/dT) = \Sigma c_i c_{pi} \tag{19}$$

where c_{pi} is the constant pressure specific heat for translation, rotation, and vibration, the energy equation (15), in combination with Eq. (14), becomes

$$\bar{c}_p \{\rho u T_x + \rho v T_y\} = (kT_y)_y + u p_x + \mu (u_y)^2 + \Sigma w_i (h_i^0 - h_i) + \Sigma c_{pi} (D_i \rho c_{iy} + D_i^T \rho c_i T_y / T) T_y \tag{20}$$

For a gas at equilibrium, on the other hand, it is found

* The heat of formation h_i^0 may be taken as zero for the molecules and negative for the atoms, in which case the enthalpy h [see Eq. (16)] is always positive.

† Subscripts x and y (or ξ and η below) are used to denote partial differentiation.

more convenient to use the enthalpy as a variable rather than temperature, in which case by combining Eqs. (17) and (18) with Eq. (15), we obtain

$$\rho u(h + u^2/2)_x + \rho v(h + u^2/2)_y = \{(k/\bar{c}_p) \times (h + u^2/2)_y\}_y + \{(1/2)[\mu - (k/\bar{c}_p)](u^2)_y\}_y + \{\Sigma[D_i\rho - (k/\bar{c}_p)](h_i - h_i^0)c_{iy}\} + \Sigma(D_i^T\rho c_i/T)(h_i - h_i^0)T_y\}_y \quad (21)$$

Eqs. (13), (14), (17), and (20) or (21) thus constitute the system whose solution is required.

(3) Similar Solutions

As is usual in boundary-layer problems, one first seeks solutions of restricted form which permit reducing exactly the partial differential equations to ordinary differential form. An easily recognizable case is that of the stagnation point flow, where, because of symmetry, all the dependent variables are chosen to be functions of y alone, except u which must be taken proportional to x times a function of y. This also appears to be the *only case* for which exact ordinary differential equations may be obtained regardless of the recombination rate. For the flat plate and cone, exact solutions exist only for the extreme values of the recombination rate constant, that is, when the boundary layer is either "frozen" or in the thermodynamic equilibrium.

For all other cases, certain degrees of approximation are required. Following standard procedures, one first tries solutions for which the velocity and enthalpy profiles remain similar to themselves, at least for an appreciable distance along the body. Such "locally similar" approximate solutions may be obtained for the "frozen" or "equilibrium" boundary layer, and also for an arbitary recombination rate in certain restricted cases.

The existence of a finite recombination rate is not the only hindrance to obtaining exact solutions in regions other than the stagnation point. In general, the variation of the velocity, thermodynamic variables and transport coefficients in the free stream and along the wall of the body of arbitrary shape preclude exact solutions (except for the cone and flat plate). An important aspect of the locally similar solutions is a proper accounting for these variations such that the heat transfer may be determined for any point of the body of arbitrary (but regular) shape. Although this problem will not be treated in this paper, we will start with a transformation suitable for locally similar solutions.

With this in mind, we choose the following transformation of the independent variables x and y, which includes the usual Howarth and Mangler transformations, as proposed by Lees.[7]

$$\eta \equiv (ru_e/\sqrt{2\xi}) \int_0^y \rho dy \quad (22)^*$$

$$\xi \equiv \int_0^x \rho_w\mu_w u_e r^2 dx \quad (23)^*$$

where u_e is the velocity at the outer edge of the boundary layer. In addition, the following dimensionless dependent variables are chosen:

$$\partial f/\partial\eta \equiv u/u_e; \quad f = \int_0^\eta (\partial f/\partial\eta)d\eta \quad (24)$$

$$g = (h + u^2/2)/h_s \quad (25)$$

$$\theta = T/T_e \quad (26)$$

$$s_i = c_i/c_{ie} \quad (27)$$

where the subscript e refers to values in the local free stream, and s to values in the free stream at the stagnation point. Substituting in Eqs. (13), (14), (17), (20), and (21), there results

$$\rho v = -r^{-1}[(\sqrt{2\xi}\, f_\xi + f/\sqrt{2\xi})\xi_x + \sqrt{2\xi}\, f_y\eta_x] \quad (28)$$

$$[(l/\sigma)(L_i s_{i\eta} + L_i^T s_i\theta_\eta/\theta)]_\eta + f s_{i\eta} + [2\xi w_i/\rho u_e c_{ie}(d\xi/dx)] = 2\xi(f_\eta s_{i\xi} - f_\xi s_{i\eta}) + 2f_\eta s_i[d(\ln c_{ie})/d(\ln \xi)] \quad (29)$$

$$(lf_{\eta\eta})_\eta + ff_{\eta\eta} + 2[d(\ln u_e)/d(\ln \xi)][(\rho_e/\rho) - f_\eta^2] = 2\xi(f_\eta f_{\eta\xi} - f_\xi f_{\eta\eta}) \quad (30)$$

$$[(\bar{c}_p/\bar{c}_{pw})(l/\sigma)\theta_\eta]_\eta + (\bar{c}_p/\bar{c}_{pw})f\theta_\eta + \Sigma[2\xi w_i/\rho u_e(d\xi/dx)][(h_i^0 - h_i)/\bar{c}_{pw}T_e] + (u_e^2/\bar{c}_{pw}T_e)lf_{\eta\eta}^2 + \Sigma(c_{pi}/\bar{c}_{pw})(c_{ie}l/\sigma)(L_i s_{i\eta} + L_i^T s_i\theta_\eta/\theta)\theta_\eta = f_\eta\{2(\bar{c}_p/\bar{c}_{pw})\theta[d(\ln T_e)/d(\ln \xi)] + (2u_e^2/\bar{c}_{pw}T_e)(\rho_e/\rho)[d(\ln u_e)/d(\ln \xi)]\} + 2(\bar{c}_p/\bar{c}_{pw})\xi(f_\eta\theta_\xi - f_\xi\theta_\eta) \quad (31)$$

$$[(l/\sigma)g_\eta]_\eta + fg_\eta + (u_e^2/h_s)\{(1 - \sigma^{-1})lf_\eta f_{\eta\eta}\}_\eta + \{(l - \sigma)\Sigma(c_{ie}/h_s)(h_i - h_i^0)[(L_i - 1)s_{i\eta} + L_i^T s_i\theta_\eta/\theta]\}_\eta = 2\xi(f_\eta g_\xi - f_\xi g_\eta) \quad (32)$$

where $l \equiv \rho\mu/\rho_w\mu_w$

and where σ and L_i are the Prandtl Number $(\bar{c}_p\mu/k)$ and Lewis Number $(D_i\rho\bar{c}_p/k)$, respectively. The subscript w refers to values of the variables at the wall.

For the dependent variables f, g, θ, and s_i to be functions of η alone, it is first necessary that the thermodynamic state variables be unchanging in the free stream and along the wall as ξ increases, a condition satisfied at a stagnation point, or along a cone or flat plate. It is further necessary that the source term—i.e., the term involving w_i—in Eqs. (29) and (31) depend upon η alone. Since the chemistry of the recombination process is believed to depend only upon the local thermodynamic variables—that is, w_i is a function of ρ, T, and s_i—this second condition may be satisfied in three different ways: (a) $w_i = 0$ (frozen boundary layer), (b) $u_e d(\ln \xi)/dx$ = constant, which is satisfied at a stagnation point, or (c) the recombination rate is sufficiently

* For two-dimensional flows let r = constant.

large to maintain thermodynamic equilibrium,* in which case w_i is determined through Eq. (29) from the solution of Eqs. (28), (30), and (32).

For the stagnation point, then, Eqs. (29) to (32) reduce to

$$[(l/\sigma)(L_i s_{i\eta} + L_i^T s_i T_\eta/T)]_\eta + f s_{i\eta} + \{2(du_e/dx)_s\}^{-1}(w_i/\rho c_{is}) = 0 \quad (34)$$

$$(lf_{\eta\eta})_\eta + ff_{\eta\eta} + (1/2)\{(\rho_s/\rho) - f_\eta^2\} = 0 \quad (35)$$

$$[(\bar{c}_p/\bar{c}_{pw})(l/\sigma)]_\eta + (\bar{c}_p/\bar{c}_{pw}) f\theta_\eta + \{2(du_e/dx)_s\}^{-1}\Sigma(w_i/\rho)[(h_i^0 - h_i)/\bar{c}_{pw}T_s] + \Sigma(c_{pi}/\bar{c}_{pw})(c_{is}l/\sigma)(L_i s_{i\eta} + L_i^T s_i\theta_\eta/\theta)_\eta\theta_\eta = 0 \quad (36)$$

$$[(l/\sigma)g_\eta]_\eta + fg_\eta + \left((l/\sigma)\Sigma[c_{is}(h_i - h_i^0)/h_s]\{(L_i - 1)s_{i\eta} + L_i^T s_i\theta_\eta/\theta\}\right)_\eta = 0 \quad (37)$$

where it has been assumed that $u^2 \ll h_s$.

For a "locally similar" solution away from the stagnation point it is required that the terms on the right-hand side of Eqs. (29) through (32) all be negligible compared with those on the left, and thus the equations may be integrated with respect to η. The dependence upon ξ of f, g, θ, and s_i is thereby implicitly determined by the variation of ρ, T, s_i, u, and the transport coefficients in the free stream and along the wall, this variation being determined by the aerodynamics of the external flow.

For Newtonian flow the distribution around the body of the relevant quantities is easily found, all quantities except du_e/dx being determined by the local body slope— i.e., local pressure. Since du_e/dx depends upon the pressure gradient and hence body curvature in the meridian plane, there is introduced an extra parameter in the locally similar solutions. Lees[7] points out that in the equation of motion (30) the pressure gradient affects only a single term, that this term is generally small, and that neglecting this term in the equation of motion will only slightly affect the solutions for g, θ, and s_i. This appears to be a greatly desirable simplification in determining the heat transfer at other than the stagnation point.

The use of locally similar solutions can only be justified a posteriori in each particular case by determining from such a solution the magnitude of the terms in Eqs. (29) through (32) which were neglected. Presumably an iterative scheme could be devised to improve on such solutions. It does not appear possible to formulate a general criterion for determining the limit of applicability of the locally similar solutions except a loose physical argument that conditions in the free stream and along the body must change only slightly in a distance of many boundary-layer thicknesses.

(4) Heat Transfer

The local heat-transfer rate to the body q is determined by the sum of the conductive and diffusive transports, the latter being included only when the atoms recombine on the wall. Thus,

$$q = [k(\partial T/\partial y)]_{y=0} + [\Sigma\rho(h_i - h_i^0) \times \{D_i(\partial c_i/\partial y) + (D_i^T c_i/T)(\partial T/\partial y)\}]_{y=0} \quad (38)$$

or

$$q = [(k/\bar{c}_p)(\partial h/\partial y)]_{y=0} + [\Sigma(k/\bar{c}_p)(h_i - h_i^0) \times \{(L_i - 1)(\partial c_i/\partial y) + (L_i^T c_i/T)(\partial T/\partial y)\}]_{y=0} \quad (39)$$

In terms of the dimensionless temperature and enthalpy distributions, this becomes

$$q = (rk_w\rho_w u_e T_e/\sqrt{2\xi})\{\theta_\eta + \Sigma c_{ie} \times [(h_i - h_i^0)/\bar{c}_p T_e](L_i s_{i\eta} + L_i^T s_i\theta_\eta/\theta)\}_{\eta=0} \quad (40)$$

or

$$q = (rk_w\rho_w u_e h_s/\sqrt{2\xi}\,\bar{c}_{pw}) \times \{g_\eta + \Sigma c_{ie}[(h_i - h_i^0)/h_s] \times [(L_i - 1)s_{i\eta} + L_i^T s_i\theta_\eta/\theta]\}_{\eta=0} \quad (41)$$

For stagnation point heat transfer we note that

$$r\rho_w u_e/\sqrt{2\xi} = \{(2/\nu_w)(du_e/dx)_s\}^{1/2} \quad (42)$$

where ν_w is the kinematic viscosity at the wall.

It is also possible to define local Nusselt and Reynolds Numbers based on the local coordinate x. Thus, defining†

$$Nu = qx\bar{c}_{pw}/k_w(h_s - h_w) \quad (43)$$

$$Re = u_e x/\nu_w \quad (44)$$

the heat transfer at the stagnation point may be written as

$$q = (Nu/\sqrt{Re})\sqrt{\rho_w\mu_w(du_e/dx)_s}[(h_s - h_w)/\sigma] \quad (45)$$

where

$$Nu/\sqrt{Re} = [\sqrt{2}\,\bar{c}_{pw}T_s/(h_s - h_w)] \times \{\theta_\eta + \Sigma c_{is}[(h_i - h_i^0)/\bar{c}_p T_s] \times (L_i s_{i\eta} + L_i^T s_i\theta_\eta/\theta)\}_{\eta=0} \quad (46a)^\ddagger$$

$$Nu/\sqrt{Re} = [\sqrt{2}/(1 - g_w)] \times \{g_\eta + \Sigma c_{is}[(h_i - h_i^0)/h_s] \times [(L_i - 1)s_{i\eta} + L_i^T s_i\theta_\eta/\theta]\}_{\eta=0} \quad (46b)^\ddagger$$

It should be emphasized that the heat transfer is independent of the particular choice of reference density and viscosity ($\rho_w\mu_w$) which appears in the definition of Eq. (23). The use of wall values of ρ and μ for this pur-

* Strictly speaking, the fluid cannot be exactly in thermodynamic equilibrium, for if this were so, there could be no net rate of change of composition following a particle path. For large enough rate constants, the fluid will be very close to equilibrium.

† It is clear from the expressions (40) and (41) that the enthalpy difference between wall and free stream, not the temperature difference, is the proper "driving force" for heat transfer.

‡ For conical or flat plate flows, the factor $\sqrt{2}$ in Eq. (46) should be replaced by $\sqrt{3/2}$ or $1/\sqrt{2}$, respectively, when the reference dimensions for Nu and Re are the distances from the apex or leading edge, respectively, measured along the surface.

pose is merely a convenience, but a logical choice in that it ensures that $l = 1$ [Eq. (33)] at the wall ($\eta = 0$). However, another choice, such as free-stream ρ and μ, or even $\rho\mu$ equal to an arbitrary function of x, could also be used. In each such case, however, the solutions of the boundary-layer equations give different $g(\eta)$, $\theta(\eta)$, etc. It is clear from an examination of these equations that each such solution may be transformed into another by a simple change of scale of η and f defined by

$$\sqrt{\rho_w\mu_w}\,\eta = \sqrt{\rho_0\mu_0}\,\eta_0 \tag{47}$$

$$\sqrt{\rho_w\mu_w}\,f = \sqrt{\rho_0\mu_0}\,f_0 \tag{48}$$

and

$$g(\eta) = g_0(\sqrt{\rho_0\mu_0/\rho_w\mu_w}\,\eta_0), \quad \text{etc.} \tag{49}$$

and where $\rho_0\mu_0$ is the new reference value used in defining η_0. As a consequence the heat transfer [see Eqs. (38) and (39)] can be seen to be independent of the choice of $\rho_0\mu_0$.

On the other hand, if one attempts to estimate $g_\eta(0)$ for the case of $\rho\mu$ not constant from a solution for $\rho\mu$ constant,* which is the problem considered by Lees,[7] the reference state ($\rho_0\mu_0$) is quite relevant since by its proper (and arbitrary) selection the wall gradient of g may be made to equal numerically that for the case of $\rho\mu$ constant. A discussion of this point has been given by Probstein,[9] and by Fay, Riddell, and Kemp.[12]

(5) Transport Properties

To obtain a numerical solution of the boundary-layer equations it is necessary to know the viscosity, Prandtl Number, Lewis Number, and thermal diffusivity as functions of the local temperature, density, and composition. For the high temperatures under consideration, these properties have been estimated,† the principal uncertainty resulting from lack of knowledge of atom-molecule interaction potentials. The particular results of this study which are pertinent to the boundary-layer calculation may be summarized as follows.

(a) The viscosity of equilibrium air, determined by assuming that all particles possess the same interaction potentials, does not vary more than 10 per cent from Sutherland's formula below 9,000°K.

(b) Both Prandtl and Lewis Numbers do not change appreciably with temperature (below 9,000°K.), the value of the latter being uncertain, but estimated as about 1.4.

In light of the uncertainties in viscosity and Lewis Number, it is clear that the calculated heat transfer using these estimates is also uncertain. However, the numerical solutions of the boundary-layer equations may be obtained for a range of possible Lewis Number and viscosity variation, such solutions being generally valid when expressed explicitly in terms of the property variations. Thus for the numerical solutions, the Prandtl Number was held fixed at 0.71, the Lewis Number was assumed constant through the boundary layer at values ranging from one to two, and the viscosity variation was determined by Sutherland's law for the equilibrium air and as calculated by Penner and Litvak for nonequilibrium composition.‡

It is easily shown that thermal diffusion is unimportant for the equilibrium boundary layer at stagnation temperatures less than 10,000°K. For the frozen boundary layer this is no longer necessarily the case; however, thermal diffusion was neglected in all the numerical solutions reported in this paper.

(6) Recombination Rate

As suggested by Davidson,** the recombination rate of atoms is determined by a three-body collison:

$$\text{atom} + \text{atom} + \text{particle} \rightarrow \text{molecule} + \text{particle}$$

For this process the rate of disappearance of atoms may be written as

$$dN_A/dt = -K_1N_A^2NT^{-1.5} \tag{50}$$

where the temperature dependence is as suggested by Davidson, who also estimated $K_1T^{-1.5}$ to be 5×10^{14} cc.^{2} mole^{-2} sec.$^{-1}$ for oxygen recombination when $T = 300$°K.†† N_A and N are the number of moles per cm.^{3} of atoms and particles, respectively.

Atoms will be produced by the reverse of the above reaction, so that the net rate of production may be written as

$$dN_A/dt = -K_1N_A^2NT^{-1.5} + K_2(T)N_MN \tag{51}$$

Since under equilibrium conditions, there is no net production of atoms, $K_2(T)$ may be solved for in Eq. (51) in terms of the equilibrium atom and molecule concentrations which would exist at the local temperature T and pressure. Substituting this value of K_2 in Eq. (51), there results

$$dN_A/dt = -K_1N_A^2NT^{-1.5} \times \{1 - (N_M/N_{ME})(N_{AE}/N_A)^2\} \tag{52}$$

where the subscript E refers to the concentrations which would exist at thermodynamic equilibrium at the local pressure and temperature, and N_M is the number of moles of molecules per cm^3.

Considering a gas mixture of diatomic molecules of

---

* As, for example, the solutions of Cohen and Reshotko.[10]

† These estimates were made by Dr. S. Penner of California Institute of Technology and M. M. Litvak of Cornell University.

‡ Results of the experiments of reference 15 indicate good agreement with the present estimates of transport properties with Prandtl Number 0.71 and Lewis Number 1.4.

** Dr. Norman Davidson, California Institute of Technology (private communication).

†† Recent experiments reported by J. Camm and J. Keck (see Bulletin of the American Physical Society, Series II, Vol. 2, No. 4, p. 216, 1957) indicate that the recombination rate at 6,000°K. may be higher than that obtained by extrapolating Davidson's estimate to such a temperature. There is nothing known concerning this rate at the low wall temperatures pertinent to the boundary-layer problem.

molecular weight M and atoms of weight $M/2$, the atom mass fraction and total density are, respectively,

$$c_A = N_A/(N_A + 2N_M) \tag{53}$$

and

$$\rho = M(N_M + N_A/2) \tag{54}$$

The net mass rate of formation of atoms (w_A) may now be determined in terms of these quantities to give

$$\left.\begin{aligned} w_A &= (M/2)(dN_A/dt) \\ &= -(2K_1\rho^2T^{-1.5}/M^2) \times \\ &\quad [(1 + c_A)(c_A^2 - c_{AE}^2)/(1 - c_{AE}^2)] \end{aligned}\right\} \tag{55}$$

Neglecting the term $(1 - c_{AE}^2)$, which does not vary by 25 per cent in the cases considered, the relevant source term in the diffusion equation (34) for atoms reduces to

$$\{2(du_e/dx)_s\}^{-1}(w_i/\rho) = -[K_1p_s^2T_s^{-3.5}/\Re^2(du_e/dx)_s] \times \{\theta^{-3.5}(c_A^2 - c_{AE}^2)/(1 + c_A)\} \tag{56}$$

where $\Re$ is the universal gas constant. The coefficient of the term in braces on the right of Eq. (56) contains all the dimensional effects of the finite recombination rate problem, and will be termed the *recombination rate parameter* (C_1)—i.e.,

$$C_1 \equiv K_1p_s^2T_s^{-3.5}\Re^{-2}(du_e/dx)_s^{-1} \tag{57}$$

The term $(du_e/dx)_s^{-1}$ is approximately the time for a particle in the free stream to move a distance equal to the nose radius, and thus also the time for a particle to diffuse through the boundary layer at the stagnation point. The factor which multiplies it in Eq. (57) is the reciprocal of the lifetime of an atom, so that the recombination rate parameter is the ratio of the diffusion time to the lifetime of an atom. Because the diffusion time contains the body nose radius while the lifetime does not, a scale effect is introduced by the chemical change which is not accounted for in the Reynolds Number. Thus, similar flows require equal Reynolds Numbers and recombination rate parameters.

A term similar to the left side of Eq. (56) appears in the energy equation (36) except that it is multiplied by a dimensionless dissociation energy. A part of this term, Σw_ih_i, is negligible since $\Sigma w_i = 0$ and h_i per unit mass for vibrationally excited molecules and atoms are nearly equal, being in the ratio 9/10.

(7) Numerical Solutions

The boundary-layer equations derived above [Eqs. (34) through (37)] can be put in a form suitable for numerical integration. The details of how this was done are given in the Appendix. Numerical solutions were obtained by use of an IBM 650 digital computer.

Many combinations of the parameters σ, L, and C_1 are possible, as well as extreme ranges in the free-stream (stagnation point) and wall boundary values. It was therefore decided to restrict the solutions to the following values:

(a) $\sigma = 0.71$
(b) $L = 1.0, 1.4, 2.0; L^T = 0$
(c) $0 \leq C_1 \leq \infty$
(d) Stagnation point conditions corresponding to thermodynamic equilibrium at velocities between 5,800 ft. per sec. and 22,800 ft. per sec. and at altitudes of 25,000 ft. to 120,000 ft. (Equilibrium air properties were determined from the tables prepared by the National Bureau of Standards[11].)
(e) Wall temperatures from 300° K. to 3,000°K.

Wherever possible, only one parameter or boundary condition was varied in a series of calculations in order to determine its individual effect. It was not believed necessary to establish such effects for all possible combinations of the remaining parameters. Tables giving the values of the parameters and the boundary conditions for each computation may be obtained directly from the authors.

The heat-transfer parameter ($Nu/\sqrt{Re}$) determined from each integration depends not only upon the parameters and boundary values of the dependent variables involved, but also upon the assumed variation of viscosity with temperature and composition. In addition, further simplifications as explained below for the individual cases were also made. In order to make the results less dependent upon the specific assumptions made, the heat-transfer parameter was numerically correlated with the parameters and boundary values in what seemed to be a suitable manner. It is believed that not too widely different assumptions would give results which would fall within the same correlation.

(8) The Equilibrium Boundary Layer

A first series of equilibrium boundary layers was computed by solving Eqs. (35) and (37) simultaneously (hereafter denoted as Method 1). The solution requires specifying ρ_s/ρ and $l = \rho\mu/\rho_w\mu_w$ as functions of g, typical variations of these quantities being shown in Fig. 1. The calculated values at various altitudes of interest are compared with the fitted curves used in the computing program, from which it was concluded that there was a negligible effect of altitude variation on these functions. Specific details of the method of calculation are given in the Appendix. It was found that moderate changes in the distribution for identical end values resulted in negligible changes in the heat-transfer parameter.

For $L_l = 1$, the equations are similar in form to those solved by Cohen and Reshotko,[10] and become identical at low enough stagnation temperatures when l is approximately constant. Solutions were obtained for the range of velocities and wall temperatures given above, and the heat-transfer parameter was found to depend only upon the total variation in $\rho\mu$ across the boundary layer, in accordance with the relation

$$Nu/\sqrt{Re} = 0.67(\rho_s\mu_s/\rho_w\mu_w)^{0.4} \tag{58}$$

The numerical correlation leading to Eq. (58) is shown in Fig. 2. The solution of Cohen and Reshotko[10] for $l = 1$ is also plotted, after correcting for Prandtl Number by multiplying their result by $(0.71)^{0.4}$.

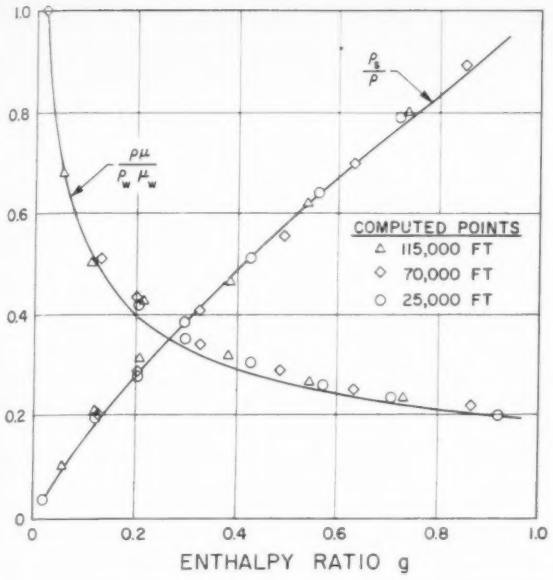

FIG. 1. Variation of $\rho\mu/\rho_w\mu_w$ and ρ_s/ρ through a stagnation point boundary layer, shown as a function of enthalpy ratio g. Stagnation conditions are for a flight velocity of 19,700 ft. per sec. at various altitudes. $T_w = 300°K$.

An alternative procedure for the equilibrium boundary layer is to solve Eqs. (34), (35) and (36) simultaneously (hereafter denoted as Method 2). An appreciable simplification results if we consider air to be composed of only "air" molecules and "air" atoms having an average heat of formation given by

$$h_A{}^0 = \sum_{\text{atoms}} c_{is}(-h_i{}^0) \Big/ \sum_{\text{atoms}} c_{is} \qquad (59)$$

where the summation extends over atomic oxygen and nitrogen only. Thus only one diffusion equation (34) is needed for the diffusion of air atoms. With this simplification the equilibrium boundary layer may be treated by eliminating the term involving w_i between Eq. (34) and (36). A solution is then possible when $\bar{c}_p$ and l are specified as functions of s_A and θ, and s_A is specified as a function of θ through the known equilibrium atom fraction as a function of temperature. (Details of the approximations made are given in the Appendix.)

This alternative solution was found to give very closely the same results as the Method 1 for a Lewis Number of unity, and the results are compared with Eq. (58) in Fig. 2. For a Lewis Number of unity, Method 2 is believed to be less accurate than Method 1, since it involves more approximations to the real gas properties.

For other values of the Lewis Number, the effect of Lewis Number on the heat-transfer parameter was found by Method 2 to be best given by

$$(Nu/\sqrt{Re})/(Nu/\sqrt{Re})_{L=1} = 1 + (L^{0.52} - 1)\,(h_D/h_s) \qquad (60)$$

where the "dissociation enthalpy" h_D is defined as

$$h_D = \sum c_{is}(-h_i{}^0) = h_A{}^0 \sum_{\text{atoms}} c_{is} \qquad (61)$$

i.e., h_D is the dissociation enthalpy per unit mass of air in the external flow. The numerical results are plotted in Fig. 3 for comparision with Eq. (60).

It was also possible to determine the effect of Lewis Number from the Method 1 computations by evaluating the additional term in Eq. (37) involving $(L - 1)$ from the equilibrium properties of air. (The approximation for this evaluation is discussed in the Appendix.) Two such cases were computed, and the results are plotted in Fig. 3 for comparison with Eq. (60). While there is some disagreement with the results of Method 2, it is not too unreasonable considering the many different approximations involved in fitting curves to the functions l, $\bar{c}_p$, etc. It is the authors' opinion that the Method 2 solutions give a better indication of the Lewis Number effect for the equilibrium boundary layer, as embodied in Eq. (60). However, for Lewis Number unity the effect of $\rho\mu$ variation is believed to be better given by the results of Method 1 [Eq. (58)], so that the total effect may be obtained by combination of Eqs. (58) and (60) in the form

$$Nu/\sqrt{Re} = 0.67(\rho_s\mu_s/\rho_w\mu_w)^{0.4} \times \{1 + (L^{0.52} - 1)(h_D/h_s)\} \qquad (62)$$

The stagnation point heat-transfer rate for $\sigma = 0.71$ thus becomes, by virtue of Eq. (45),*

$$q = 0.94(\rho_w\mu_w)^{0.1}(\rho_s\mu_s)^{0.4} \times \{1 + (L^{0.52} - 1)(h_D/h_s)\}(h_s - h_w)\sqrt{(du_e/dx)_s} \qquad (63)$$

It is interesting to note that the external flow properties are much more important than the wall values in determining the heat-transfer rate, so that the uncertainty in the heat transfer is about 40 per cent of the un-

* For σ not equal to 0.71, it is recommended that the factor 0.94 be replaced by $(0.76\,\sigma^{-0.6})$.

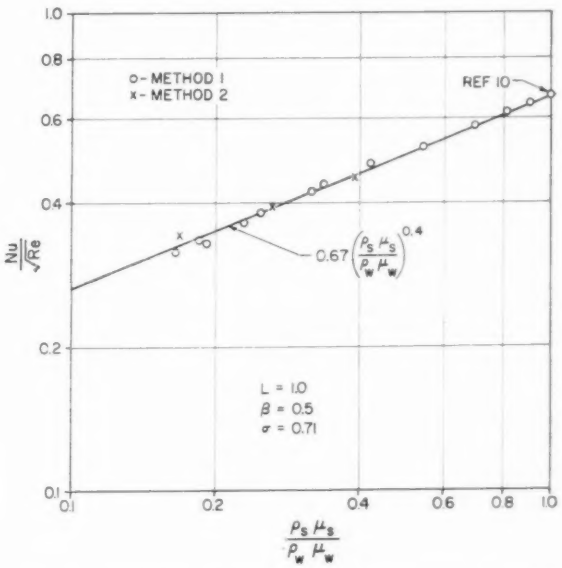

FIG. 2. Correlation of the heat-transfer parameter $Nu/\sqrt{Re}$ as a function of the $\rho\mu$ ratio across the boundary layer, $\rho_s\mu_s/\rho_w\mu_w$ for the equilibrium stagnation point boundary layer with $L = 1$.

certainty in the external viscosity. The physical reason for the importance of the external viscosity is that the growth of the boundary layer, and hence the heat transfer to the wall, depends mostly upon the external properties. The analogy with turbulent boundary layers is easily seen.

For a modified Newtonian flow, the stagnation point velocity gradient is

$$(du_e/dx)_s = (1/R)\sqrt{2(p_s - p_\infty)/\rho_s} \qquad (64)$$

where R is the nose radius and p_∞ is the ambient pressure.

(9) The "Frozen" Boundary Layer

When atomic gas phase recombination is negligible ($C_1 = 0$), atoms diffusing from the free stream will reach the wall. If the wall is *noncatalytic* to surface recombination, the atom fraction at the wall will build up to the free-stream value. On the other hand, if the wall is *catalytic*, the atom concentration will be reduced to its equilibrium value at the wall temperature. Intermediate cases of wall catalyticity are of course possible, but only these extremes were computed.

Eqs. (34), (35), and (36) were solved with $C_1 = 0$ for various stagnation conditions and Lewis Numbers as discussed in the Appendix (Method 2).

For Lewis Number unity, the effect of the $\rho\mu$ variation was very close to that found for the equilibrium boundary layer by Method 2, and could suitably be expressed by Eq. (58). For other values of L, the dependence could best be given by*

$$(Nu/\sqrt{Re})/(Nu/\sqrt{Re})_{L=1} = 1 + (L^{0.63} - 1)(h_D/h_s) \qquad (65)$$

The calculated values are compared with Eq. (65) in Fig. 4.

The difference in the exponent of L for the frozen as compared with the equilibrium boundary layer [Eqs. (60) and (65)] is quite certain since exactly the same property variations were used in both cases, and also seems reasonable in view of the greater importance of diffusion throughout the whole of the frozen boundary layer. It can be seen, however, that for a Lewis Number not too far from unity there is little difference in heat transfer for the frozen as opposed to the equilibrium boundary layer.

A few cases for noncatalytic wall were also computed. The resultant heat-transfer parameter could be given approximately by Eq. (62) with $L = 0$—i.e., the heat transfer becomes proportional to $h_s - h_D$.

A comparison of the distributions of enthalpy, temperature, and atom concentration for an equilibrium and a frozen boundary layer with identical catalytic wall and free-stream conditions is shown in Figs. 5 and 6. Both cases give very nearly the same heat transfer; however, the enthalpy distributions are slightly different (since $L = 1.4$) and the temperature and concentration distributions are markedly different, as is the mechanism of heat transfer.

(10) Finite Recombination Rate

This most general case was solved using Method 2 with values of the recombination rate parameter (C_1) varying from zero (frozen) to infinity (equilibrium). As for the frozen boundary layer, the wall may be either catalytic or noncatalytic, and both of these alternatives were calculated. It is to be expected, of course, that for large values of C_1 (near equilibrium) there should be little effect of wall catalysis, since few atoms reach the wall.

The heat-transfer parameter for one flight condition and wall temperature is plotted in Fig. 7 for the complete range of C_1. The solid lines are the total heat transfer for both catalytic (upper curve) and noncatalytic (lower curve) surfaces. For the catalytic wall, the fraction of heat transfer by conduction alone is shown by the dotted curve, so that the freezing of the boundary layer as recombination slows down (C_1 decreasing) is easily evident.

For either wall condition, C_1 must change by a factor of 10^4 in order for the boundary layer to change from substantially frozen to equilibrium throughout. Within this region of variation of C_1, the boundary layer will be partly frozen (near the outer edge) and partly in equilibrium (near the wall). Since the recombination term [Eq. (56)] varies as $T^{-3.5}$, and the temperature changes by a factor of twenty between wall and external flow for the case considered, large variations in the recombination rate are possible across the boundary layer, thus permitting it to be partly frozen and partly in equilibrium.

For the noncatalytic wall, the distributions of atom mass fraction for several recombination rate parameters are shown in Fig. 8. For C_1 very large, no atoms reach the wall, all having recombined in the gas. For lower values of C_1, some atoms reach the wall and, because none recombine on the wall, a finite atom concentration builds up. For C_1 approaching zero, there is no recombination and hence no concentration gradients exist.

It can be seen in Fig. 7 that a much lower value of C_1 is necessary to "freeze" the boundary layer when a noncatalytic wall is used than would be the case otherwise. This is caused by the "damming up" of the atoms at the noncatalytic wall, resulting in greater recombination because of high local concentrations.

From Eqs. (57) and (63) it can be seen that, for a given flight velocity (hence T_s), C_1 varies as the square of the stagnation point density (and thus for strong shock waves, as the square of the ambient density), and also as the nose radius. Thus the boundary layer would become frozen at a high enough altitude, this altitude being less for small nose radii than for large. In order to change from a frozen to an equilibrium boundary layer, C_1 must change by 10^4, and thus the density by 10^2, which is an altitude change of about 100,000 ft.

* Note that Lees [see reference 7, Eq. (19)] suggested that, for the frozen boundary layer, the exponent of L in Eq. (65) be 2/3.

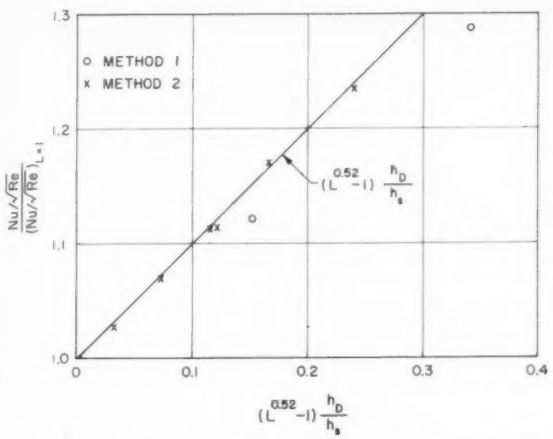

FIG. 3. Correlation of Lewis Number effects on the heat-transfer parameter $Nu/\sqrt{Re}$ for the equilibrium stagnation point boundary layer with L = constant $\neq 1$.

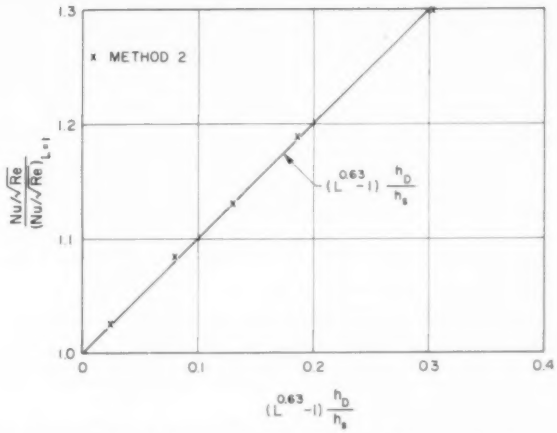

FIG. 4. Correlation of Lewis Number effects on the heat-transfer parameter $Nu/\sqrt{Re}$ for the frozen stagnation point boundary layer, L = constant $\neq 1$.

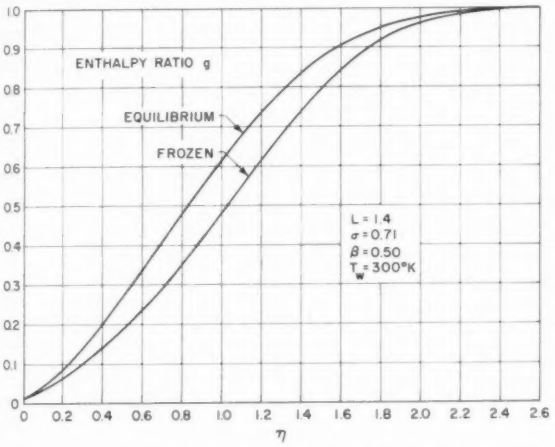

FIG. 5. Comparison of enthalpy distributions for an equilibrium and a frozen stagnation point boundary layer with the same external flow and wall conditions, g_w = 0.0123, c_{AS} = 0.499.

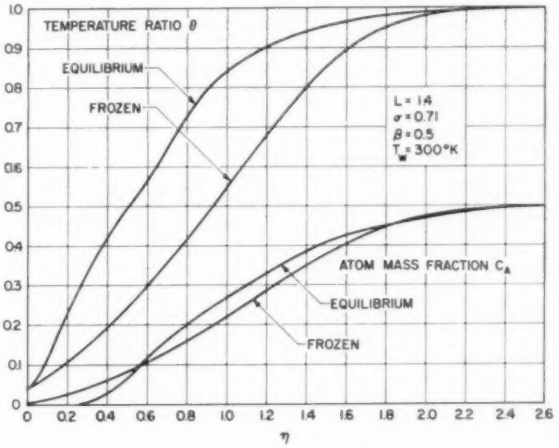

FIG. 6. Comparison of temperature and atom concentration distributions for an equilibrium and a frozen boundary layer with the same external flow and wall conditions, g_w = 0.0123, c_{AS} = 0.499.

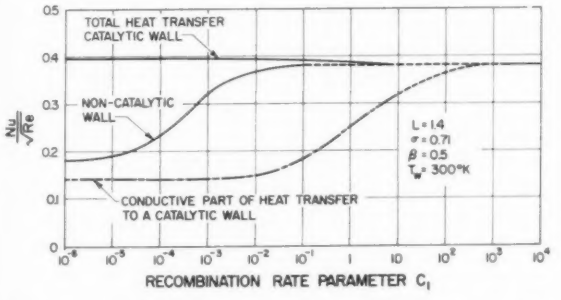

FIG. 7. Heat-transfer parameter $Nu/\sqrt{Re}$ for a boundary layer with finite recombination rates—i.e., various values of the recombination rate parameter C_1, g_w = 0.0123, c_{AS} = 0.536. Note the reduction of heat transfer to a noncatalytic wall for low values of C_1.

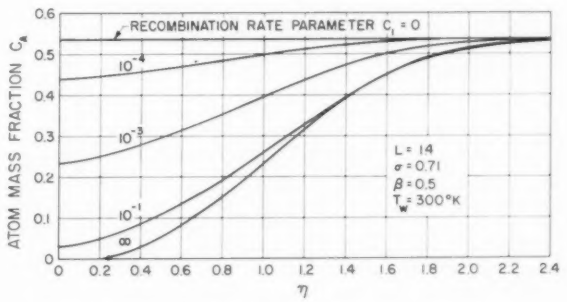

FIG. 8. Distributions of atom mass fraction in a stagnation point boundary layer on a noncatalytic wall for several values of the recombination rate parameter C_1, g_w = 0.0123, c_{AS} = 0.536.

(11) Conclusions

The laminar stagnation point heat transfer in dissociated air can be given by Eqs. (63) and (65) for the equilibrium and frozen boundary layers, respectively. These results were computed for a Prandtl Number of 0.71 and for a Lewis Number which was constant throughout the boundary layer.

The major deviation in the heat-transfer parameter from the low temperature, perfect gas value is due to the variation of $\rho\mu$ across the boundary layer. The heat transfer [Eq. (63)] is mainly dependent upon the value of $\rho\mu$ at the outer edge of the boundary layer.

If the wall catalyzes atomic recombination, the total heat transfer is not much affected by a nonequilibrium state of the boundary layer if the Lewis Number is near unity.

If the wall is noncatalytic, the heat transfer may be appreciably reduced when the boundary layer is frozen throughout—i.e., when the recombination reaction time becomes much longer than the time for a particle to diffuse through the boundary layer. Since the ratio of these times depends upon altitude and nose radius, there is a scale effect which determines the chemical state of the boundary layer.

Appendix—Details of the Numerical Solutions

Method 1

The momentum equation for the stagnation point boundary layer is given by Eq. (35)—namely,

$$(lf_{\eta\eta})_\eta + ff_{\eta\eta} + (1/2)[(\rho_s/\rho) - f_\eta^2] = 0 \quad \text{(A-1)}$$

If thermal diffusion is neglected (i.e., $L_i^T = 0$) then the energy equation in terms of the enthalpy becomes, from Eq. (37),

$$[(l/\sigma)g_\eta]_\eta + fg_\eta + \{(l/\sigma)\Sigma[c_{is}(h_i - h_i^0)/h_s](L_i - 1)s_{i\eta}\}_\eta = 0 \quad \text{(A-2)}$$

or

$$[(l/\sigma)(1 + d)g_\eta]_\eta + fg_\eta = 0 \quad \text{(A-3)}$$

where

$$\left.\begin{aligned} d &\equiv \Sigma[c_{is}(h_i - h_i^0)/h_s](L_i - 1)(\partial s_i/\partial g)_p \\ &= (L - 1)\Sigma(h_i - h_i^0)(\partial c_i/\partial h)_p \end{aligned}\right\} \quad \text{(A-4)}$$

where the subscript p denotes that the differentiation is at constant pressure and it is assumed $L_i = L =$ constant for all species.

In Method 1, which is suitable only for the equilibrium boundary layer, Eqs. (A-1) and (A-3) were solved simultaneously with the boundary conditions

$$f(0) = 0, \quad f_\eta(0) = 0, \quad f_\eta(\infty) = 1$$

$$g(0) = g_w, \quad g(\infty) = 1$$

The functions l, ρ_s/ρ and d were evaluated from the calculated equilibrium properties of air[11] and by taking the viscosity to vary according to Sutherland's formula [see Section (5) above]. For given external (stagnation point) flow conditions these quantities were plotted as functions of g. For numerical computation it was convenient to use analytic expressions of the following form:

$$l \equiv \rho\mu/\rho_w\mu_w = (\alpha_1/\sqrt{g}) - (\alpha_2/g) \quad \text{(A-5)}$$

$$\rho_s/\rho = 1 - \gamma_1(1 - g) - \gamma_2(1 - g)^4 \quad \text{(A-6)}$$

$$d = (L - 1)\Sigma(h_i - h_i^0)(\partial c_i/\partial h)_p = \beta_1 e^{-\beta_2/g} \quad \text{(A-7)}$$

The constants α, γ, β in each expression were determined by fitting these expressions to the equilibrium air calculations (see Fig. 1).

Numerical solutions for this problem were obtained on an IBM 650 computer. The method of solution was to pick values of $f_{\eta\eta}(0)$ and $g_\eta(0)$ and integrate the equations directly, recording the resultant asymptotic values of f_η and g for large values of η. After three such integrations an interpolation will produce better values of $f_{\eta\eta}(0)$ and $g_\eta(0)$. The interpolation procedure was repeated until the required conditions at "infinity" were met—i.e., $f_\eta \to 1$ and $g \to 1$. This interpolation was made an integral part of the numerical program so by starting with three initial guesses for $f_{\eta\eta}(0)$ and $g_\eta(0)$ the program would run automatically to completion.

It should be noted that Eqs. (A-1) and (A-3) are formally identical with the stagnation point equations solved by Cohen and Reshotko[10] except for the function d [Eq. (A-4)]. If $L = 1$, however, $d \equiv 0$; thus by specifying $L = 1$, $\sigma = 1$, $l = 1$ and $\rho_s/\rho = g$, the stagnation point solutions given by Cohen and Reshotko could be duplicated. (A table giving the specific values of the parameters for which solutions were obtained by the method described above may be obtained directly from the authors.)

Method 2

This method is a more general formulation in that it allows computation of the nonequilibrium boundary layer. As may be expected, however, it involves more approximations than the rather straightforward procedure of Method 1.

In the nonequilibrium case, the concentration of the various species is not determined by the enthalpy and the (known) pressure. It is necessary, therefore, to add a continuity equation for each species. Furthermore, it is convenient to express the thermodynamic properties in terms of the temperature and the concentrations of the species. The energy equation should, therefore, be written in terms of the temperature. To make this problem tractable it was assumed that air is a diatomic gas composed of "air" molecules and "air" atoms with properties properly averaged between oxygen and nitrogen. The dissociation energy of an air atom was taken to be the average dissociation energy in the external flow [see Eq. 59)]. With this assumption the problem is reduced to the simultaneous solution of three equations (momentum, energy and atom concentration) and the thermodynamic properties are to be expressed in terms of the temperature and atom concentration.

The momentum equation is still Eq. (A-3), with

$$\rho_s/\rho = [(1 + c_A)/(1 + c_{As})]\theta \quad \text{(A-8)}$$

$$l \equiv \rho\mu/\rho_w\mu_w = [1/(1 + c_A)]^{3/2}(\theta_w/\theta)F(\theta) \quad \text{(A-9)}$$

where

$$F(\theta) \equiv (T_s\theta/300)^{3/2}[413/(T_s\theta + 113)] + 3.7(T_s\theta/10{,}000)^2 - 2.35(T_s\theta/10{,}000)^4$$

and the stagnation temperature T_s is given in degrees Kelvin. The function $F(\theta)$ is a fitted curve giving the temperature dependence of the viscosity under the assumption that the atoms and molecules have the same collision cross-sections.

The energy equation in terms of the temperature is, from Eq. (36) with $L_i^T = 0$,

$$[(cl/\sigma)\theta_\eta]_\eta + cf\theta_\eta + (l/\sigma)\theta_\eta \times \Sigma(c_{pi}/\bar{c}_{pw})L_i c_{is} s_{i\eta} + \{2(du_e/dx)_s\}^{-1} \times \Sigma(w_i/\rho)[(h_i^0 - h_i)/\bar{c}_{pw}T_s] = 0 \quad \text{(A-10)}$$

where $$c \equiv \bar{c}_p/\bar{c}_{pw}$$

With the assumption of a simple diatomic gas and taking $L_i = L$ = constant, the third term may be rewritten as

$$(Ll/\sigma)\theta_\eta c_{A\eta}[(c_{pA} - c_{pM})/\bar{c}_{pw}]$$

and the fourth term, using Eqs. (56), (57), and (61), and taking $h_A = h_M$, becomes

$$C_1(h_D/\bar{c}_{pw}T_s)[(c_A^2 - c_{AE}^2)/\theta^{3.5}(1 + c_{As})]$$

Now $$c_{pM} \approx (\mathcal{R}/M)\{(7/2) + e^{-(T_V/T)^2}\}$$

where the exponential is the vibrational heat capacity and $T_V \approx 800°$K. for air; also

$$c_{pA} = (5/2)[\mathcal{R}/(M/2)]$$

Hence,

$$c \equiv \bar{c}_p/\bar{c}_{pw} = (10/7)c_A + \{1 + (2/7)e^{-(\theta V/\theta)^2}\}(1 - c_A) \quad \text{(A-11)}$$

$$(c_{pA} - c_{pM})/\bar{c}_{pw} = (3/7) - (2/7)e^{-(\theta V/\theta)^2} \quad \text{(A-12)}$$

For computation then the energy equation becomes

$$[(cl/\sigma)\theta_\eta]_\eta + cf\theta_\eta + e(Ll/\sigma)\theta_\eta c_{A\eta} + C_1C_2m = 0 \quad \text{(A-13)}$$

where

$l \equiv \rho\mu/\rho_w\mu_w = [1/(1 + c_A)]^{3/2}(\theta_w/\theta)F(\theta)$, see Eq. (A-9)

$e \equiv (c_{pA} - c_{pM})/\bar{c}_{pw} = (3/7) - (2/7)e^{-(\theta V/\theta)^2}$

$c \equiv \bar{c}_p/\bar{c}_{pw} = (10/7)c_A + \{1 + (2/7)e^{-(\theta V/\theta)^2}\}(1 - c_A)$

C_1 = parameter, see Eq. (57)

$C_2 \equiv h_D/\bar{c}_{pw}T_s$ = parameter, see Eq. (61)

$m \equiv (c_A^2 - c_{AE}^2)/\theta^{3.5}(1 + c_A)$

The equilibrium atom mass fraction c_{AE} can be determined from reference 11. For computation c_{AE} was approximated by

$$c_{AE} = c_{As}e^{C_3(1 - 1/\theta)} \quad \text{(A-14)}$$

where C_3 is a constant.

The continuity equation for atoms was written in terms of the atom mass fraction c_A instead of the normalized atom mass fraction s. Thus Eq. (34) becomes

$$[(lL/\sigma)c_{A\eta}]_\eta + fc_{A\eta} - \{2(du_e/dx)_s\}^{-1}\Sigma(w_i/\rho) = 0 \quad \text{(A-15)}$$

or

$$[(lL/\sigma)c_{A\eta}]_\eta + fc_{A\eta} - C_1m = 0 \quad \text{(A-16)}$$

Method 2 for the nonequilibrium boundary layer is the simultaneous solution of Eqs. (A-1), (A-13) and (A-16) with the boundary conditions

$$f(0) = 0, \quad f_\eta(0) = 0, \quad f_\eta(\infty) = 1$$
$$\theta(0) = \theta_w, \quad \theta(\infty) = 1$$

$$\left.\begin{array}{l} c_A(0) = 0 \quad \text{for catalytic wall} \\ c_{A\eta}(0) = 0 \quad \text{for noncatalytic wall} \end{array}\right\} \quad c_A(\infty) = c_{As}$$

Solutions were obtained on a digital computer using an iterative procedure similar to that used in Method 1.

The limiting case of the equilibrium boundary layer was obtained by Method 2 by eliminating the term C_1m between Eqs. (A-13) and (A-16) and solving the resulting equation simultaneously with Eq. (A-1), taking the equilibrium atom concentration as a known quantity in the form of Eq. (A-14). The limiting case of the frozen boundary was obtained by putting $C_1 \equiv 0$.*

References

[1] Moore, L. L., *A Solution of the Laminar Boundary Layer Equations for a Compressible Fluid with Variable Properties, Including Dissociation*, Journal of the Aeronautical Sciences, Vol. 19, No. 8, pp. 505–518, August, 1952.

[2] Hansen, C. F., *Note on the Prandtl Number for Dissociated Air*, Journal of the Aeronautical Sciences, Vol. 20, No. 11, pp. 789–790, November, 1953.

[3] Romig, M F., and Dore, F. J., *Solutions of the Compressible Laminar Boundary Layer Including the Case of a Dissociated Free Stream*, Convair Report No. ZA-7-012, San Diego, Calif., 1954.

[4] Beckwith, I. E., *The Effect of Dissociation in the Stagnation Region of a Blunt-Nosed Body*, Journal of the Aeronautical Sciences, Vol. 20, No. 9, pp. 645–646, September, 1953.

[5] Crown, J. C., *The Laminar Boundary Layer at Hypersonic Speeds*, Navord Report 2299, U.S. Naval Ordnance Lab., 1952.

[6] Mark, R., *Compressible Laminar Heat Transfer Near the Stagnation Point of Blunt Bodies of Revolution*, Convair Report No. ZA-7-016, San Diego, Calif., 1955.

[7] Lees, L., *Laminar Heat Transfer Over Blunt-Nosed Bodies at Hypersonic Flight Speeds*, Jet Propulsion, Vol. 26, No. 4, pp. 259–269, 1956.

[8] Hirschfelder, J. O., Curtiss, C. F., and Bird, R. B., *Molecular Theory of Gases and Liquids*, John Wiley and Sons, Inc., New York, 1954.

[9] Probstein, R. F., *Methods of Calculating the Equilibrium Laminar Heat Transfer Rate at Hypersonic Flight Speeds*, Jet Propulsion, Vol. 26, No. 6, pp. 497–499, 1956.

[10] Cohen, C. B., and Reshotko, E., *Similar Solutions for the Compressible Laminar Boundary Layer with Heat Transfer and Pressure Gradient*, NACA TN 3325, 1955.

[11] Hilsenrath, J. and Beckett, C., *Tables of Thermodynamic Properties of Argon-Free Air to 15,000°K*, AEDC-TN-56-12, Arnold Engineering Development Center, USAF, September, 1956 (ASTIA Document No. AD-98974).

* Numerical results of these calculations may be obtained directly from the authors.

(*Continued on page 121*)

Stagnation Point Heat-Transfer Measurements in Dissociated Air†

P. H. ROSE* AND W. I. STARK**

Avco Research Laboratory

SUMMARY

The results of an experimental investigation of the laminar heat transfer at the stagnation point of a blunt body in partially dissociated air are presented and are compared to the theoretical treatment of Fay and Riddell.[3] Heat-transfer results are presented for air temperatures as high as 8,000°K. where more than 50 per cent of the molecules are in the dissociated state. The experiments were performed in a shock tube and the new experimental techniques and principles are discussed briefly. Simulation of flight stagnation conditions at velocities up to satellite velocity of 26,000 ft./sec. is shown to be possible in shock tubes and data has been obtained over a large altitude range at these velocities.

SYMBOLS

A = ratio of thermal conductivity and diffusivity $\equiv (K_i/K_m)\sqrt{k_m/k_i}$
a = speed of sound
C_p = heat capacity
D = diffusion coefficient
E = electrical potential
h = enthalpy per unit mass
h_D = average dissociation energy per unit mass of atoms times the atom mass fraction in the external flow
I = electric current
K = thermal conductivity
k = diffusivity $\equiv K/\rho C_p$
L = Lewis Number $\equiv D\rho C_p/K$
l = linear dimension, thickness
M = Mach Number
Nu = Nusselt Number $\equiv qx/K\Delta T$
p = pressure
q = specific heat flux
R = resistance
Re = Reynolds Number $\equiv \rho ul/\mu$
T = temperature
t = time
u = velocity
x = linear dimension
α = temperature coefficient of resistivity
γ = ratio of specific heats
μ = viscosity
ρ = density
σ = Prandtl Number $\equiv C_p\mu/K$
τ = characteristic time of experiment

Subscripts

i = insulator
m = metal
o = constant or steady state
s = stagnation conditions
w = wall
1 = initial conditions
2 = conditions behind moving shock
4 = driver conditions

INTRODUCTION

THE PROBLEM of aerodynamic heat transfer at the stagnation point of a blunt body in hypersonic flow, characterized by large temperature gradients in the boundary layer has received a considerable amount of attention in the literature (see, for example, Lees,[1] Cohen and Reshotko,[2] Sibulkin,[18] and others). Recently, in reference 3, Fay and Riddell have considered the more general problem by including the effects of variable fluid properties in the boundary layer, diffusion of atoms, and chemical processes such as dissociation and recombination. In this treatment, the heat transfer at the stagnation point has been solved for several cases; (1) a boundary layer in thermochemical equilibrium throughout, (2) a boundary layer whose composition is "frozen" at the atom and ion concentrations that exist at the edge of the boundary layer, and (3) a boundary layer wherein the concentration of each chemical species is permitted to adjust as dictated by a finite atomic recombination rate.‡ This paper presents the methods and results of the experimental attack on this problem.

At the present time, much effort is being spent on the development of a facility which is capable of reproducing, in the laboratory, the environmental conditions encountered by a vehicle traveling at hypersonic velocities. Some of the schemes generally under consideration are hypervelocity guns, wind-tunnel modifications, free flight missiles and several versions of the shock tube. Of these, only the shock tube has the ability to produce the correct conditions of temperature and pressure while holding the model stationary—i.e., by moving the air as is done in wind tunnels. This method of operation has the advantage of simplifying the instrumentation, which is very difficult in any hyper-

Received May 14, 1957.

† This work was sponsored by the Ballistic Missile Division, ARDC, USAF, under Contract AF 04(645)-18.

The authors of this paper would like to express their appreciation to the many members of the staff of the Avco Research Laboratory who contributed to this program. In particular they are grateful for the many discussions and suggestions by Arthur R. Kantrowitz, Director of the Laboratory, Mac C. Adams, H. K. Brown, S. C. Lin, and Frederick R. Riddell. Most of the experiments reported herein were ably performed by Thomas Connolly, Raymond Gardner, Weldon Nelson, and James Trider.

* Principal Research Scientist.

** Associate Engineer.

‡ The "frozen" and "equilibrium" situation can best be distinguished by considering the relaxation time of the chemical process—i.e., recombination of dissociated atoms—as compared to a characteristic flow time, such as the time required for a particle to flow through the boundary layer. The frozen flow is defined as $\tau_{flow} \ll \tau_{recomb.}$ and equilibrium as $\tau_{flow} \gg \tau_{recomb.}$.

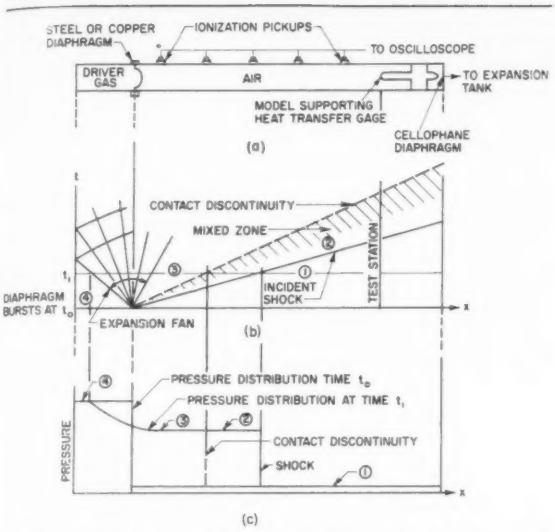

FIG. 1. (a) Schematic diagram of a shock tube as used for heat-transfer experiments. (b) x-t diagram showing the progress of the shock wave and the expansion wave following the diaphragm burst. The gases which were originally separated by the diaphragm are separated by the contact discontinuity (interface). (c) Pressure distribution at several typical times in the shock tube. [Time t_0 and t_1 from (b).]

sonic facility. In addition, the low cost of operating a shock tube makes it a very attractive instrument for conducting basic high temperature gas dynamic research.

The shock tube heat-transfer experiments described in this paper involved the development of new instrumentation capable of microsecond response. For surface temperature measurements, the thin film resistance thermometer, as used by other investigators for similar purposes, but at low Mach Numbers, was developed for use under the extreme temperatures and pressures encountered at the stagnation point at very high Mach Numbers.* In addition, a new type of meter has been developed based on the calorimeter principle. Heat-transfer measurements have been performed over a wide range of shock tube pressures and temperatures, simulating hypersonic flight at velocities up to about 26,000 ft./sec. The results are compared with the theoretical analysis of Fay and Riddell[3] and indicate reasonably good agreement with the equilibrium boundary-layer solutions.

THE SHOCK TUBE

The shock tube, as used for these experiments, has been described in the literature.[4–6] Schematically, the shock tube is shown in Fig. 1. A strong shock wave is created by the sudden removal (rupture) of a diaphragm separating a high- and low-pressure gas. Compression waves advance into the low-pressure gas and quickly (in a few diameters) steepen to form a shock wave. Simultaneously, the high-pressure region also expands, but the interface between these two gases moves at the particle velocity which is slightly slower than the shock wave velocity. Consequently, the shock wave runs away from this interface, or contact discontinuity, creating a continually growing region as the shock wave moves down the tube. When the shock wave advances into the low-pressure gas (air for the present experiments) it behaves according to the laws of conservation of momentum, energy, and mass, resulting in a gas which has been compressed, heated, and set into motion at almost the velocity of the shock wave. By a change of coordinate system—i.e., by considering the problem from the point of view of an observer traveling at the shock wave velocity—this process is reduced to a more generally known form of the Rankine-Hugoniot equations.

The conventional method of presenting the processes occurring in a shock tube is the x-t, space-time, diagram in the center part of Fig. 1. The diaphragm breaks at distance and time equal to zero. In practice, the interface is found to spread, probably due to turbulent mixing, and is indicated as a region rather than a line. Downstream in the shock tube, the time interval between the passage of the shock wave and the arrival of the mixing region gives the experimenter a region which has been uniformly heated and compressed in which to make measurements.

The pressure at every point in the tube at several typical times is presented in the lower part of Fig. 1.

It is possible to produce a wide range of conditions of temperature, pressure, and velocity in shock tubes, limited only by the strength of the shock wave that can be created in a given gas. The strength of this shock wave can be expressed as a function of only the pressure ratio across the diaphragm and the ratio of the speed of sound in the driver and in the driven gas, as well as the specific heat ratio in the driver gas, γ_4, as follows:

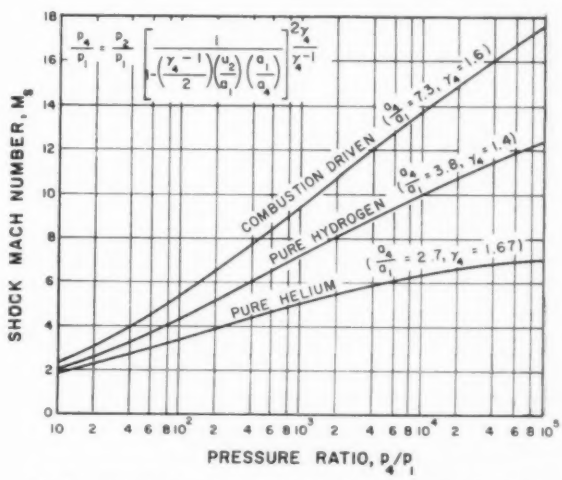
$\frac{p_4}{p_1} = \frac{p_2}{p_1}\left[1-\left(\frac{\gamma_4-1}{2}\right)\left(\frac{u_2}{a_1}\right)\left(\frac{a_1}{a_4}\right)\right]^{\frac{2\gamma_4}{\gamma_4-1}}$
SHOCK MACH NUMBER, M_s
PRESSURE RATIO, p_4/p_1
COMBUSTION DRIVEN ($\frac{a_4}{a_1}$ = 7.3, γ_4 = 1.6)
PURE HYDROGEN ($\frac{a_4}{a_1}$ = 3.8, γ_4 = 1.4)
PURE HELIUM ($\frac{a_4}{a_1}$ = 2.7, γ_4 = 1.67)

FIG. 2. Relation between shock Mach Number and diaphragm pressure ratio for three typical driver gases: (a) combustion of O_2, H_2, and He; (b) cold hydrogen; and (c) cold helium (equilibrium air is the driven gas).

* As well as electrical-conductivities of air that are comparable to the resistivity of the gage resistance element.

$$\frac{p_4}{p_1} = \frac{p_2}{p_1}\left\{\frac{1}{1 - [(\gamma_4 - 1)/2]\,(u_2/a_1)\,(a_1/a_4)}\right\}^{2\gamma_4/(\gamma_4-1)} \quad (1)$$

Fig. 2 shows the theoretical strength of the shock waves produced in air driven by cold hydrogen and also by a mixture of oxygen, hydrogen and helium in which an increase in the speed of sound ratio is achieved by combustion. The experimentally achieved shock wave strengths agree quite well.

The equipment used for these experiments is capable of producing shock waves traveling at over twenty times the speed of sound in room temperature air. If the air were an ideal diatomic gas ($\gamma = 1.4$) this strength shock wave would heat the air to a temperature of about 24,000°K. However, energy actually goes into dissociating the oxygen and nitrogen molecules rather than into raising the temperature. Using the properties of air in thermochemical equilibrium, either from the National Bureau of Standards tables,[7] or from the data calculated by the Rand Corporation,[8] in the solution for the conditions behind the shock wave, the air is actually found to attain a temperature of only 9,000°K.

Correlation of physical measurements in shock tubes with quantities calculated from theories requires a precise knowledge of the state of the gas in the shock tube at the point where the measurements are being conducted. For this purpose the initial pressure in the driven gas and speed of the moving shock wave are measured. From these two measurements, the properties of the gas at any part of the shock tube at any time can be calculated. For this purpose, the Avco Research Laboratory has constructed a Mollier diagram for air[9] from the National Bureau of Standards tables. Reference 9 contains curves of the solutions of the Rankine-Hugoniot equations for equilibrium air for typical shock tube and hypersonic flight conditions.

It must be pointed out that in the example discussed above, the speed of sound in the gas heated by the incident shock wave is approximately 6000 ft. per sec. due to its high static temperature, so that the air even though traveling at almost 20,000 ft. per sec. has a flow Mach Number of only about three.

Simulation

At the stagnation point of a blunt body in hypersonic flight, the usual separation of theoretical aerodynamics into a viscous and inviscid problem is exactly applicable to the experimental situation. As long as there are no interactions between the shock wave and the boundary layer, such as when the boundary layer is of the same thickness as the detachment distance, where shock-wave boundary-layer intersections are present or when flow separations are involved, the boundary-layer problem can be considered experimentally apart from the inviscid flow field and Reynolds Number simulation does not have to be achieved.

The temperature, pressure, and velocity environment created in the shock tube can be applied directly to the solution of the stagnation point heat-transfer problem. Aerodynamic heat transfer at the stagnation point, by conduction, convection, and diffusion of air molecules and atoms is simulated in a scale test if the conditions at the edge of the boundary layer in the vicinity of the stagnation point, including the pressure distribution and the wall conditions, are correctly reproduced.

It can be shown that the heat-transfer rate through a laminar boundary layer at the stagnation point at low speeds, where the product $\rho\mu$ in the boundary layer does not vary from the free stream to the wall and the density varies inversely with the temperature,[2] can be expressed in a nondimensional form as

$$Nu/\sqrt{Re} = \text{constant} = 0.763\sigma^{0.4} \quad (2)$$

The numerical solution of Fay and Riddell[3] for the equilibrium boundary layer with variable fluid properties can be correlated by considering the $\rho\mu$ ratio across the boundary layer, by the expression

$$Nu/\sqrt{Re} = 0.763\sigma^{0.4}\{[(\rho\mu)_s/(\rho\mu)_w]^{0.4} \times [1 + (L^{0.52} - 1)\,(h_D/h_s)]\} \quad (3)$$

The heat transfer at the stagnation point can be written from this expression, assuming the pressure distribution can be expressed by the Newtonian assumption, as

$$q = 0.763\{(\rho\mu)_w^{0.1}(\rho\mu)_s^{0.4}\,[1 + (L^{0.52} - 1)\,(h_D/h_s)] \times [(h_s - h_w)/\sigma^{0.6}]\,(1/\sqrt{R})\,(2p_s/\rho_s)^{1/4}\} \quad (4)$$

This equation makes the heat-transfer simulation at the stagnation point dependent on the inviscid flow parameters, the wall conditions, and the pressure gradient. Note that the wall conditions enter as $(\rho\mu)_w^{0.1}$ and $(h_s - h_w)$ and affect Eq. (4) very weakly, so that high cooling, as long as the cooling is large, is sufficient. In addition, the transport properties of air—i.e., μ, K, and D—enter the solution in the form of the Lewis Number, $L \equiv D\rho C_p/K$, and Prandtl Number, $\sigma \equiv C_p\mu/K$.

The inviscid flow conditions produced at the stagnation point of a model in the shock tube are used to simulate the hypersonic flight situation. However, the stagnation enthalpy is achieved in a manner different from flight—i.e., in a two-step process: first, through the conversion of the kinetic energy of the incident shock velocity, $u_s^2/2$, into the total enthalpy of the hot gas region (as considered in the shock fixed coordinate system) and, second, through the conversion of the total enthalpy of the moving hot gas into the stagnation enthalpy in the shock tube fixed coordinate system. The initial pressure level of the experiment can be adjusted to obtain the proper stagnation density, ρ_s, in the inviscid flow.

The boundary layer on a model in the shock tube under the same stagnation conditions as in hypersonic flight will be an exact geometric scale reproduction of the flight case if the two situations are chemically similar. This means that the flight and shock tube

FIG. 3. Schlieren photograph of the flow over the nose of a hemisphere-cylinder model in a $1^1/_2$ in. inside diameter shock tube. Note fine Mach lines whose inclination to the body is accurately measurable

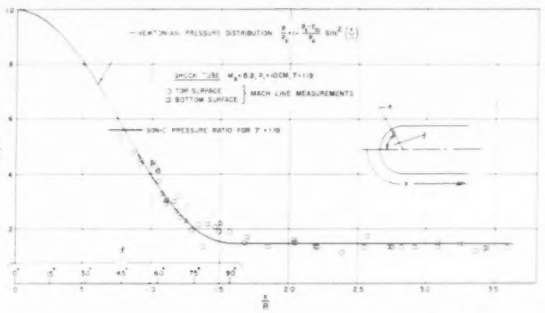

FIG. 4. Pressure distribution calculated from Mach line measurements on Fig. 3, compared to the Newtonian pressure distribution. The agreement is reasonable, especially on the aft portion of the body and near the sonic point. Stagnation conditions are equivalent to a flight velocity of approximately 13,000 ft./sec. and an altitude of 25,000 ft. The flow Mach Number is approximately 2.3.

boundary layers must be either both in thermochemical equilibrium throughout or both completely "frozen." Between these two extremes the scaling of the recombination parameter discussed by Fay and Riddell[3] is applicable. The implication of the latter type of simulation is that the stagnation enthalpy and the atom diffusion process through the boundary layer are correctly duplicated in the experiment. The only other variable which must be determined to complete the simulation principle is the velocity gradient at the stagnation point or pressure distribution.

For blunt bodies in hypersonic flow, the Newtonian approximation predicts that the pressure distribution is independent of Mach Number. This approximation to the pressure distribution has been shown experimentally to be correct even at surprisingly low Mach Numbers for very blunt bodies. It remains only to be shown that this approximation can be made in the shock tube. Because of the difficulty of making reliable pressure measurements in the time scale of the shock tube an optical scheme from which the pressure distribution can be calculated has been developed.

Fig. 3 shows a schlieren photograph of the flow over a hemisphere-cylinder model in a $1^1/_2$ in. inside diameter circular shock tube. The surface of the model was roughened slightly so that weak disturbances—i.e., Mach waves—propagate outward from the body. By following an isentrope on a Mollier diagram from the stagnation point, the pressure at every point where a Mach angle is measured can be calculated for equilibrium air.*

Fig. 4 shows the pressure distribution deduced in this manner from an experiment performed at shock Mach Number 8.8 in an initial pressure of 10 cm. of Hg of air (flow Mach Number about 2.3). The pressure distribution does not follow the Newtonian estimate exactly. However, the sonic point, as indicated from the first visible Mach line, seems to occur very close to the predicted point. In addition, the slope of the pressure distribution at this point is very close to the estimated slope, leaving little doubt that the pressure distribution inside the sonic point is close to Newtonian.

The fact that the pressure distribution in the vicinity of the stagnation point on a hemisphere cylinder model can be approximated by the Newtonian estimate, even for relatively weak shocks, makes the shock tube a very useful tool for experimental boundary-layer studies. Simulation of stagnation point heat transfer in a shock tube thus becomes completely independent of flow Mach Number and simply a matter of geometric scaling and duplicating enthalpy and pressure.

Fig. 5 shows the stagnation conditions attainable in a shock tube as compared to those encountered in

* This calculation depends on how the speed of sound is defined along the isentropic expansion—i.e., equilibrium or "frozen" at stagnation point dissociation. For the example of Figs. 3 and 4, the degree of dissociation is negligible so that variances with these definitions are eliminated. The fluid properties in an isentropic expansion in equilibrium air can be calculated from the use of an effective γ to a reasonable accuracy; this value is 1.19 for the case of Figs. 3 and 4.

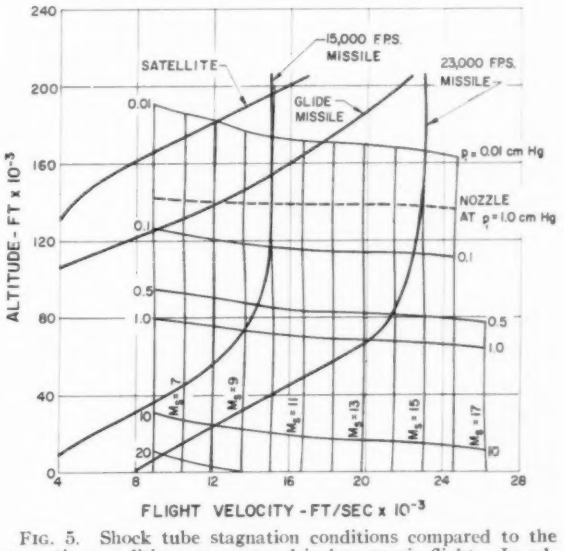

FIG. 5. Shock tube stagnation conditions compared to the stagnation conditions encountered in hypersonic flight. In addition, conditions attainable by a 36:1 area ratio nozzle are indicated for one initial pressure. Typical trajectories[10] of several types of missiles are also shown.

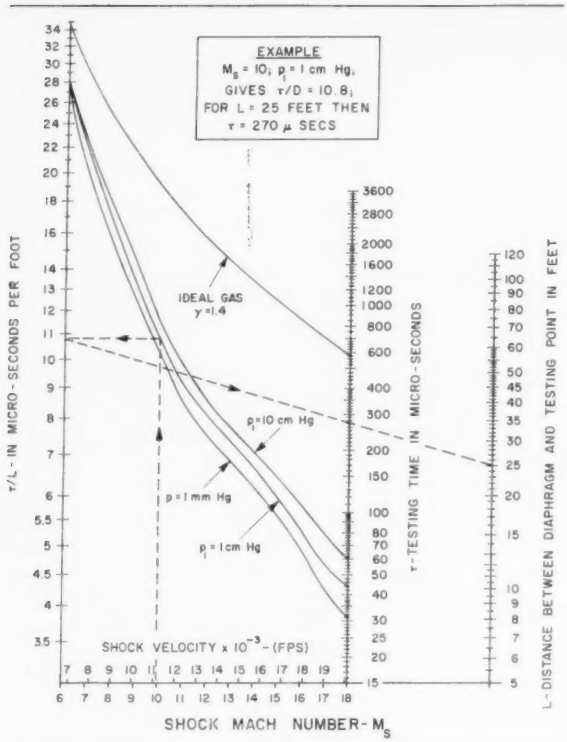
EXAMPLE
M_s = 10; p_1 = 1 cm Hg;
GIVES τ/D = 10.8;
FOR L = 25 FEET THEN
τ = 270 μ SECS
IDEAL GAS
γ=1.4
p_1=10 cm Hg
p_1=1 mm Hg
p_1=1 cm Hg
τ/L - IN MICRO-SECONDS PER FOOT
τ - TESTING TIME IN MICRO-SECONDS
L - DISTANCE BETWEEN DIAPHRAGM AND TESTING POINT IN FEET
SHOCK VELOCITY x 10^{-3} - (FPS)
SHOCK MACH NUMBER - M_s

FIG. 6. Nomograph* for calculating the time interval between the arrival of the shock wave and the driver gas at a given station in a shock tube. Calculations have been carried out considering air an ideal gas ($\gamma = 1.4$), and in equilibrium. For equilibrium air the testing time is greatly reduced.

hypersonic flight, on a pressure-temperature grid. The conditions attainable in a straight shock tube without the addition of expansion nozzles are plotted. Trajectories of various types of proposed hypersonic vehicles, as given by Masson and Gazeley,[10] are shown to fall well into the accessible range. In particular, trajectories of ballistic bodies fall into the range covered by the straight shock tube. For better simulation of the flight of glide vehicles, satellites and continuous flight, the shock tube gases can be expanded in a nozzle extending the shock tube capabilities to somewhat higher altitudes.[11]

Most of the experiments reported in this paper were performed in $1^1/_2$ in. inside diameter shock tubes, varying from 15 to 30 ft. in length.

Measurement Techniques

Because of the extremely short steady-state times available in shock tube experiments, instrumentation presents a problem. Fig. 6 gives the testing time in shock tubes under typical conditions. The departure from the ideal gas gives shorter times due to the higher real gas density ratios. In practice, it is found that only 40 to 70 per cent of the theoretical time is actually available, probably due to mixing at the interface and to attenuation of the shock strength.

Typical of the instrumentation problem is the measurement of the velocity of the incident shock wave, from which the stagnation conditions are calculated. In this experiment, the passage of the shock wave at a number of points along the length of the tube is recorded by ionization-sensitive pickups. The signals are displayed on the face of an oscilloscope on a sweep that has been extended to cover very long times, yet is readable to very short intervals. An example of the trace of this measurement is shown in Fig. 7. Accuracy better than ±2 per cent for each interval can be obtained, depending on the accuracy of the signal and pickup spacing.

In order to make significant heat-transfer measurements in shock tubes an instrument capable of microsecond response had to be developed. The most promising schemes considered were of two types, (a) surface temperature history measurements, and (b) calorimetric measurements.

Because of the difficulty of shock tube instrumentation, it was felt highly desirable to make several independent measurements of the heat-transfer phenomena. Variations of the resistance thermometer principle were found satisfactory for both above schemes.

If one considers the one-dimensional heat conduction problem for a finite thickness of a metal, backed up by an infinitely thick insulator, with a constant heat flux, q_o, entering the metal surface, then the temperature response of the interface between the metal and the insulator can be written as follows:

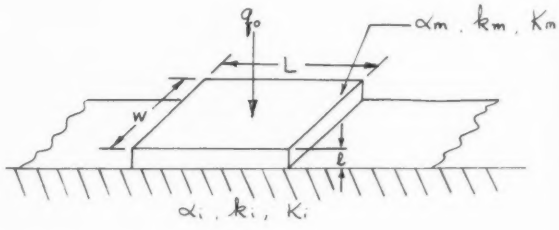

$$T_i(l,t) = T_m(l,t) = \frac{2\sqrt{k_m}}{K_m}\,\frac{q_o}{(1+A)}\sum_{n=0}^{\infty}\left(\frac{1-A}{1+A}\right)^n \times \left\{2\sqrt{\frac{t}{\pi}}\,e^{-[(2n+1)^2 l^2/4k_m t]} - \frac{2n+1}{\sqrt{k_m}}\,\operatorname{erfc}\frac{(2n+1)l}{2\sqrt{k_m t}}\right\} \quad (5)$$

If the metal thickness, l, is very small, that is, very much smaller than the characteristic diffusion length in the insulator, $l_i \equiv \sqrt{k_i \tau}$,† then the temperature response of the metal essentially is the same as the re-

* Enter abscissa at shock Mach Number and find intersection with initial pressure curve. Locate values of left-hand ordinates, at the latter intersection. Line up the value of τ/L with the length of the shock tube on the right-hand ordinate and read the testing time τ on the center ordinate. Experimental values of τ are found to be approximately 40 to 70 per cent of the values calculated this way.

† And therefore also much smaller than the same length for the metal, $l_m \equiv \sqrt{k_m \tau}$, which is larger than l_i.

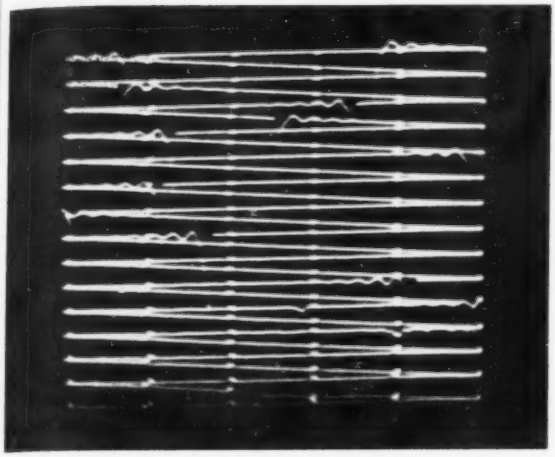

FIG. 7. Typical oscillograph from the shock velocity timing circuit. The oscilloscope sweep starts at the top and makes a complete cycle, left to right and back, every 100 microsec. The bright spots are produced by the output from a crystal oscillator, spaced exactly 10 microsec. apart. The time of arrival of the shock wave at each successive ionization-sensitive pickup is denoted by the sudden break in the sweep (change in gap resistance caused by the ionized gas). Sample oscillograph has signals from 12 pickups. The pickups are spaced approximately a foot apart.

sponse of the interface temperature,* and can be reduced to

$$T_m(l, t) = (2\sqrt{k_t}/\sqrt{\pi}K_t)q_o\sqrt{t} \qquad (6)$$

For the case of the thin resistance thermometer, a current is passed through a thin metal film through which the heat is transferred to the insulator. The resistance change of the metal, interpreted as the surface temperature of the insulator, yields the heat-transfer rate from Eq. (6). In terms of measured quantities, the heat-transfer rate can be written as

$$q_o = [1/k''(IR)]\,(E/\sqrt{t}) \qquad (7)$$

where

$$k'' = 2\alpha_m\sqrt{k_t}/\sqrt{\pi}\,K_t \qquad (8)$$

represents the physical properties of the resistance thermometer.

The other extreme compared to the very thin film situation is a metal layer whose thickness is larger than the characteristic diffusion length of the metal—i.e., $l > \sqrt{k_m\tau}$. Such a gage is one in which essentially all the heat stays in the metal—i.e., a calorimeter. By expanding the expression for the temperature and resistivity of a thin metal lamina and integrating over the metal thickness, an average temperature can be found from which the response of the resistance element to the heat flux is described as follows:

$$q_o = [1/(IR)]\,(\rho Cl/\alpha)_m\,(dE/dt) \qquad (9)$$

This expression is good as long as there are no two-dimensional effects—that is, each lamina is at a uniform temperature.

* The error introduced by the heat capacity of the thin metal film has been considered in reference 19 and is negligible for the geometry used in these experiments.

Both of the principles described above can be extended to the case of nonuniform heat flux in time—i.e., $q = q(t)$. The calorimeter integrates the total heat input into the metal. Therefore, the heat-transfer rate at any time is given by the instantaneous slope of the voltage signal with time.

For the thin resistance thermometer, the surface temperature response to a heat input arbitrarily changing with time can be written as

$$T(o, t) = T(l, t) = \frac{\sqrt{k_t}}{K_t\sqrt{\pi}}\int_0^t \frac{q(\tau)}{\sqrt{t-\tau}}\,d\tau \qquad (10)$$

This expression can readily be inverted to solve for the time-dependent heat-transfer rate as a function of surface temperature, which, in terms of the temperature coefficient of resistivity and the measured quantities, yields

$$q(t) = \frac{1}{k''(IR)\pi}\left\{\frac{2E(t)}{\sqrt{t}} + \int_0^t \frac{E(t) - E(\tau)}{(t-\tau)^{3/2}}\,d\tau\right\} \qquad (11)$$

This equation has been set up for solution by digital computer for reduction of the data obtained from the photographic oscillograph records.

The thin resistance thermometer as used by Blackman[12] and others[13,14] was developed mainly as a trigger device. At the stagnation point of models under the extreme conditions created by strong moving shock waves considerable development was required before quantitative data was obtained. It can be shown that a thin gage can be up to one micron thick, considering times of the order of 100 microsec.[19] The metal films produced were measured by interference microscope to be approximately 0.3 microns thick.

The production of these thin films required much development. Evaporated films were found to be unsatisfactory because they did not adhere to the insulator sufficiently. The most promising results were obtained through the use of a solution of organic platinum and gold compounds of resinous character in oils and other solvents. This solution, manufactured by the Hanovia Chemical and Manufacturing Company, is called Liquid Bright Platinum No. 05. The solution is brush applied in the desired geometry and fired in a ventilated oven to about 1,200°F. for a few minutes. In order to produce highly erosion-resistant films, several coats, each individually fired, were required.

In the analysis of the data from thin heat-transfer gages, the characteristics of the gage are represented by the diffusivity and the thermal conductivity of the insulator and the temperature coefficient of resistivity of the metal. The latter, as measured in a laboratory oven from 0° up to 200°C., when combined with the manufacturer's data for the properties of the insulator—i.e., pyrex—gives a value of k'', defined by Eq. (8), of 0.00765. Because the metal fuses into the outer layers of the insulator, the thermal conductivity of the pyrex could be greatly in doubt. To eliminate the uncertainty in the value of the calibration constant, k'', due

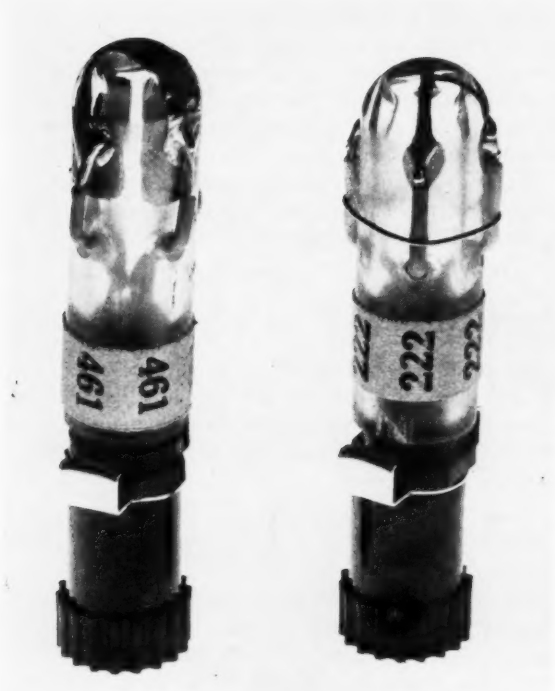

FIG. 8. Sample heat-transfer gages used. The thin gage is on the right and the calorimeter gage on the left. Both gages are mounted on ground and polished pyrex hemisphere-cylinder models. Gages normally plug into sting model support.

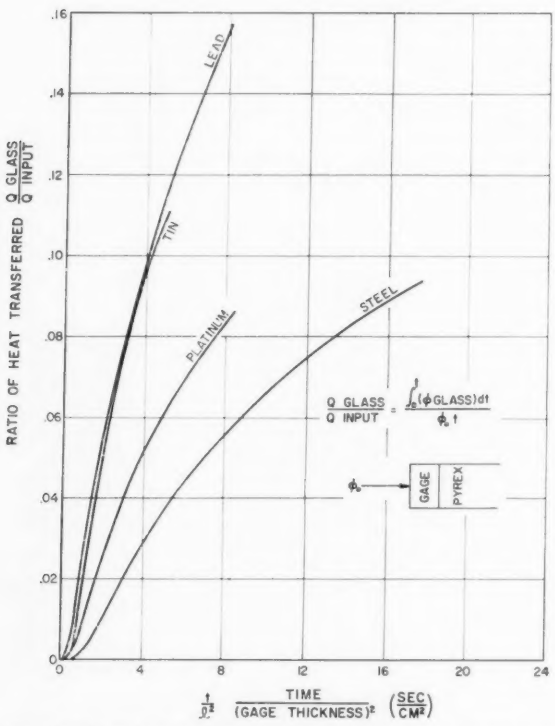

FIG. 9. Heat loss from calorimeter to the insulator for various heat-transfer gage materials. Calculations are made assuming a perfect contact between the metal and insulator.

to this effect, a method of dynamically calibrating the gage in the true scale of the shock tube experiment was developed.

When a pulse of electrical energy is passed through a resistance thermometer, the resistance of the element will change in proportion to the power dissipated. If this pulse is made comparable in energy and time duration to thermal energy transferred during a shock tube experiment, the response of the resistance thermometer is directly comparable. As a result, from the known energy in the pulse, the properties represented by the value of k'' can be calculated. The average value of the calibration constant, determined from the electrical calibration, brackets the calculated value within plus or minus 15 per cent.

It was found to be a very difficult task to develop thin resistance thermometers which could withstand the extreme conditions, such as erosion due to dust and diaphragm fragments, without serious damage, as evidenced by a change of resistance. As a result, gages are calibrated and used for one run mostly, except in the low shock strength and low density region. There is considerable evidence that the damage which does occur happens after the interface arrives, that is, after the data has been taken. Typical heat-transfer gages, both the thin and the calorimeter type, are shown in Fig. 8.

Difficulties encountered with the thin resistance thermometers,* particularly at high Mach Numbers, led to the development of the calorimeter gage. Considering Eqs. (5) and (9), it can be determined that a metal of one characteristic thickness will absorb a large fraction of the heat flux incident upon it in 100 microsec. For platinum this thickness is approximately 0.003 cm. Such a strip of metal gives a response of one millivolt to a heat input of one kilowatt per square centimeter, which is the order of the minimum heat-transfer rates of interest in these experiments.

Because the gage is not infinitely thick, there will be some heat loss to the back-up insulator. This loss can be calculated and corrected, assuming a perfect contact between the metal and insulator. This loss, as a function of gage thickness and testing time is shown in Fig. 9. In an actual gage there is a small air space between the two materials, which materially reduce this loss.

The manufacture of calorimeter gages has been simplified to make the gages expendable, an almost necessary condition when making experiments with strong shock waves. A die-cut piece of platinum is cupped and mounted on a ground hemisphere-cylinder pyrex model by soldering it onto areas previously painted with the same platinum used for the thin gages. A four lead pattern, two to introduce the current and two to measure the resistance of a specific area, has been used to minimize the edge effects and aerodynamic disturbances caused by the wires and soldering. An

* Such as the large amount of work involved in the reduction of the oscillographic trace to heat-transfer data.

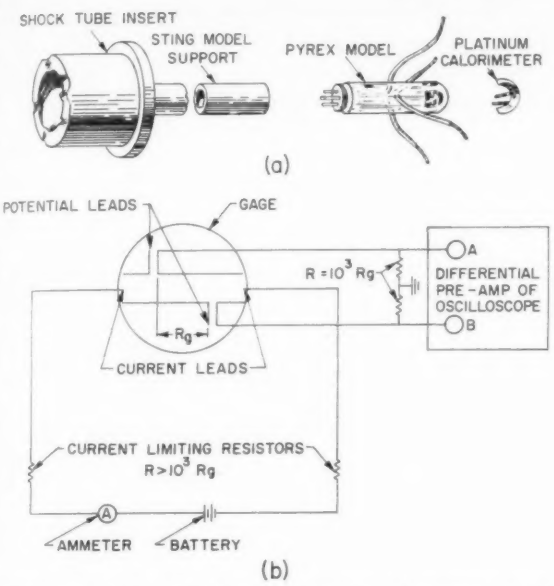

FIG. 10. Calorimeter heat-transfer gage (a) exploded view and (b) schematic. The gage area, between the two thin potential leads, covers an area of $\pm 20°$ surrounding the stagnation point. Heat-transfer data is corrected for the average over the gage area based on an assumed distribution (Newtonian pressure).

exploded view of a typical heat-transfer gage and circuit schematic are shown in Fig. 10. The gage covers a finite surface surrounding the stagnation point. The average heat-transfer rate over this surface has been calculated to be 94 per cent of the stagnation-point rate, assuming a Newtonian pressure distribution. A corresponding correction is made.

The properties of the gage material and insulator of interest for the calculation of heat-transfer data from calorimeter gage response are given in Eq. (9).

For the thicknesses of metal used, bulk properties are considered reliable. For chemically pure platinum, it has been estimated that the important properties, i.e., the heat capacity, density and temperature coefficient of resistivity are known within an accuracy of plus or minus 2 per cent.

The electrical calibration, previously described for the thin heat-transfer gages, has been successfully used to check the properties used for calorimeter gage data. The low resistance of the thermometer element, approximately 4×10^{-3} ohms, dictates the use of a 1,000-amp. pulse to produce energy dissipation in the gage comparable to the shock tube test transfer. It is difficult to produce a reasonably square pulse of this current amplitude, but a pulse whose current variations are known can be used to obtain the material properties. The properties thus determined check the manufacturer's data within plus or minus 10 per cent.

The details of analysis and experiences collected in the development of shock tube heat-transfer techniques are reported in reference 21.

RESULTS

The stagnation point of a blunt body has advantages which make it attractive for heat-transfer experiments. First, the most severe laminar heating occurs at this point; second, direct simulation of flight conditions—i.e., correct stagnation pressure and enthalpy independent of the Mach Number of the flow surrounding the model—can be accomplished at this point; and third, the problem of conductive, convective, and diffusive* heat transfer can be treated theoretically, limited only by the uncertainty of the transport properties at very high temperatures. However, calculations have been carried out over a range of viscosity, Prandtl Numbers and Lewis Numbers large enough to cover the most reasonable estimates that have been made for these parameters. This uncertainty in the calculated heat transfer is of the same order as the experimental scatter.

In addition, at the stagnation point of small models the radiative heat transfer is minimized by the small scale, whereas the aerodynamic heat transfer increases

* Heat transfer due to diffusion of atoms.

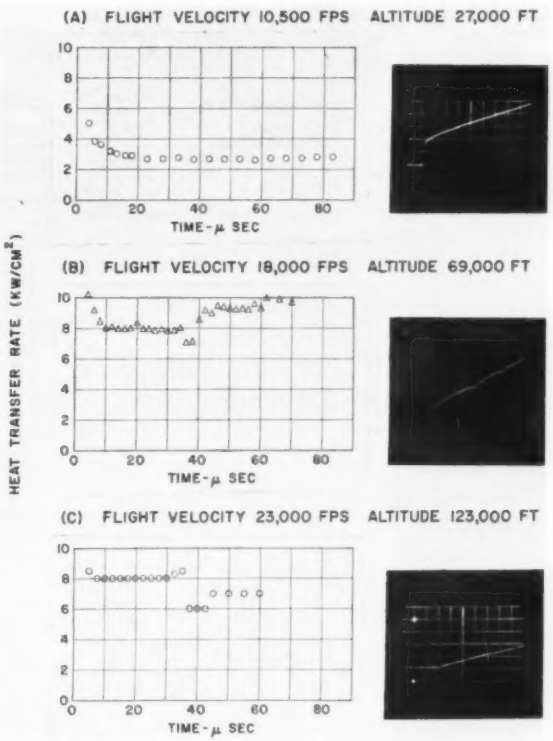

FIG. 11. Typical oscillographs and data. On all three oscillographs time increases from left to right. The sweep speed is 10 μsec./interval. The oscilloscope is triggered before the moving shock arrives at the stagnation point. The break in the horizontal trace denotes the arrival of the shock at the gage. The break of the curve accompanied by the end of the constant heat transfer denotes the arrival of the interface. (a) Record from a thin heat-transfer gage at a relatively low shock Mach Number. (b) Record from a thin heat-transfer gage to a higher shock Mach Number. Note that the extreme conditions at the high stagnation enthalpy degrade the quality of the signal. (c) Calorimeter gage record.

inversely with the radius ratio of the scaling. Thus, for a small, say 1/2-in., diameter hemisphere model compared to reasonable nose sizes, the ratio of radiative to aerodynamic heat transfer is suppressed by a very large factor, leaving measurements of purely aerodynamic heat transfer at high stagnation temperatures, even at 11,000°K.

The experiments were performed at the stagnation point of 1/2 in. diameter hemisphere-cylinder models, with either thin or calorimeter heat-transfer gages mounted at the stagnation point. A few experiments were performed on 1-in. diameter models in a 4-in. 100 ft. long shock tube. The pyrex models were ground and optically polished to the proper nose radius.

Oscillograms of the response from heat-transfer gages during a typical experiment are shown in Fig. 11. The thin gage has a parabolic response with time after the shock wave arrives at the gage. The oscilloscope is triggered a few microseconds before the arrival of the shock wave at the gage in order to record the initial portion of the curve. The output of the resistance element can be plotted against the square root of time, yielding directly, by use of the result of the gage calibration, the unknown heat-transfer rate, q. The records can also be analyzed by reading the output at many time intervals, and solving Eq. (11) for the heat-transfer rate, $q(t)$, as a function of time. The result of such an analysis is plotted in the left half of Fig. 11.

An oscillogram from a typical calorimeter gage is shown in the lower half of Fig. 11. The instantaneous variation of the output with time yields (from the values of the physical properties of the platinum strip as supplied by the manufacturer) the unknown heat-transfer rate, $q(t)$, at any time.

Fig. 12 presents the results of the experiments that have been performed. Three series of experiments at convenient initial shock tube pressures simulate hypersonic flight at altitudes of roughly 20,000, 70,000, and 120,000 ft. The velocity range covered extends from below the onset of chemical effects, at stagnation temperatures of about 3,000°K., to beyond the velocity required by a satellite to counteract the earth's gravitational field. The data were mostly taken with calorimeter gages. Points marked by triangles are from thin heat-transfer gage experiments. There seems to be a reasonable agreement between data from the two

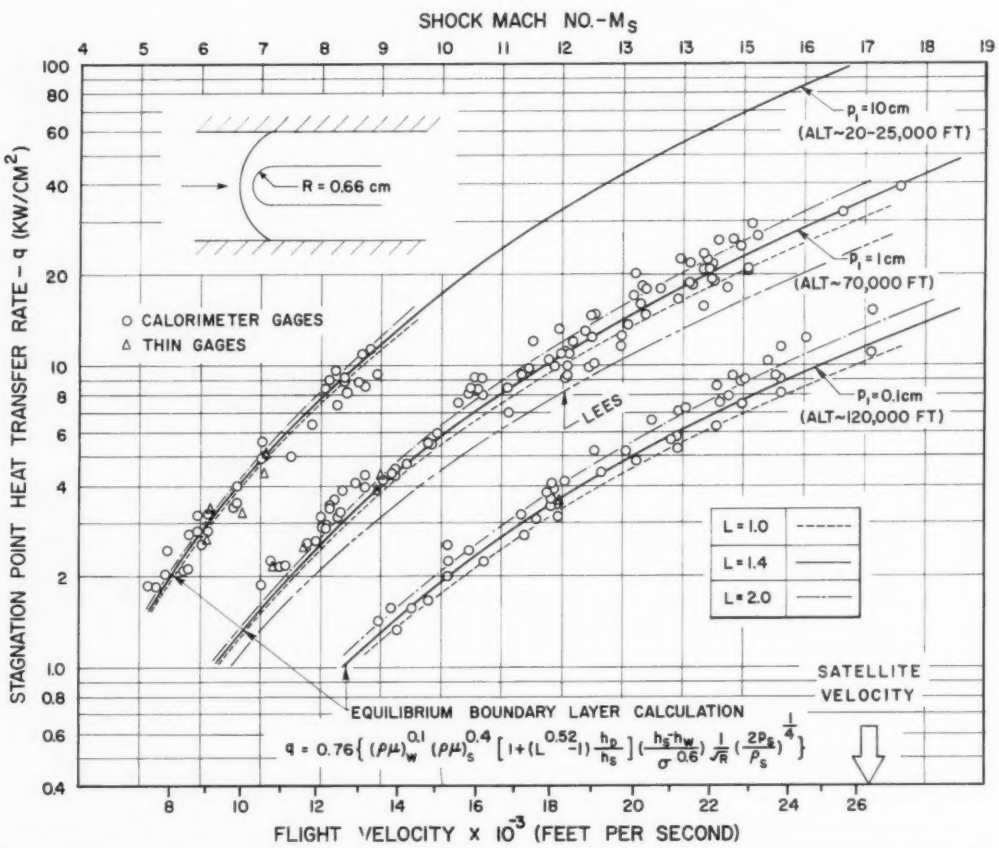
STAGNATION POINT HEAT TRANSFER MEASUREMENTS
SHOCK MACH NO.-M_S
4 5 6 7 8 9 10 11 12 13 13 15 16 17 18 19
STAGNATION POINT HEAT TRANSFER RATE - q (KW/CM^2)
100 80 60 40 20 10 8 6 4 2 1.0 0.8 0.6 0.4
R = 0.66 cm
p_1 = 10 cm
(ALT~20-25,000 FT)
p_1 = 1 cm
(ALT~70,000 FT)
p_1 = 0.1 cm
(ALT~120,000 FT)
○ CALORIMETER GAGES
△ THIN GAGES
LEES
L = 1.0
L = 1.4
L = 2.0
SATELLITE VELOCITY
EQUILIBRIUM BOUNDARY LAYER CALCULATION
$q = 0.76\{(\rho\mu)_w^{0.1}(\rho\mu)_s^{0.4}[1+(L^{0.52}-1)\frac{h_D}{h_s}](\frac{h_s-h_w}{\sigma^{0.6}})\frac{1}{\sqrt{R}}(\frac{2p_s}{\rho_s})^{\frac{1}{4}}\}$
8 10 12 14 16 18 20 22 24 26
FLIGHT VELOCITY X 10^{-3} (FEET PER SECOND)

FIG. 12. Measured stagnation point heat-transfer rates compared to the equilibrium boundary-layer theory of Fay and Riddell[3] and Lees.[1]

types of gages, considering the scatter in these types of measurements.*

The theoretical curve on Fig. 12 represents the result of the equilibrium boundary-layer calculations of Fay and Riddell.[3] The equilibrium solution for a Lewis Number of 1.4 and a Prandtl Number of 0.71 gives reasonable correlation to the experimental data within the scatter of the data and the uncertainties of the theory. The uncertainties in the calculated heat transfer are the uncertainties in the transport properties and the properties in the inviscid flow. The latter depend on the assumptions of thermodynamic equilibrium at the stagnation point and a Sutherland dependence of viscosity on temperature.

The consequences of this data can most easily be seen from the nondimensional form of the laminar stagnation point heat-transfer equations. The trend of the heat-transfer parameter, $Nu/\sqrt{Re}$, with flight velocity, characterized by the density ratio across the boundary layer, $(\rho\mu)_s/(\rho\mu)_w$, shows a decrease of a factor of two in the absolute value of the heat-transfer rate from a rate calculated from the low speed value of $Nu/\sqrt{Re}$ from Sibulkin,[18] 0.67 at $(\rho\mu)_s/(\rho\mu)_w = 1.0$, (as shown in Fig. 13) at the satellite velocity.

The Mach Number independence of the stagnation point simulation previously described has been confirmed by experiments conducted by the Cornell Aeronautical Laboratory[15] in a hypersonic shock tunnel. In this type of facility a gain in flow Mach Number is achieved by expanding air, which has been heated by an incident shock wave, in a large area ratio nozzle. By reducing the static temperature and speed of sound, a flow Mach Number of approximately five is achieved. Fig. 14 shows this data, reduced to the same conditions and scale as the straight shock tube data, correlated to the experiments reported here. These measurements, carried out by the Cornell Aeronautical Laboratory under subcontract from this program, were designed to support the present data by establishing the effect of changing the flow Mach Number from three to five. Even though this data has been taken at a relatively low stagnation temperature only, the measurements are in close agreement with the straight shock tube data.

The range of altitudes simulated by these experiments can be extended somewhat if one takes a closer look at the chemical kinetics of the flow over both scale and full size bodies. A simulation based on reproduction of the heat-transfer parameters, Nusselt Number and Reynolds Number, results in smaller actual boundary-layer thicknesses for the small scale model. The chemical kinetics of the boundary-layer problem—i.e., the similarity of the chemical changes in the boundary layer—are not simulated completely unless the boundary layer is completely in equilibrium

* More attention has been paid to data from the calorimeter instruments because at the high heat-transfer rates of these experiments the large temperature rise of the thin gages introduces additional corrections and inaccuracies.

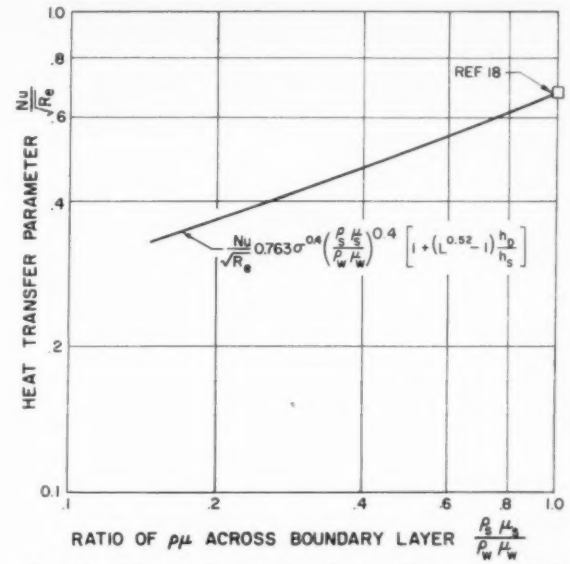
HEAT TRANSFER PARAMETER $\frac{Nu}{\sqrt{Re_e}}$
RATIO OF $\rho\mu$ ACROSS BOUNDARY LAYER $\frac{\rho_s \mu_s}{\rho_w \mu_w}$
REF 18
$\frac{Nu}{\sqrt{Re_e}} = 0.763\sigma^{0.4}\left(\frac{\rho_s \mu_s}{\rho_w \mu_w}\right)^{0.4}\left[1+\left(L^{0.52}-1\right)\frac{h_D}{h_s}\right]$

FIG. 13. Effect of the variation of the fluid properties, $(\rho\mu)$, through the equilibrium boundary layer, on the heat-transfer parameter, $Nu/\sqrt{Re}$, for Lewis Number of 1.4 and Prandtl Number of 0.71. (Shock tube at initial pressure of 1 cm. of Hg of air.)

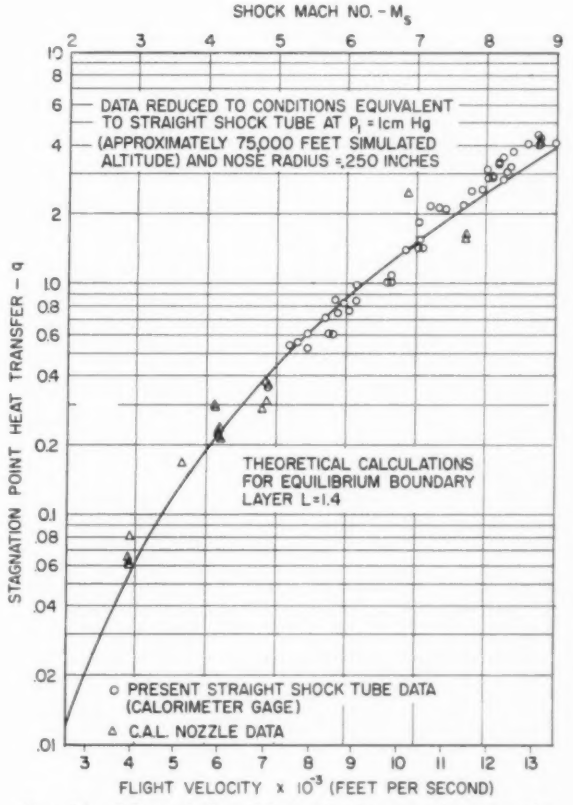
SHOCK MACH NO. - M_s
STAGNATION POINT HEAT TRANSFER - q
DATA REDUCED TO CONDITIONS EQUIVALENT TO STRAIGHT SHOCK TUBE AT P_1 = 1cm Hg (APPROXIMATELY 75,000 FEET SIMULATED ALTITUDE) AND NOSE RADIUS = .250 INCHES
THEORETICAL CALCULATIONS FOR EQUILIBRIUM BOUNDARY LAYER L=1.4
o PRESENT STRAIGHT SHOCK TUBE DATA (CALORIMETER GAGE)
△ CAL. NOZZLE DATA
FLIGHT VELOCITY x 10^{-3} (FEET PER SECOND)

FIG. 14. Effect of flow Mach Number on the stagnation point heat transfer on a hemisphere-cylinder body. CAL data from hypersonic shock tunnel with flow at Mach 4.5 to 5.0. Present straight shock tube data has a variation of flow Mach Number from approximately 2.3 to over 3.0.

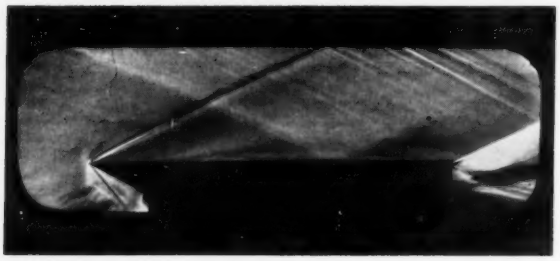

FIG. 15. Schlieren photograph of flow over a flat plate in a $1^1/_2$ in. inside diameter shock tube. The Mach angle should be 24.9° if the gas were in equilibrium, 26.2° if the vibrational relaxation were very slow, and 31.6° if the gas were completely frozen ($\gamma = 1.4$). Measured angles are 25.3°.

throughout or completely "frozen" throughout for both scale and full-size bodies. By "frozen" it is meant that the transit time of an atom or molecule through the boundary layer to the body surface is very short compared to the times required for recombination of the atoms. This means that the concentration of the chemical species in the inviscid flow at the edge of the boundary layer is frozen in the flow and remains constant throughout the boundary layer. In the intermediate range, one must consider the simulation of the stagnation enthalpy and the recombination rate parameter, as used in the solution of the nonequilibrium boundary layer with finite recombination rates.[3] The implication of this simulation is that the mechanism of heat transfer by conduction and atom diffusion is correctly duplicated. The recombination rate parameter is proportional to the product of the body radius and the square of the density and therefore experiments performed on small scale models at a given density altitude correspond to much higher simulated altitudes from the flow chemistry simulation point of view. This consideration, when applied to the present experiments, 0.250-in. nose radius, compared to a body one hundred times this size, extends the significance of this data to altitudes of almost 200,000 ft.

Knowledge of the conditions in the shock tube, in which the measurements have been made, depends on accurate measurement of the velocity of the shock wave as it moves down the tube, and on the assumption that the flow is in equilibrium behind the moving shock wave as well as behind the standing shock. The velocity measurement brings up the question of attenuation of the strength of the incident shock wave as it moves down the tubes. This question is further complicated for strong shocks by the properties of equilibrium air, which must be substituted for ideal gas relations. Several investigators have devoted much time and effort to a solution of this problem.[16,17] However, not much work has been extended to the strong shock case.

It is possible to circumvent this question in many cases, by making estimates of a tolerable degree of attenuation within the desired experimental accuracy. Testing time can then by sacrificed by changing the shock tube length to obtain the proper compromise.

Calculations to determine the effect of attenuation on the heat transfer measured at a given point in the tube have been made, using equilibrium properties for the air. This analysis shows that a very small correction can be made to the Mach Number, giving an effective Mach Number that would have caused the conditions in which the measurements were made. In general, extrapolating the shock-wave velocity to the point where the measurements are made is an accurate correction.

Despite these considerations, it has been convenient to hold the attenuation for all the data presented in this paper to less than 10 per cent of the initial shock Mach Number. A few runs made at high initial pressure where the wall boundary layer is turbulent with shock attenuations up to 20 per cent have been tolerated. Under this restriction, corrections to the extrapolated shock Mach Number have been calculated to be negligible.

Measurements behind grossly attenuating shock waves verify this procedure. Both the static pressure and heat-transfer rate have been measured to be constant with time at the value predicted from the extrapolated Mach Number.

In the shock tube, the question of the thermochemical state of the test gas is subdivided into (1) whether this gas is in equilibrium behind the incident shock as well as behind the standing shock wave at the stagnation point of blunt bodies, and (2) whether air starting in chemical equilibrium at the edge of the boundary layer remains so or is frozen at some composition as it flows through the boundary layer.

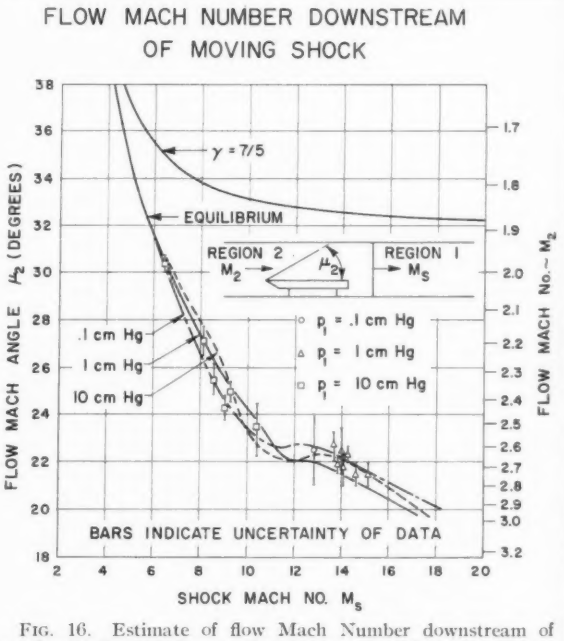

FIG. 16. Estimate of flow Mach Number downstream of moving shock, made from various assumptions about the thermochemical state of the air. Note that, in the equilibrium flow Mach Number estimate, the vibrational relaxation process across the disturbance has been considered.

The assumption that air in a shock tube comes to equilibrium very quickly behind the moving shock wave is probably very good in the light of available experimental data.[20] Measurements reported in reference 20 of the Mach angles in the flow over a flat plate, such as Fig. 15 (a technique similar to the one used to obtain pressure distributions), indicate that the flow is steady at the Mach Number predicted from equilibrium considerations. Fig. 16 shows the results from these measurements. It can be seen that the experimental results agree well with the Mach Number calculated from equilibrium considerations. Any other assumption regarding the state of the gas gave discernible deviations from the measured angles.

In addition, a number of other independent experiments performed at low initial pressure, where the relaxation time should be the longest (including heat-transfer measurements), can all be explained only from equilibrium assumptions.

It can be calculated that, if the flow were not to equilibrate across the moving shock wave nor at the stagnation point, the effect on the heat-transfer measurement would be, at the maximum, a decrease of 20 per cent at the extreme of the range covered by these experiments. At less severe conditions of dissociation, this correction would be much smaller.

The question of the chemistry of the air as it flows through the boundary layer, starting in equilibrium at its edge, has received much attention. This point has been thoroughly discussed by Fay and Riddell.[3] In the shock tube, the total heat transfer, whether the boundary layer is in equilibrium or is frozen at the edge conditions, remains almost unchanged, that is, within 5 per cent. For a typical model size, and based on the best recombination rate estimates, the large reduction of heat transfer that can be produced by a noncatalytic wall* in combination with the frozen boundary layer can be realized only at initial pressures lower than those covered by these experiments.

Conclusions

It has been shown that the environment encountered in hypersonic flight through the earth's atmosphere can be created in the laboratory in shock tubes. At the stagnation point, these conditions can be used for direct measurements of phenomena involving the boundary layer, such as aerodynamic heat transfer, on scale models simulating larger hypersonic vehicles.

These conditions have been used to make measurements of the stagnation point heat-transfer rates on hemisphere-cylinder models through a velocity range in which the dissociation of the air molecules at the stagnation point goes from zero to over 50 per cent, corresponding to satellite velocities. The measurements are compared to the boundary-layer theory developed by Fay and Riddell,[3] which accounts for the large variation of the fluid properties and for heat transferred by diffusion of atoms in the boundary layer. The data and theory show reasonably close agreement. The instrumentation and techniques developed for these measurements are briefly described.

* For a discussion of the effects of catalytic and noncatalytic body surfaces, see Fay and Riddell.[3]

References

[1] Lees, L., *Laminar Heat Transfer Over Blunt-Nosed Bodies at Hypersonic Flight Speeds*, Jet Propulsion, Vol. 26, p. 259–269, 1956.

[2] Cohen, C. B., and Reshotko, E., *Similar Solutions for the Compressible Laminar Boundary Layer with Heat Transfer and Pressure Gradient*, NACA TN 3325, 1955.

[3] Fay, J. A., and Riddell, F. R., *Theory of Stagnation Point Heat Transfer in Dissociated Air*, Journal of the Aeronautical Sciences, Vol. 25, No. 2, pp. 73–85, 121, February, 1958.

[4] Resler, E. L., Lin, S. C., and Kantrowitz, A. R., *The Production of High Temperature Gases in Shock Tubes*, Journal of Applied Physics, Vol. 23, pp. 1390–1399.

[5] Resler, E. L., *High Temperature Gases Produced by Strong Shock Waves*, Ph.D. Thesis, Cornell University, 1951.

[6] Bleakney, W., Weimer, D. K., and Fletchner, C. H., *The Shock Tube: A Facility for Investigations in Fluid Dynamics*, Review of Scientific Instruments, Vol. 20, pp. 807–815, November, 1949.

[7] Hilsenrath, J., and Beckett, C. W., *Tables of Thermodynamic Properties of Argon-Free Air to 15,000°K.*, USAF Arnold Engineering Development Center Report TN 56-12, September, 1956.

[8] Gilmore, F. J., *Equilibrium Composition and Thermodynamic Properties of Air to 24,000°K.*, Rand Corporation Research Memorandum RM-1543, August 24, 1955.

[9] Feldman, Saul, *Hypersonic Gas Dynamics Charts for Equilibrium Air*, Avco Research Laboratory, 1957.

[10] Masson, D. J., and Gazely, Carl, Jr., *Surface Protection and Cooling Systems for High Speed Flight*, Rand Corporation, P-829, March 23, 1956, revised April 16, 1956.

[11] Hertzberg, A., Smith, W., Glick, H. J., and Squire, W., *Modification of the Shock Tube for Generation of Hypersonic Flow*, Cornell Aeronautical Laboratory Report No. A. D.-789-A-2 (AEDC TN 55-15). March 1955.

[12] Blackman, V. H., *Vibrational Relaxation in Oxygen and Nitrogen*, Palmer Physics Laboratory, Princeton University Technical Report No. 2-20.

[13] Chaibai, A. J., and Emrich, R. J., *Measurement of Wall Temperature and Heat Flow in the Shock Tube*, Journal of Applied Physics, Vol. 26, p. 779, June, 1955.

[14] Rabinowitz, J., Jessey, M. E., and Baetsch, C. A., *Resistance Thermometer for Transient High Temperature Studies*, Journal of Applied Physics, Vol. 27, January, 1956.

[15] Cornell Aeronautical Laboratory, Inc. *Investigation of Stagnation Point Heat Transfer in the C.A.L. Hypersonic Shock Tunnel*, to be published.

[16] Trimpi, Robert L., and Cohen, Nathaniel B., *A Theory for Predicting the Flow of Real Gases in Shock Tubes with Experimental Verification*, NACA TN 3375, 1955.

[17] Mirels, H., *Attenuation in a Shock Tube due to Unsteady-Boundary-Layer Action*, NACA TN 3278, 1956.

[18] Sibulkin, M., *Heat Transfer Near the Forward Stagnation Point of a Body of Revolution*, Journal of Aeronautical Sciences, Vol. 19, No. 8, pp. 570–571, August, 1952.

[19] Vidal, R. J., *Model Instrumentation Techniques for Heat Transfer and Force Measurements in a Hypersonic Shock Tunnel*, Cornell Aeronautical Laboratory, Inc. Report No. 40-917-A-1, February, 1956.

[20] Feldman, S., *The Chemical Kinetics of Air at High Temperature: A Problem in Hypersonic Aerodynamics*, Avco Research Laboratory, Research Report 4, February, 1957.

[21] Brown, Herbert K., and Rose, Peter H., *A Critical Analysis of the Uncertainties Involved in Shock Tube Heat Transfer Measurements*, Avco Research Laboratory Research Report 10 (To be published).

Analysis of Elliptical Rings for Monocoque Fuselages

STANLEY KAUFMAN*

Aircraft Armaments, Inc.

SUMMARY

J. A. Wise[1] solved for the external and internal forces of a prismatic ring subjected independently or collectively to any combination of three generalized loading conditions parallel to the plane of the ring—a radial force, a tangential force, and an applied moment anywhere on the ring.

This paper is a natural extension of his work as it considers the more general shape, the prismatic elliptical ring subjected to the following three loading conditions parallel to the plane of the ring: first, a force parallel to the major axis; second, a force parallel to the minor axis; and third, an applied moment anywhere on the ring.

INTRODUCTION

ALTHOUGH THERE IS much information available in the literature on proposed methods of solving for internal forces in a ring of generalized shape[2,3] under generalized loading, exact solutions have by necessity been limited to the simpler geometric shapes such as the circle.[1,4–6] For certain specific loading conditions formal solutions have also been obtained for the ellipse.[7]

The analysis is subjected to the following assumptions: (1) centroidal axis of the ring and the line of shear flow are coincident, (2) strain energy due to shear and thrust are negligible compared to that of bending, and (3) resisting shear flow is distributed according to the elementary (VQ/I) beam theory.

ANALYSIS

The equation of the ellipse shown in Fig. 1 is

$$y = K'\sqrt{a^2 - x^2}$$

Let us now introduce a change in variables by letting

$$x = a \sin r, \quad y = K'a \cos r$$

$$ds = \sqrt{dx^2 + dy^2} = a\sqrt{1 - K^2 \sin^2 r}\, dr$$

where $K^2 + K'^2 = 1$

$$x_1 = a \sin z, \quad y_1 = K'a \cos z$$

The statical moment about the y-axis, Q_y, is

$$Q_y = \int_x^{x=a} x\, ds = a^2[A - A(K, r)]$$

where

$$A(K, r) = \int_0^r \sin\phi \sqrt{1 - K^2 \sin^2\phi}\, d\phi =$$

$$\frac{1}{2}(1 - \cos r \sqrt{1 - K^2 \sin^2 r}) + \frac{1 - K^2}{2K} \times$$

$$\ln \frac{(K + 1)}{(K \cos r + \sqrt{1 - K^2 \sin^2 r})}$$

for $0 < k < 1$, A being the complete integral between $r = 0$ and $r = \pi/2$.

The moment of inertia about the y-axis, I_{yy}, is

$$I_{yy} = 4\int_0^{x=a} x^2 ds = 4a^3G$$

where[8]

$$G(K, r) = \int_0^r \sin^2\phi \sqrt{1 - K^2 \sin^2\phi}\, d\phi =$$

$$-\frac{1}{3}\sqrt{1 - K^2 \sin^2 r} \sin r \cos r +$$

$$\frac{(2K^2 - 1)}{3K^2} E(K, r) + \frac{K'^2}{3K^2} F(K, r)$$

for $0 < k < 1$, where $E(K, r)$ and $F(K, r)$ are elliptic integrals of the second and first kinds, respectively:

$$E(K, r) = \int_0 \sqrt{1 - K^2 \sin^2\phi}\, d\phi, \quad F(K, r) =$$

$$\int_0^r \frac{d\phi}{\sqrt{1 - K^2 \sin^2\phi}}$$

G being the complete integral between $r = 0$ and $r = \pi/2$.

The shear stress q can now be calculated as

$$q = P[\pm Q_y/I_{yy} \pm y_1 \Big/ 4\int_0^{x=a} (y\,dx - x\,dy)]$$

$$= P/4a\{\pm [A - A(K, r)]\, G \pm 2 \cos z/\pi\}$$

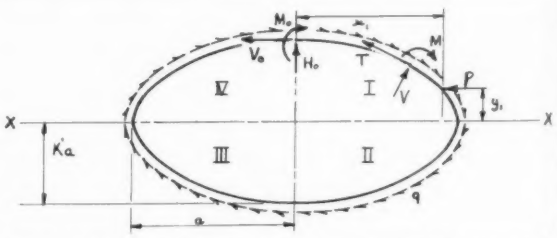

FIG. 1. Applied and internal forces, force parallel to major axis.

Received April 16, 1957. Revised and received September 13, 1957.

* Design Engineer.

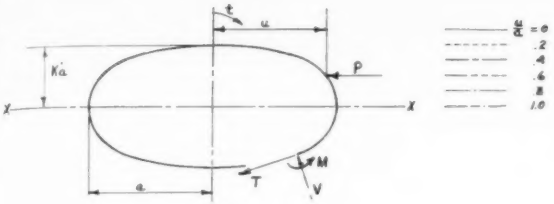

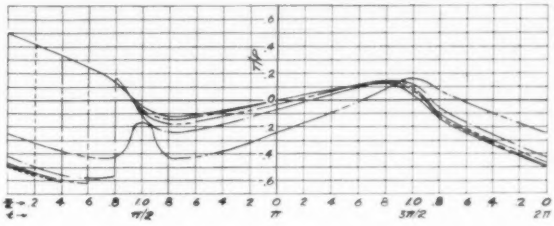

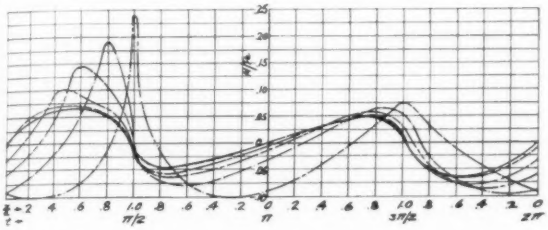

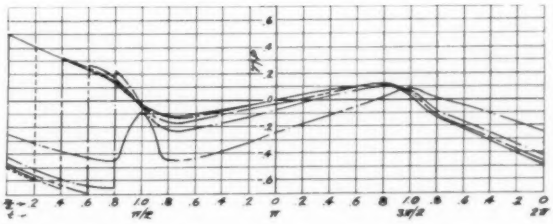

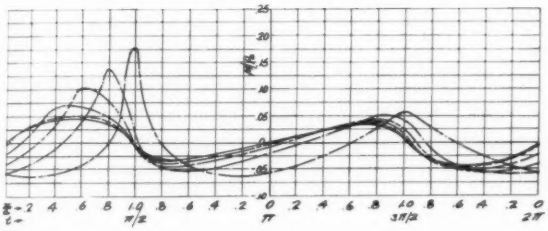

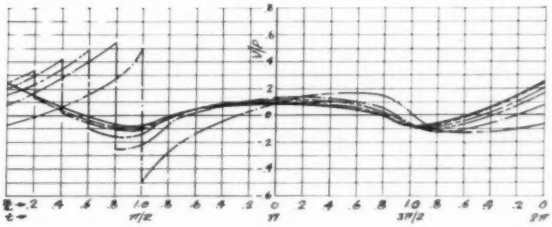

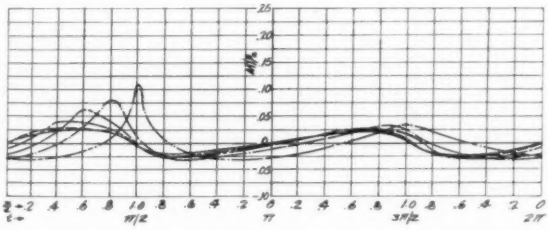

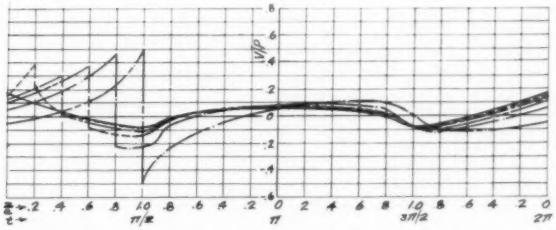

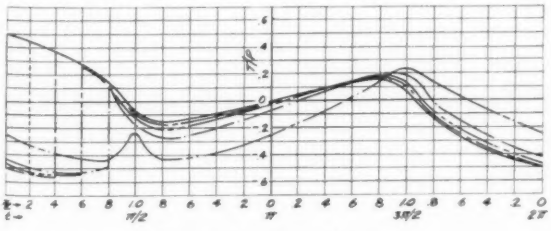

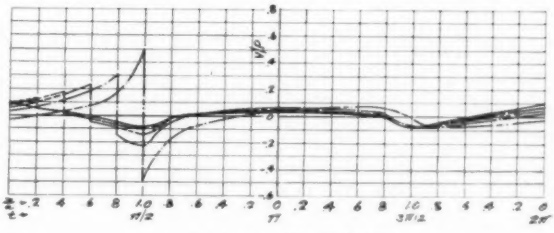

FIGS. 2–6. *Top to bottom.*
FIG. 2. Force parallel to major axis.
FIG. 3. M/Pa vs. x/a for $K' = 1.0$.
FIG. 4. M/Pa vs. x/a for $K' = 0.7$.
FIG. 5. M/Pa vs. x/a for $K' = 0.4$.
FIG. 6. T/P vs. x/a for $K' = 1.0$.

FIGS. 7–11. *Top to bottom.*
FIG. 7. T/P vs. x/a for $K' = 0.7$.
FIG. 8. T/P vs. x/a for $K' = 0.4$.
FIG. 9. V/P vs. x/a for $K' = 1.0$.
FIG. 10. V/P vs. x/a for $K' = 0.7$.
FIG. 11. V/P vs. x/a for $K' = 0.4$.

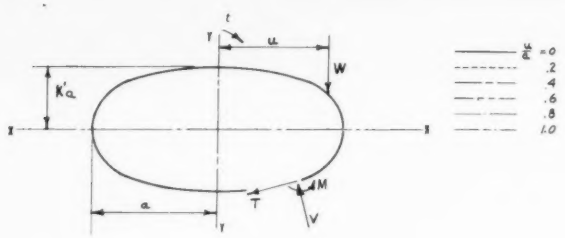

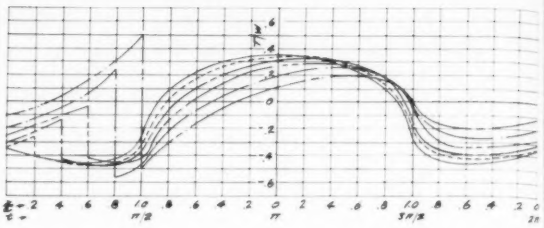

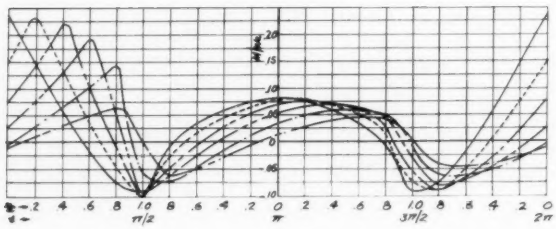

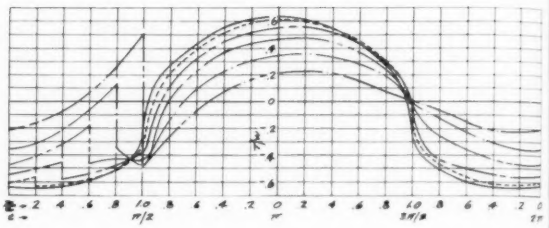

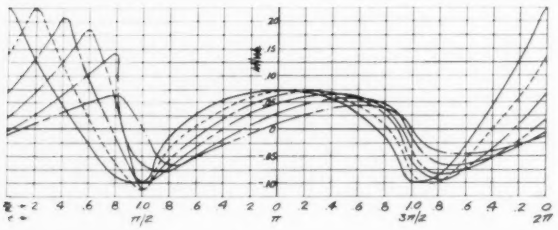

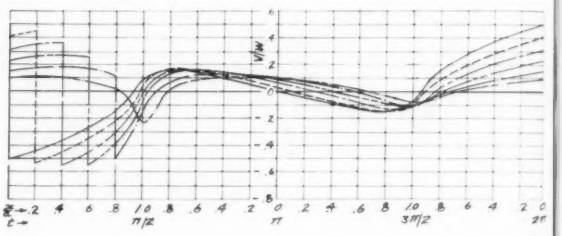

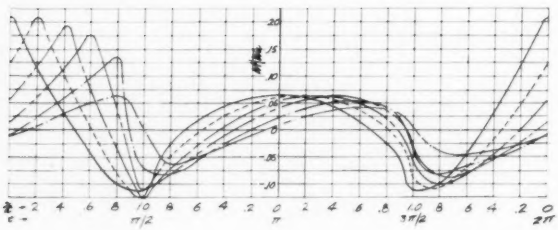

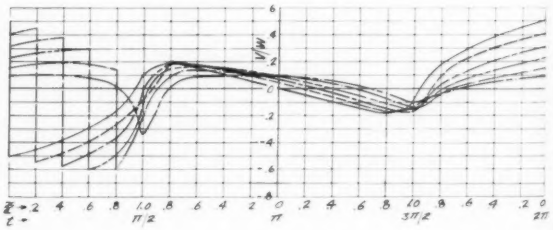

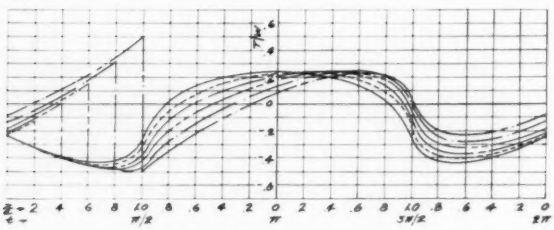

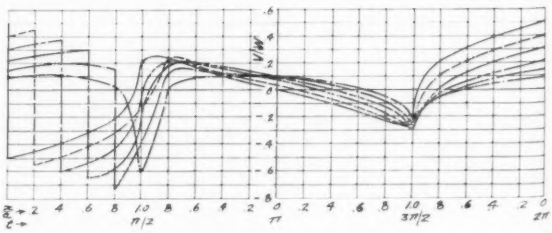

FIGS. 12–16. *Top to bottom.*
FIG. 12. Force parallel to minor axis.
FIG. 13. M/Wa vs. x/a for $K' = 1.0$.
FIG. 14. M/Wa vs. x/a for $K' = 0.7$.
FIG. 15. M/Wa vs. x/a for $K' = 0.4$.
FIG. 16. T/W vs. x/a for $K' = 1.0$.

FIGS. 17–21. *Top to bottom.*
FIG. 17. T/W vs. x/a for $K' = 0.7$.
FIG. 18. T/W vs. x/a for $K' = 0.4$.
FIG. 19. V/W vs. x/a for $K' = 1.0$.
FIG. 20. V/W vs. x/a for $K' = 0.7$.
FIG. 21. V/W vs. x/a for $K' = 0.4$.

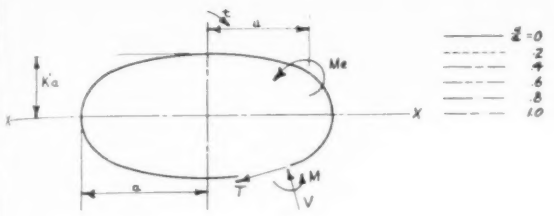

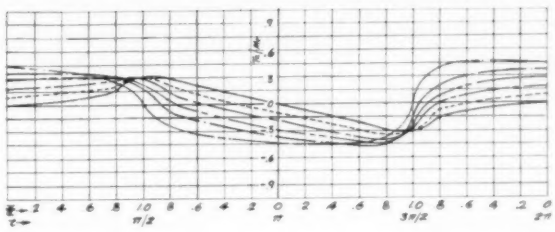

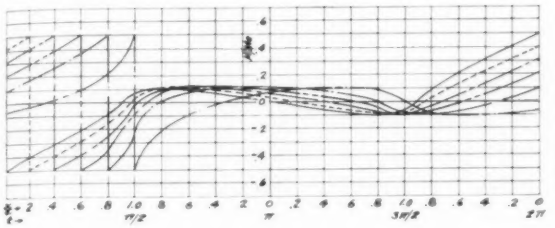

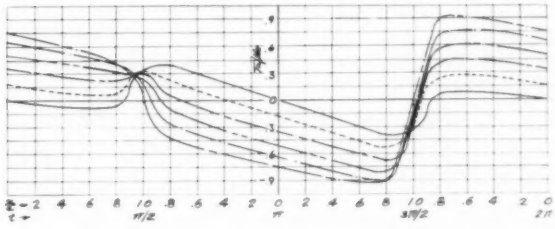

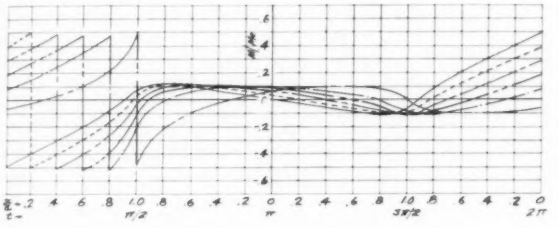

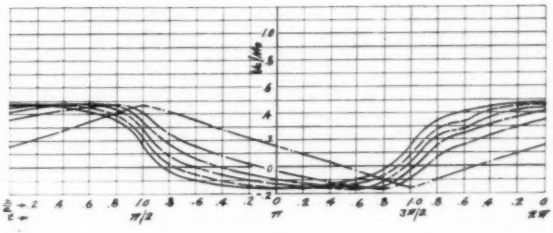

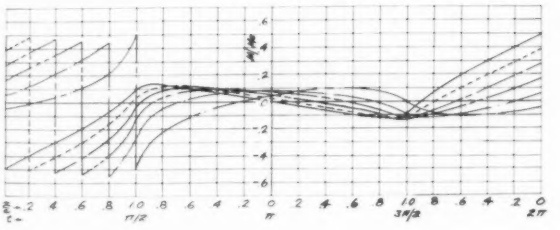

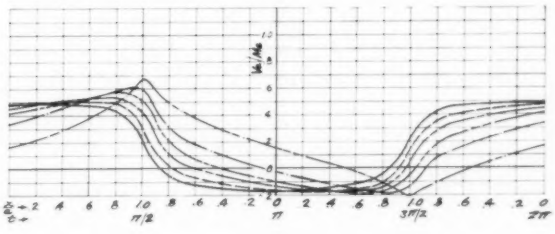

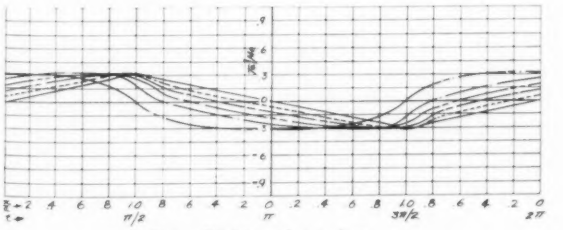

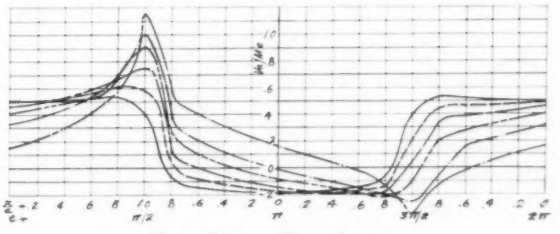

FIGS. 22–26. *Top to bottom.*
FIG. 22. Applied moment.
FIG. 23. M/M_e vs. x/a for $K' = 1.0$.
FIG. 24. M/M_e vs. x/a for $K' = 0.7$.
FIG. 25. M/M_e vs. x/a for $K' = 0.4$.
FIG. 26. Ta/M_e vs. x/a for $K' = 1.0$.

FIGS. 27–31. *Top to bottom.*
FIG. 27. Ta/M_e vs. x/a for $K' = 0.7$.
FIG. 28. Ta/Me vs. x/a for $K' = 0.4$.
FIG. 29. Va/M_e vs. x/a for $K' = 1.0$.
FIG. 30. Va/M_e vs. x/a for $K' = 0.7$.
FIG. 31. Va/M_e vs. x/a for $K' = 0.4$.

Expressions can now be written for bending moment[9] for quadrants I, II, III, and IV in terms of the loading, resistant shear flow, and the three redundants M_0, H_0, and V_0. One can form, in the usual manner, three linear independent equations from the following integrals by integrating over the entire ellipse:

$$\int M\frac{\partial M}{\partial M_0}ds = 0, \quad \int M\frac{\partial M}{\partial H_0}ds = 0, \quad \int M\frac{\partial M}{\partial V_0}ds = 0$$

After solving for M_0, H_0, and V_0, equations are obtained for bending moment (M), thrust (T), and shear (V) in terms of the known parameters.[9] A similar procedure can be followed for the other two loading conditions and coefficients then calculated for M, T and V. The accompanying graphs represent these coefficients.

Conclusions

In the usual airframe construction the centroidal axis of the ring does not exactly coincide with the shear flow in the skin, attached to the outside flange of the ring. It is good practice to choose the greater skin dimensions rather than the dimensions of the centroidal axis of the ring to be on the conservative side.

One can resolve any load parallel to the plane of the ring into one or more of the three generalized loading conditions considered in this paper. Furthermore, one can superimpose the shear flows, bending moments, shears, and thrusts resulting from any combination of these loading conditions, as the theorem of superposition for small deflections is valid here.

References

[1] Wise, J. A., *Analysis of Circular Rings for Monocoque Fuselages*, Journal of the Aeronautical Sciences, Vol. 6, No. 11, pp. 460–463, September, 1939.

[2] Lundquist, E. E., and Burke, W. F., *General Equations for the Stress Analysis of Rings*, NACA TR 509, 1934.

[3] Liepmann, Hans P., *Stress Analysis for Rings with One Axis of Symmetry*, Journal of the Aeronautical Sciences, Vol. 7, No. 12, pp. 509–512, October, 1940.

[4] Greenwood, Ernest, J. A., Jr., *A Method of Stress Analysis of Monocoque Fuselage Circular Rings*, Journal of the Aeronautical Sciences, Vol. 3, No. 12, pp. 440–443, October, 1936.

[5] Miller, R. W., and Wood, K. D., *Formulas for the Stress Analysis of Circular Rings in a Monocoque Fuselage*, NACA TN 462, 1933.

[6] Niles, A. S., and Newell, J. S., *Airplane Structures*, Vol. II, John Wiley and Sons, Inc., New York, 1943.

[7] Burke, W. F., *Working Charts for the Stress Analysis of Elliptical Rings*, NACA TN 444, 1933.

[8] Legendre, A. M., *Traité des Fonctions Ellipiques*, Vol. I, Imprimeriede Huzard-Courcier, Paris, 1825.

[9] Kaufman, S., *Theory and Design Coefficients of Elliptical Rings*, an essay submitted to the Advisory Board of the School of Engineering of the Johns Hopkins University in conformity with the requirements for the degree of Master of Science in Engineering, 1957.

Faculty of Science of the University of Paris

Symposium on Rarefied Gas Dynamics and Aerothermodynamics

Centre Universitaire Méditerranéen, Nice, France, July 2–5, 1958

This Symposium will be mainly concerned with the present position in regard to research being carried out on Rarefied Gas Dynamics and Aerothermodynamics. It will include theoretical and experimental studies on (1) aerodynamic and thermodynamic phenomena in highly rarefied atmospheres; (2) fundamental physical values that occurred in the preceding investigations—that is, on the accommodation coefficient and exchange momentum coefficients; and (3) apparatus and methods of measurement that relate to the field already covered in previous investigations.

Participants should submit a title and brief outline of the proposed paper as soon as possible to the Secretary: *Dr. F. M. Devienne, Laboratoire Méditerranéen de Recherches Thermodynamiques, 2 Avenue Villebois Mareuil, Nice, France.*

The Effects of Afterbody Length and Mach Number on the Normal Force and Center of Pressure of Conical and Ogival Nose Bodies

WILLIAM E. BUFORD*

Ballistic Research Laboratories, Aberdeen Proving Ground

SUMMARY

Measurements have been made of the normal force and center of pressure of bodies of revolution at supersonic Mach Numbers from 1.36 to 4.0. Conical and ogival nose bodies, with cylindrical afterbody lengths varying systematically from 0 to 11 calibers, were studied. The purpose of this study was to describe in a systematic manner the variation of the body aerodynamic characteristics with afterbody length and Mach Number. These data are in reasonable agreement with the theoretical values predicted by Van Dyke's improved treatment of the first-order axial and cross flows.

SYMBOLS

q	= dynamic pressure = $\gamma P_{t_s} M^2$
P_{t_s}	= test section pressure
γ	= ratio of specific heats = 1.405
M	= Mach Number
α	= angle of attack
C_N	= N/qS
$dC_N/d\alpha$	= normal force coefficient slope per degree
N	= normal force
S	= maximum cross-sectional area of body = $\pi d^2/4$
d	= maximum body diameter
l	= body length
l/d	= fineness ratio
C.P.	= center of pressure

INTRODUCTION

THE EFFECTS of fineness ratio and Mach Number on the normal force and center of pressure of bodies of revolution are of considerable interest in missile design. Many current missile configurations employ long bodies in the design, and in many cases the contribution of the body to the total normal force is equal to or greater than that contributed by the lifting surfaces. The forward center of pressure of the body makes it difficult to stabilize such missiles throughout the required Mach Number range.

The art of missile design has been handicapped by a lack of systematically acquired information describing the aerodynamic variations of bodies with fineness ratio, Mach Number, and differing nose configuration. The existing experimental data are usually limited to describing the effects of one particular variable, or a description of a particular missile configuration. Extensive theoretical investigations have been made in attempts to predict the desired information accurately. However, most of the theoretical solutions have suffered from inherent defects from the standpoint of accuracy, and from the time and effort required to perform the calculations. A constructive approach to these limitations was made by Van Dyke[1] in a paper in which better accuracy was indicated by an improved treatment of the first-order solution. In the present paper a description is presented of the experimental normal force and center of pressure variations with several of the physical body parameters and with Mach Number. In addition to their direct practical value in design, the results may be utilized for evaluating the theoretical solutions.

MODELS

In preparing a systematic program of this type, it is necessary to decide which physical parameters are most important aerodynamically, and, therefore, which ones are to be varied. For bodies of revolution the parameters we have chosen are (1) nose type (ogive or cone) and (2) afterbody length. The parameters were chosen and varied in a manner so that the results are readily adaptable for use in missile design practice.

Two basic nose shapes were chosen—a 10° half angle cone and a tagent ogive of the same length of the cone. The nose was 2.84 calibers long and the ogive had a radius of 8.29 calibers. Drawings of the models appear in Fig. 1, and a photograph of the models and balance can be seen in Fig. 2. Incremental lengths of cylindrical afterbody were added up to a maximum fineness ratio of 13.84.

The region of the nose-body juncture is important because of normal force carry-over from the nose to the body. Therefore in this region incremental lengths of

Received October 31, 1955. Resubmitted September 10, 1957.

* Formerly, Aerodynamic Engineer, Supersonic Wind Tunnels Branch. Now, Group Engineer, Systems Analysis Department, Denver Division of The Martin Company.

The author wishes to acknowledge the valuable contributions made by several people to this work. The theoretical calculations were performed at the direction of Stanley Shatunoff, who was formerly an Aerodynamic Engineer at the Supersonic Wind Tunnels Branch. The impetus for the experiments was provided by Charles L. Poor, who was Chief of the Supersonic Wind Tunnels Branch at the initiation of the program. The mathematical computations for the theoretical work was done by Miss Mary Jane Cox, Chief of the Wind Tunnel Computing Section.

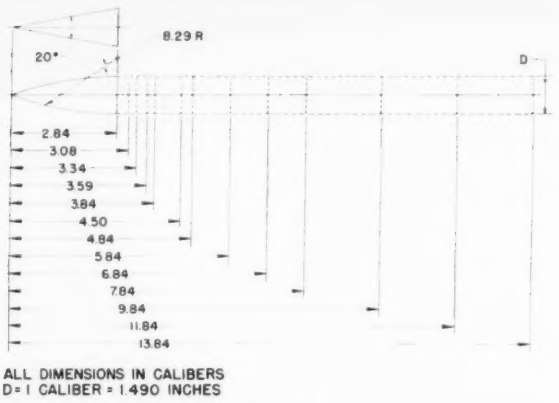

FIG. 1. Drawing of models.

0.25 calibers were used. As the body lengthened the increments were increased to 2 calibers. These variations are presented in Fig. 2. At Mach Number 1.36, reflected shock wave interference limited the fineness ratio to 7.

APPARATUS

The Aberdeen supersonic wind tunnel is a variable density, continuously operating type. The maximum Mach Number deviation in the test section is ±0.015. A photograph of the wind-tunnel test section appears in Fig. 3.

The measurements were made with each of two strain-gage balances. The balances are shown in Figs. 4 and 5. The balance shown in Fig. 4 combines a normal force beam and moment beam arrangement wherein the moment beam is integral with the strut. The balance shown in Fig. 5 measures the normal force in two parts and may also be used to measure the drag.

TEST CONDITIONS

Tests were conducted at Mach Numbers 1.36, 1.72, 3.02, 3.55, and 4. The Reynolds Number was varied by changing the tunnel supply pressure. The test conditions are summarized in Table 1. The Reynolds Number is based on the maximum body diameter (1.49 in.). In some cases data were obtained up to an angle of attack of 16° (see reference 2). However, for the purpose of this paper only the data at small angles (±3°) are used. Photographs of the flow appear in Figs. 6 and 7.

ACCURACY OF RESULTS

From a consideration of calibration data, flow uniformity, and data repeatability, it is believed that the measurements are accurate to within ±0.004 in terms of C_N and 0.15 caliber in center of pressure. The normal force coefficient slope is believed to be accurate to within ±2 per cent. A measure of the validity of the results is obtained from the close agreement of the cone alone measurements with the results of the Stone-Kopal exact solution (see Fig. 8).

TABLE 1

Mach Number	Test Reynolds Number (Based on Body Diameter)	Dynamic Pressure (psi)
1.36	0.96×10^6	7.49
1.72	0.65×10^6	7.87
3.02	$0.25 \times 10^6, 0.63 \times 10^6$	2.61, 6.52
3.55	$0.8 \times 10^6, 0.46 \times 10^6$	1.67, 4.17
4.0	$0.13 \times 10^6, 0.49 \times 10^6$	1.03, 4.26

The angles of attack were corrected for a strut deflection due to aerodynamic load and for flow deviation in the tunnel. In computing center of pressure in the small angle range, slopes of the normal force and moment curves were used. For the small angles considered, the relationship of C_N versus α was linear and $dC_N/d\alpha$ was obtained by graphical means.

RESULTS

(a) Fineness Ratio Effects on Normal Force

The variation of the normal force coefficient slope with fineness ratio and Mach Number is summarized for the ogival and conical nose bodies in Figs. 9 and 10, respectively. Examination of the results reveal several interesting characteristics. There is a pronounced increase in $dC_N/d\alpha$ as afterbody is added to the nose; in general, after the afterbody attains a certain length,

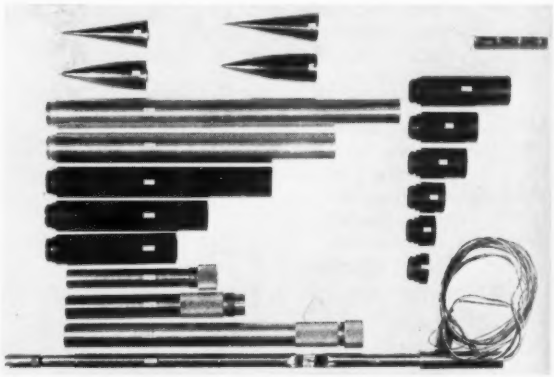

FIG. 2. Photograph of models and balance.

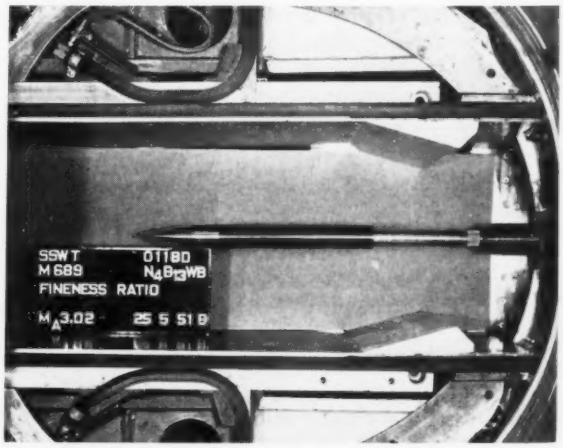

FIG. 3. Photograph of model installed in wind tunnel.

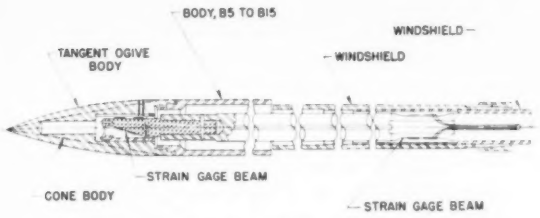

FIG. 4. Drawing of moment balance.

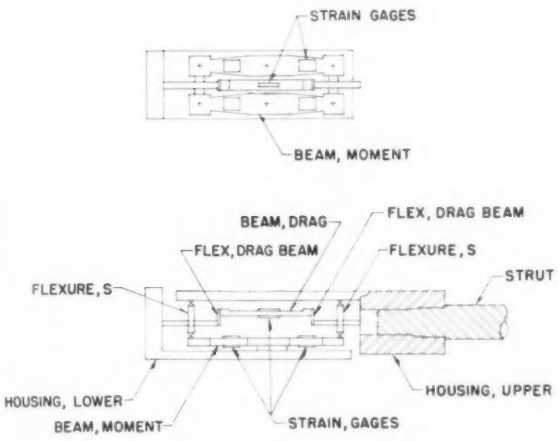

FIG. 5. Drawing of normal force balance.

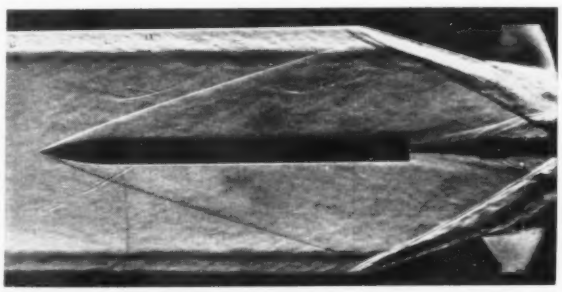

FIG. 6 Photograph of flow about ogive nose body with fineness ratio = 13.84, $M = 4$, $\alpha = 0°$.

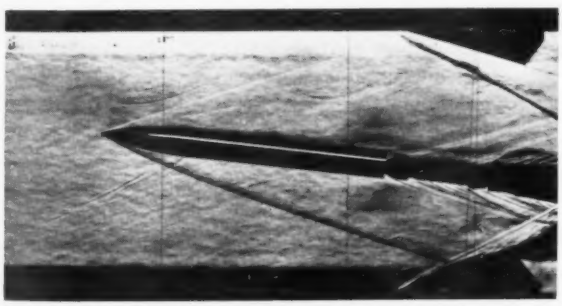

FIG. 7. Photograph of flow about ogive nose body with fineness ratio = 9.84, $M = 3.8$, $\alpha = 6°$.

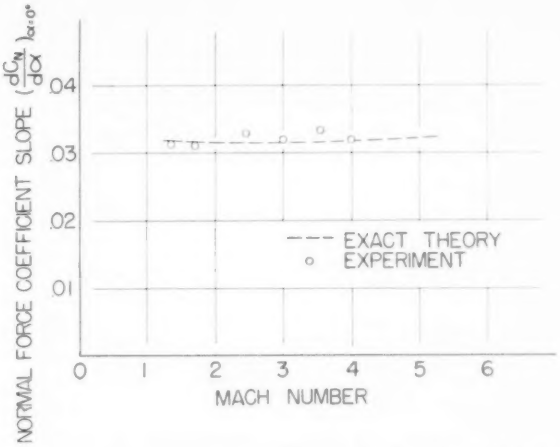

FIG. 8. Comparison of experimental values of normal force coefficient slope with values from exact theory for 10° half angle cone.

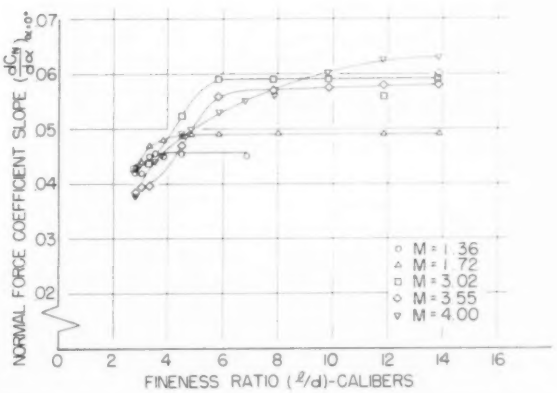

FIG. 9. Variation of normal force coefficient slope with fineness ratio for ogive nose body.

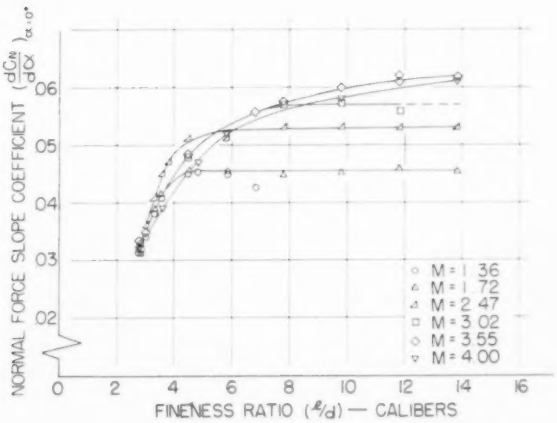

FIG. 10. Variation of normal force coefficient slope with fineness ratio for cone nose body.

little or no increase results from further extensions. For the conical nose, the increase in $dc_N/d\alpha$ with addition of afterbody length is constant at all Mach Numbers for afterbody lengths up to 1 caliber. At this length, deviations occur for different Mach Numbers. Also, $dc_N/d\alpha$ becomes constant at some length dependent upon the Mach Number. The ogival nose configuration exhibits the increase in $dc_N/d\alpha$ with increased afterbody, and $dc_N/d\alpha$ attains a maximum at a fineness ratio of about 7 or less for all Mach Numbers. However, a Mach Number effect is immediately apparent as the body is lengthened. These data seem to positively establish the existence of a potential normal force carry-over onto the afterbody; the magnitude of carry-over and the length of afterbody affected are a function of nose shape and Mach Number. This normal force is in contrast with the force developed by viscous effects. That is, a normal force is developed on the cylindrical afterbody by the potential flow.

As the afterbody continues to be lengthened, one would expect a progressive reduction of the normal force carry-over, and this effect seems apparent in most of these results. However, there is a possibility of a gradual progressive increase in $dc_N/d\alpha$ because of increased effective base area due to boundary-layer displacement thickness. This might explain the progressive small increase in $dc_N/d\alpha$ for both the cone and ogive nose bodies at Mach Numbers 3.55 and 4. However, this possible effect seems to require more careful study. Because of the lower pressure on the upper surface of bodies, there may be a tendency for the boundary-layer fluid to accumulate on the body's upper surface. This distortion may tend to cancel expected effects of an effective larger base area due to increased boundary-layer thickness. In connection with this study, tests were made in which, on very long bodies, increased displacement thickness was caused by a nose transition strip. No measurable differences in $dc_N/d\alpha$ occurred with or without the transition strip.

(b) *Mach Number Effects on Normal Force*

In regard to Mach Number effects, these data substantiate previous experimental results which have shown an increase in $dc_N/d\alpha$ with increasing Mach Number up to a certain limit. This is characteristic of pointed nose bodies.

Any Reynolds Number effect on $dc_N/d\alpha$, associated with the increasing length, would be included in the effect of fineness ratio. However, for two Mach Numbers the Reynolds Number was varied and the effects on $dc_N/d\alpha$ were undetectable.

There appears to be a Mach Number where a maximum $dc_N/d\alpha$ is reached and further increase tends to reduce $dc_N/d\alpha$. This phenomenon may be distinctly observed in the ogival nose data where a maximum is reached at 3.02 and the values at 3.55 and 4 are less. Also for the cone, $dc_N/d\alpha$ at Mach Number 4 is smaller than it is at Mach Number 3.55.

(c) *Center of Pressure*

The increase in $dc_N/d\alpha$, whether caused by increased fineness ratio or Mach Number, is associated with a rearward movement of the center of pressure. This may be observed in Figs. 11 and 12. This, of course, is expected since the increased normal force is contributed by the afterbody. In most cases $dc_N/d\alpha$ and center of pressure position become constant at the same fineness ratio. One exception is the data for the ogival nose body at Mach Number 4; here the center of pressure location is constant above a length of 8 calibers whereas $dc_N/d\alpha$ continues to increase. In actual missile practice this rearward movement of the center of pressure with increased body length may not be as helpful as it appears since associated with it is the increase in the body normal force contribution.

Evaluation of Theory

(a) *Improved First-Order Theory*

Van Dyke, in a recent paper,[1] made several important contributions, among which are an improved treatment of first-order theory, a second-order solution to the exact perturbation equations for use in the zero lift case, and the suggestion of a hybrid theory combining first-order and second-order solutions for the lifting case. He notes that in usual first-order theory, several approximations are made on the basis that the mathematical order of the terms neglected is no greater than the terms previously dropped in linearizing the equations of motion. He demonstrates that the physical magnitude of error may be many times larger and that while in many cases linearizing the pressure relationship proves disastrous, greatly improved agreement is obtained with the exact expression. Van Dyke's hybrid theory has been used to predict the pressure and normal force on several particular body shapes, and quite good agreement has been obtained. It is of interest to determine whether the theory has merit when applied to more general configurations.

(b) *Solutions Used in Comparison*

The results of the present study provide a criterion for an evaluation of Van Dyke's suggestions. This is so because we are concerned both with the flow at the nose and also the carry-over onto long afterbodies. Theoretical calculations were performed for the lifting case of the variable length bodies with the ogive nose. Two differing calculations were used: (1) a first-order solution wherein the exact pressure relation and the exact tangency condition were applied, and (2) a calculation wherein the numerical method of characteristics was used for the axial flow and a first-order solution was used for the cross flow. This latter differs from Van Dyke's hybrid theory to the extent that the exact solution rather than the second-order solution was used for the axial flow. In all cases, the theoretical values are presented in terms of the normal force coefficient, C_N.

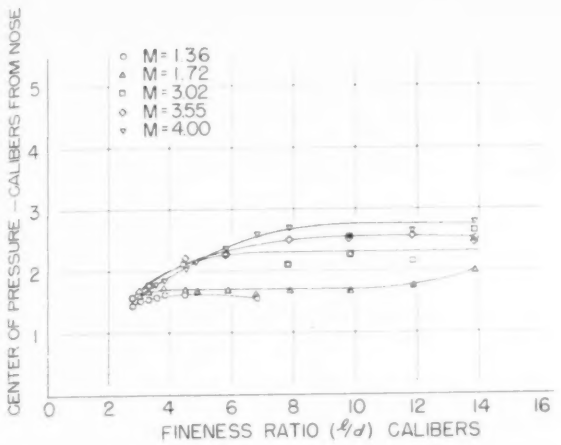

FIG. 11. Variation of center of pressure location with fineness ratio for ogive nose body.

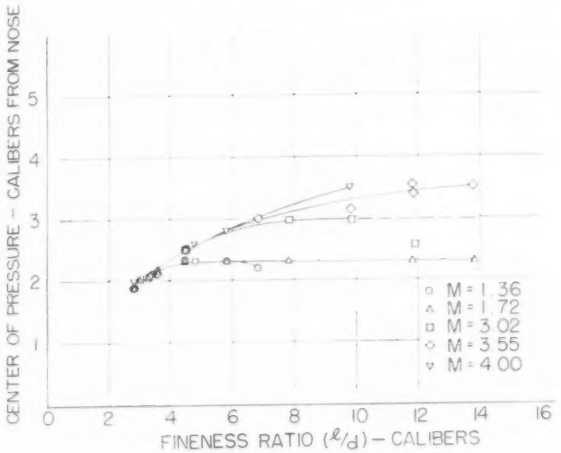

FIG. 12. Variation of center of pressure location with fineness ratio for cone nose body.

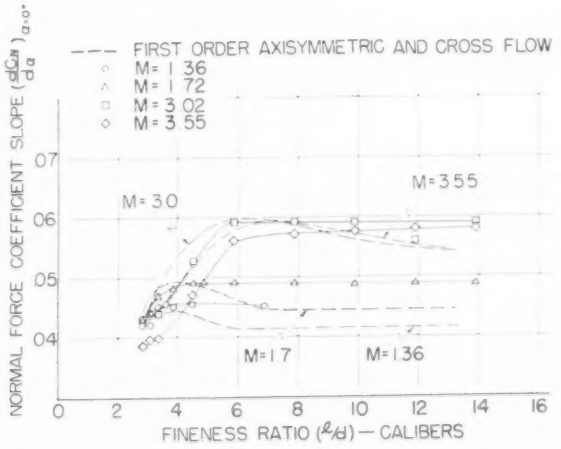

FIG. 13. Theoretical and experimental values of normal force coefficient slope variation with fineness ratio for ogive nose body.

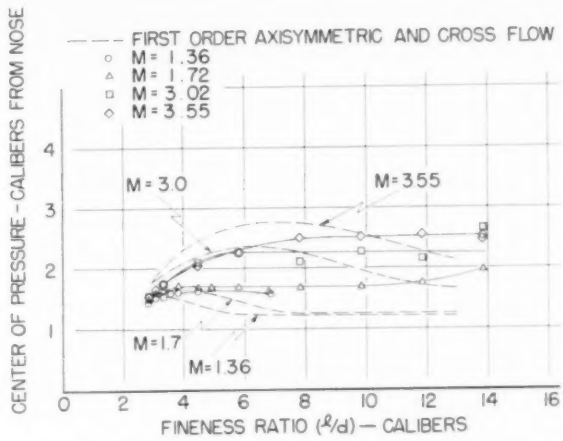

FIG. 14. Theoretical and experimental values of variation of center of pressure location with fineness ratio for ogive nose body.

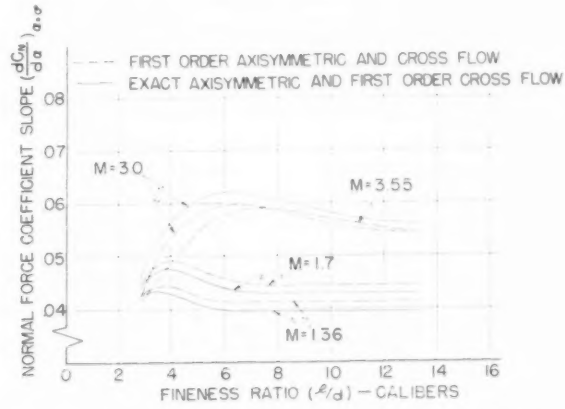
NORMAL FORCE COEFFICIENT SLOPE (dCN/dα)α→0
FIRST ORDER AXISYMMETRIC AND CROSS FLOW
EXACT AXISYMMETRIC AND FIRST ORDER CROSS FLOW
M = 3.0
M = 3.55
M = 1.7
M = 1.36
FINENESS RATIO (ℓ/d) — CALIBERS

FIG. 15. Theoretical values of normal force coefficient slope variation with fineness ratio for ogive nose body.

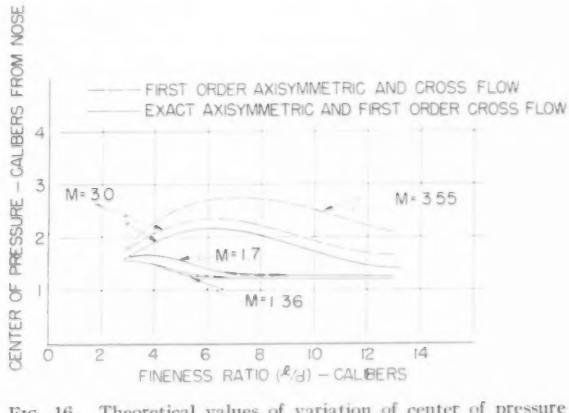
FIRST ORDER AXISYMMETRIC AND CROSS FLOW
EXACT AXISYMMETRIC AND FIRST ORDER CROSS FLOW
M = 3.0
M = 3.55
M = 1.7
M = 1.36
CENTER OF PRESSURE - CALIBERS FROM NOSE
FINENESS RATIO (ℓ/d) — CALIBERS

FIG. 16. Theoretical values of variation of center of pressure location with fineness ratio for ogive nose body.

(c) Evaluation of Improved First-Order Theory

Evaluation of the improved first-order solution may be made from Figs. 13 and 14. In the case of the normal force coefficient slope, $dc_N/d\alpha$, the values from the improved first-order solution agree within about 10 per cent of the experimental data. Both the observed increase in $dc_N/d\alpha$ with increased length and the maximum value at some particular length are predicted. However, at all Mach Numbers, the theory predicts a decrease in $dc_N/d\alpha$ when the fineness ratio is increased sufficiently. It is conceivable that the theory is closely representative of the potential flow, and that the constancy of the experimental results above a certain length may be attributed to viscous effects—i.e., boundary-layer displacement thickness. It is also noteworthy that, in the ogive nose case, the theory predicts the observed decrease in $dc_N/d\alpha$ at Mach Numbers greater than 3.

The predicted centers of pressure are not as good quantitatively as are the values of $dc_N/d\alpha$; however, the qualitative trends of the observed results are substantiated. Associated with the predicted decrease in $dc_N/d\alpha$ is the forward movement of the computed center of pressure above a certain length of afterbody.

(d) Evaluation of a Hybrid Theory

The improved first-order and the modified hybrid solutions may be compared in Figs. 15 and 16. It is apparent that the differences between the first-order and the hybrid solutions are of a minor nature. In fact, the first-order agreement with the present experiments is better than that of the hybrid solution, although this is probably fortuitous. The predicted trends are much the same, and it appears that the increased effort in using the hybrid solution is not warranted.

Conclusions

In the small-angle, potential-flow range, the normal force coefficient slope, $dc_N/d\alpha$, increases to some maximum essentially constant value as afterbody is added to a basic pointed nose. The magnitude of the increase and the afterbody length at which no further increase occurs are a function of Mach Number and nose shape.

The normal force coefficient slope increases with Mach Number until a maximum is reached. Further increases in Mach Number result in a decrease in $dc_N/d\alpha$.

The center of pressure moves rearward as afterbody is added until a maximum constant value is attained and also moves rearward as the Mach Number is increased.

The predictions of improved first-order theory are in fair quantitative agreement and good qualitative agreement with the experimental results.

It is indicated that a hybrid solution—exact axial flow, first-order cross flow—has little, if any, superiority in comparison with improved first-order theory.

References

[1] Van Dyke, Milton D., *First- and Second-Order Theory of Supersonic Flow Past Bodies of Revolution*, Journal of the Aeronautical Sciences, Vol. 18, No. 3, pp. 161-178, March, 1951.

[2] Buford, William E., and Shatunoff, Stanley, Ballistic Research Laboratories Confidential Memorandum Report No. 760, February, 1954.

Third U.S. National Congress of Applied Mechanics

Brown University, June 11–14, 1958

The congress program, which is to be distributed in May, will feature over 100 papers in Applied Mechanics, including mechanics of rigid bodies, mechanics of deformable solids, mechanics of fluids and gases, thermodynamics, and heat transfer. In addition, there will be four general lectures by leading authorities.

To reduce the cost of attending the symposium to the utmost, the following all-inclusive living arrangement is offered. This covers rooms in the new West Quadrangle of Brown University and all meals from Breakfast on Wednesday, June 11, through Luncheon on Saturday, June 14, but *not* the Banquet on Thursday night ($5.00). The rates will be $24.00 for each of two persons sharing a room, or $30.00 for a person occupying a single room. Rooms will be available without additional charge for Tuesday night and Saturday night.

Registration Fees: Advance Registration on or before June 7, $4.00. Registration on June 8 or later, $6.00. Please make checks payable to: *Applied Mechanics Congress*, not to any person.

Requests for copies of the program and letters concerning advance registration should be addressed to Miss E. M. Addison, Box F, Brown University, Providence 12, R.I. In registering, please indicate number of persons in party and family relationship, desire for single rooms or willingness to share rooms, estimated arrival and departure times, and need for parking space.

On the Numerical Calculation of Detached Bow Shock Waves in Hypersonic Flow†

P. R. GARABEDIAN* AND H. M. LIEBERSTEIN**
Stanford University and the Ramo-Wooldridge Corporation

SUMMARY

A method is described for calculating examples of hypersonic flow with a detached bow shock wave past a bluff axially symmetric body. The form of the shock wave is assumed, and the analysis is based on a Cauchy problem for the stream function in the subsonic region, where the motion is governed by a partial differential equation of elliptic type. Through analytic continuation into the complex domain, the Cauchy problem is reformulated in such a manner that it becomes properly set in the subsonic region. This leads to a stable scheme for computation of the flow by finite differences. Numerical examples at free-stream Mach Number 5.8 are presented in which the flow is determined throughout the subsonic region, and, in particular, the detachment distance, the location of the sonic line, and the pressure distribution along the body are calculated. These results are in excellent agreement with experimental data obtained at the California Institute of Technology.

SYMBOLS

r, z	= cylindrical coordinates
u, v	= r, z components of velocity
ψ	= stream function
p	= pressure
ρ	= density
M	= free-stream Mach Number
q_1	= speed in front of shock
q	= speed behind shock
γ_1	= ratio of specific heats in front of shock
γ	= effective ratio of specific heats behind shock
H	= enthalpy
S	= entropy
μ	= speed of sound
k	= an energy loss across shock
A	= function of ψ equal to p/ρ^γ
T	= temperature
H_0	= stagnation enthalpy
f, g	= functions of r^2 describing shock
l, z_0	= parameters in equation of shock
a, b, c, d	= coefficients in partial differential equation for ψ
P, Q	= $\partial\psi/\partial r, \partial\psi/\partial z$
α, β	= characteristic coordinates
x, y	= coordinates related to α, β
ξ, η	= real and imaginary parts of y
F	= arbitrary function of y
E_1, E_2, E_3, E_4	= parameters in definition of F
$\Delta x, \Delta\eta$	= increments in x, η
s	= $\Delta x/\Delta\eta$, ratio of mesh sizes
σ^+, σ^-	= slopes of the characteristics
V, V_1, L, L_1, Λ	= auxiliary functions of ψ
B	= matrix of coefficients
R	= vector of unknown functions
N	= number of mesh points on initial line
h	= distance between body and shock along z-axis
κ	= curvature of body
K	= curvature of shock

Received July 8, 1957.

† Portions of this work were done under sponsorship of the Office of Naval Research.

* Professor of Mathematics, Stanford University, and Consultant, the Ramo-Wooldridge Corporation.

** Member of the Technical Staff, the Ramo-Wooldridge Corporation.

INTRODUCTION

IN THIS PAPER we analyze the steady supersonic flow of an inviscid compressible fluid past a blunt body of revolution. In such a flow, a detached bow shock wave appears in front of the body. We shall be interested in studying the properties of the flow in the region between this shock wave and the nose of the body, and, in particular, our attention will be focused on the behavior of the motion near the stagnation point located at the intersection of the nose with the axis of symmetry. Indeed, we shall confine our discussion to the subsonic region behind the vertex of the detached shock wave. Thus it suffices to visualize a model where the body extends smoothly to infinity behind the bow wave and where no wake or further shocks appear.

In recent years, a great deal of both theoretical and experimental work has been done on this problem (see references 1, 3, 5, 8, 9, 10, and 11). It has generally been assumed that most of the important properties of the bow shock wave are of a local character, and the above simplified model has proved to be quite successful as a point of departure. The most serious difficulties encountered in attempting to determine such flows theoretically result from the unfortunate fact that for a prescribed body the shape and location of the shock wave are not known in advance, whence it is actually a free boundary problem that must be solved.

In modern aerodynamics, the Mach Number M of the uniform flow in front of the bow wave must be allowed to take on values significantly higher than $M = 8$. In hypersonic flows of this type, there is an extremely sharp increase in temperature across a strong shock, and for a real gas it is necessary to take into account the effects of dissociation. One possibility here is to evaluate the equation of state of the gas by means of tables of the pressure p, enthalpy H, and entropy S as functions of the temperature T and density ρ which have now become available[4,6] for a wide range of values of T and ρ. However, in our analysis the situation simplifies considerably because we restrict our attention to the subsonic region near the stagnation point. Crude arguments show that in this region T and ρ vary by as little as a sixth of their total values,

so that only a very small section of the tables is actually relevant for the subsonic portion of a specific flow. Examination of such a section of the tables establishes that, over the small ranges of values of T and ρ that we have described, the quantity $H\rho/p$ deviates from an appropriate fixed value by less than 1 per cent. Thus we are justified in using in the subsonic region the empirical equation of state

$$H = [\gamma/(\gamma - 1)]\,(p/\rho) \tag{1}$$

where γ is a constant to be found from the tables and can be interpreted as an effective ratio of specific heats.

In practice, γ always exceeds 1, but must be chosen quite close to 1 when the temperature in the subsonic region is high. In front of the bow wave, of course, an actual ratio of specific heats γ_1 replaces the empirical value γ in the equation of state (1). It is also desirable to provide for the addition of a constant on the right in Eq. (1) in case this should result in a better representation for the enthalpy behind the shock wave. It can easily be shown from the principles of thermodynamics that this slightly more general form of the equation of state is equivalent to the assumption that the entropy S is a function of p/ρ^γ alone.

Determination of the shape of the bow wave in front of a prescribed body involves, as we have observed, the solution of a difficult free boundary problem. On the other hand, it is possible to find the body generating a given shock wave by solving an initial value problem for the equations of motion. Such an initial value problem is not properly set in the usual sense when we assign Cauchy data along the arc of the shock wave bordering the subsonic region in a meridian plane, since in this region the flow is described by a stream function which satisfies a partial differential equation of elliptic type. However, we shall show how this initial value problem can be reformulated in the complex domain in such a manner that it becomes properly set, and our reformulation will lead to a stable numerical scheme for calculation of the stream function in the subsonic region. This procedure enables one to obtain numerical examples of the flow with a detached shock past a blunt body of revolution.

Such examples yield much significant information about the physical properties of the flow. It is possible to deduce from them a theoretical graph of the product κh of the curvature κ of the body times the detachment distance h as a function of the free-stream Mach Number M. A description of the distributions of pressure and density along the body can also be found, and the position of the sonic line can be determined. It is reasonable to expect that all this data is to a certain extent insensitive to alterations in the shape of the body, and thus the reliable examples which our method gives will be of considerable practical value.

Cauchy Problem for the Stream Function

We shall work in a meridian plane with the usual coordinates r and z, where r is the radius and z the altitude of a cylindrical coordinate system in space. If we denote by u and v the components of velocity in the directions of increasing r and z, respectively, then the conservation of mass implies the existence of a stream function ψ such that

$$\psi_r = r\rho v, \quad \psi_z = -r\rho u \tag{2}$$

The conservation of energy can be expressed by means of either of the two relations

$$H(p, \rho) + (q^2/2) = H_0 \tag{3}$$

$$p = A(\psi)\rho^\gamma \tag{4}$$

where H is the function of p and ρ defined by Eq. (1), $q^2 = u^2 + v^2$ is the square of the speed, H_0 is a constant called the stagnation enthalpy, and A is an arbitrary function of ψ alone. The equations of conservation of momentum can be combined with Eq. (3) to give Eq. (4), and conversely, they can be combined with Eq. (4) to give Eq. (3). Using Eqs. (2), (3), and (4) to eliminate derivatives of u, v, p and ρ, we can derive from the momentum equations the second-order partial differential equation

$$[1 - (u^2/\mu^2)]\psi_{rr} - (2uv/\mu^2)\,\psi_{rz} + [1 - (v^2/\mu^2)]\psi_{zz} = \rho v - r^2\rho^2[(H + q^2)/\gamma]\,[A'(\psi)/A(\psi)] \tag{5}$$

for the stream function ψ, where $\mu^2 = \gamma A\rho^{\gamma-1}$ is the square of the speed of sound. The conditions (2), (3), (4), and (5) comprise our formulation of the equations governing the steady axially symmetric motion of a compressible fluid. Since Eqs. (2), (3), and (4) can in principle be solved for u, v, p, and ρ in terms of r, ψ, ψ_r, and ψ_z, this system reduces, in effect, to the single second-order quasi-linear equation (5) for ψ, which is, of course, of the elliptic type in a region of subsonic flow.

Without loss of generality, we can choose a scale such that $p = \rho = 1$ in front of the bow shock wave, and we denote by $q_1 = M\gamma_1^{1/2}$ the speed there. We write the equation of the bow wave in the form

$$(z + z_0)^2 = f(r^2) = z_0^2 + g(r^2) \tag{6}$$

in the meridian plane, with $g(0) = 0$. The shock conditions across this curve which express the laws of conservation of mass and momentum are the usual ones of classical fluid mechanics, but, because we want to take into account the effects of dissociation in our analysis, we must write the shock condition expressing conservation of energy in the generalized form

$$[\gamma/(\gamma - 1)]\,(p/\rho) + (q^2/2) = [\gamma/(\gamma - 1)] + (q_1^2/2) + k \tag{7}$$

where p, ρ, and q stand for values of the pressure, density and speed just behind the shock and where k is a constant which allows for the change in the formula for the equation of the state as we cross the shock. Thus k depends on γ_1 and on the additive constant which might be included in Eq. (1). In the simplest case where no additive constant is inserted in the empirical equation of state (1), we find for k the value

$$k = [\gamma_1/(\gamma_1 - 1)] - [\gamma/(\gamma - 1)] \tag{8}$$

The constant on the right in Eq. (7) is, of course, merely another expression for the stagnation enthalpy H_0.

Since the flow in front of the bow wave is uniform, and since the stream function ψ is continuous across the shock due to the conservation of mass, we find that

$$\psi = q_1(r^2/2) \tag{9}$$

on the curve (6). Straightforward calculations with the remaining shock conditions show that along Eq. (6)

$$\psi_z = [q_1 r^2 f'(r^2)/(z + z_0)L]\,[1 - (1/V)] \tag{10}$$

and that

$$A(\psi) = [(\gamma - 1)/(\gamma + 1)] \times [(L_1 - q_1^2\,VL - VL^2)/L^2]\,V^{\gamma-1} \tag{11}$$

where

$$L = 1 + [2\psi f'(2\psi/q_1)^2/q_1 f(2\psi/q_1)] \tag{12}$$

$$L_1 = \left(\left\{2k + [2\gamma/(\gamma - 1)]\right\}L + q_1^2\right)L \tag{13}$$

$$\Lambda = 1 - \gamma\,(L/q_1^2) \tag{14}$$

$$V = \frac{(\gamma - 1)\,(q_1^2 + 2kL) + 2\gamma L}{\gamma q_1^2 + \gamma L + q_1[q_1^2\Lambda^2 - 2(\gamma^2 - 1)kL]^{1/2}} \tag{15}$$

We note also that

$$\frac{A'(\psi)}{A(\psi)} = \frac{L'(\psi)}{V} \times \frac{(\gamma - 1)L_1V_1 - \gamma V_1 VL(q_1^2 + L) - q_1^2 V(1 - V)}{L_1 - VL(q_1^2 + L)} \tag{16}$$

where

$$V_1 = \frac{\gamma}{(\gamma + 1)q_1^2} \times \left\{1 + \frac{q_1\Lambda + (\gamma^2 - 1)q_1(k/\gamma)}{[q_1^2\Lambda^2 - 2(\gamma^2 - 1)kL]^{1/2}}\right\} \tag{17}$$

We can now rewrite the second-order partial differential equation (5) for ψ in the form

$$a\,\psi_{rr} + 2b\,\psi_{rz} + c\,\psi_{zz} + d = 0 \tag{18}$$

where the coefficients a, b, c, and d are known functions of r, ψ, ψ_r, and ψ_z which are defined explicitly by means of the relations (2), (3), (4), (11), and (16). When the curve (6) is given analytically, Eqs. (9), (10), and (18) constitute a Cauchy problem for the determination of the stream function ψ. With our choice of the bow wave in an appropriate class of analytic curves (6), we shall investigate this Cauchy problem in the subsonic region, where Eq. (18) is of elliptic type. In particular, we shall work through in detail the case

$$f(r^2) = (M^2 - 1)\,(l^2 + r^2), \qquad z_0^2 = l^2(M^2 - 1) \tag{19}$$

in which the shock is a hyperbola whose asymptotes are Mach lines of the approach flow.

Characteristic Coordinates

The two families of characteristics of Eq. (18) are defined by the quadratic ordinary differential equation

$$a\dot{z}^2 - 2b\dot{z}\dot{r} + c\dot{r}^2 = 0 \tag{20}$$

This equation can be factored to yield

$$(\dot{z} - \sigma^+\dot{r})\,(\dot{z} - \sigma^-\dot{r}) = 0 \tag{21}$$

and for the moment we shall not let it disturb us that the roots σ^+ and σ^- are complex numbers when $b^2 - ac < 0$. Each factor in Eq. (21) defines a family of characteristics of Eq. (18). We set

$$P = \psi_r, \quad Q = \psi_z \tag{22}$$

and we introduce new independent variables α and β, called characteristic coordinates, which are defined by the property that one of them is constant along each curve of one family of characteristics, while the other is constant along each characteristic of the remaining family.

In terms of the characteristic coordinates α and β, we can reduce the second-order equation (18) in a standard way[2, 7] to the system of six first-order partial differential equations

$$z_\alpha - \sigma^+ r_\alpha = 0, \quad z_\beta - \sigma^- r_\beta = 0 \tag{23}$$

$$d\,\sigma^+ r_\alpha + a\,\sigma^+ P_\alpha + c\,Q_\alpha = 0 \tag{24}$$

$$d\,\sigma^- r_\beta + a\,\sigma^- P_\beta + c\,Q_\beta = 0 \tag{25}$$

$$\psi_\alpha - Pr_\alpha - Qz_\alpha = 0 \tag{26}$$

$$\psi_\beta - Pr_\beta - Qz_\beta = 0 \tag{27}$$

for the determination of the five unknown functions r, z, P, Q, and ψ. We do not need to use both of Eqs. (26) and (27), and, indeed, it suffices to take any fixed linear combination of them, although such a combination introduces in general a new artificial family of characteristics in the (α, β) plane. Together with the initial conditions

$$z = g(r^2)/[f(r^2)^{1/2} + z_0], \quad \psi = q_1 r^2/2 \tag{28}$$

$$Q = [q_1 r^2 f'(r^2)/(z + z_0)L]\,[1 - (1/V)] \tag{29}$$

$$P = q_1 r - [rf'(r^2)Q/(z + z_0)] \tag{30}$$

the first-order system (23), (24), (25), (26) is equivalent to the Cauchy problem defined by Eqs. (9), (10), and (18). Since further transformation of the characteristic coordinates is still permissible, we can impose the initial conditions along an arbitrary monotonic curve in the (α, β) plane and prescribe r arbitrarily along this curve.

It turns out to be convenient to make the additional substitution of variables

$$x = (\alpha + \beta)/2, \quad y = (\alpha - \beta)/2i \tag{31}$$

Eqs. (23), (24), and (25), together with the sum of Eqs. (26) and (27), transform into the system

$$r_x = [b\,r_y - a\,z_y]/(ac - b^2)^{1/2} \tag{32}$$

$$z_x = [c\,r_y - b\,z_y]/(ac - b^2)^{1/2} \tag{33}$$

$$P_x = [d\,z_y + b\,P_y + c\,Q_y]/(ac - b^2)^{1/2} \tag{34}$$

$$Q_x = [-d\,r_y - a\,P_y - b\,Q_y]/(ac - b^2)^{1/2} \tag{35}$$

$$\psi_x = [(Pb + Qc)r_y - (Pa + Qb)z_y]/(ac - b^2)^{1/2} \tag{36}$$

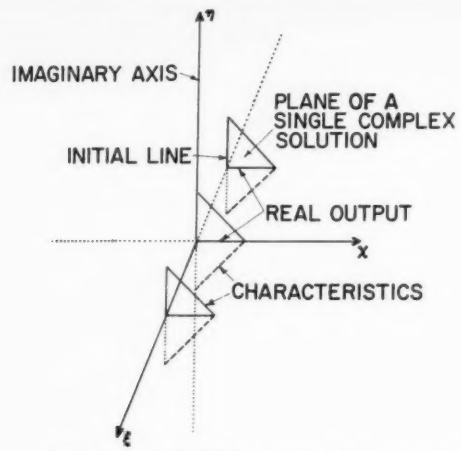

FIG. 1. Geometry of characteristic coordinates in the complex domain.

in the (x, y) plane. This canonical system, together with the initial conditions (28), (29), and (30), is also equivalent to the Cauchy problem (9), (10), (18), and it has the advantage that its real solutions generate real flows in the subsonic region, where $b^2 - ac < 0$, since no complex quantities appear in that case. For the sake of simplicity, we rewrite Eqs. (32), (33), (34), (35), and (36) in the matrix notation

$$R_x = B\,R_y \tag{37}$$

where R stands for the column vector of unknown functions r, z, P, Q, ψ and B is the appropriate five-by-five matrix of coefficients.

We are free to choose the y axis as our initial curve in the (x, y) plane, and we impose there the conditions (28), (29), and (30). To these we can add a relation $r = F(y)$, where F is an arbitrary real analytic function of y. This freedom results from the easily verified fact that our formulation of the Cauchy problem is invariant under any conformal transformation in the (x, y) plane. For the applications, it is convenient to use an explicit initial relation between r and y of the form

$$r = F(y) = E_1 y + E_2 y^3 + [E_3 y/(y^2 + E_4)] \tag{38}$$

where E_1, E_2, E_3, and E_4 are arbitrary real parameters.

Use of Complex Variables

In our reduction of Eq. (18) to the canonical form (37) we have not allowed the appearance of complex quantities to disturb us. This is justified when we take into account the analyticity of the functions which occur and when we think of the intermediate equations in our derivation as identities which must hold in the complex domain, according to the basic principles of analytic continuation. Thus we should assume from the beginning that we have continued all functions analytically into the complex domain so that they have become complex functions of complex variables. It is then irrelevant whether or not complex numbers are used in our calculations. It is convenient to observe at the conclusion of the argument, however, that, when $b^2 - ac < 0$, real solutions of the canonical system (37) in the real (x, y) plane correspond to real subsonic flows satisfying Eq. (18) in the physical plane.

We shall now make a more decisive use of complex variables by showing how the Cauchy problem for Eq. (18) can be formulated in the complex domain as a properly set initial value problem for the canonical system (37). For this purpose we keep x real, but we let $y = \xi + i\eta$ be complex. Thus we can visualize the domain of the independent variables in a space of three dimensions with the rectangular coordinates x, ξ, and η. The initial conditions (28), (29), (30), and (38) are imposed for $x = 0$, and they become identities in the complex variable y over the (ξ, η) plane. In particular, they are valid for variable η with $x = 0$ and ξ fixed. With this in mind, we shall restrict our attention to a plane $\xi =$ const., in which x and η are the rectangular coordinates.

Because of the Cauchy-Riemann equations, we can write Eq. (37) in the form

$$R_x = (B/i)R_\eta \tag{39}$$

in such a plane. The matrix B/i is easily seen to have the characteristic roots 1, -1 and 0, and the system (39) is of hyperbolic type in the (x, η) plane and has the three families of characteristic curves $x + \eta =$ const., $x - \eta =$ const., and $\eta =$ const. The last family appears because we used the sum of Eqs. (26) and (27) in our derivation of Eq. (37), whereas the earlier two families correspond to the original characteristics of the second-order partial differential equation (18). In this connection, it is interesting to note that Eq. (31) reduces, at least in the special case $\xi = 0$, to the rotation and magnification

$$x = (\alpha + \beta)/2, \quad \eta = (\beta - \alpha)/2 \tag{40}$$

and is therefore a real substitution in the (x, η) plane. Thus our introduction of η, rather than y, as the basic variable is equivalent to using real characteristic coordinates. (See Fig. 1.)

What we have established at this stage is that, by analytic continuation into the complex domain and appropriate choice of the independent variables, we can transform the real elliptic equation (18) into the hyperbolic system (39) for the determination of five complex-valued unknowns. Furthermore, we have shown that when $\eta = 0$, that is, in the (x, ξ) plane, the solution of Eq. (39) will be real. Of course, for $\eta \neq 0$ the unknowns r, z, P, Q, and ψ will in general turn out to be complex because of the appearance of i in Eq. (39) and because of the complex values of $y = \xi + i\eta$ which we substitute initially into Eq. (38).

In order to find an actual subsonic flow in the physical plane, we must solve the initial value problem for Eq. (39) for choices of the parameter ξ covering a complete interval. Thus with our method we must determine the solution in a three-dimensional region, although only the portion of this region which intersects the plane $\eta = 0$ yields physically significant data. However, at each specific stage of the procedure, we have

merely to deal with an initial value problem in two independent variables. The solution of each individual problem of this type yields values of ψ, P, and Q along a curve in the (r, z) plane. This curve assumes a shape which depends on our choice of the arbitrary function F in Eq. (38) and which can be prescribed quite generally.

The Cauchy problem for Eq. (39) is properly set in the sense that the solution depends continuously on the initial data, but the same is not true for Eq. (18) in the elliptic case $b^2 - ac < 0$. The explanation for this phenomenon is that a small change in the initial data for Eq. (18) in the real domain can result in a large change in the initial data for Eq. (39), since we obtain the latter by analytic continuation of the former into the complex domain. Thus we should treat the Cauchy problem for Eq. (18) only when the data can be continued into a sufficiently large section of the complex domain. The problem becomes properly set if we adopt a new criterion for continuity in the variation of the data which states that two sets of data are close only when the analytic continuation of their difference is small in the complex domain. Hadamard's classic counterexample does not satisfy this criterion.

An even more precise analysis of the situation can be made if we are content with a discussion of what happens in the space of the rotated characteristic coordinates x, ξ, and η. Here singularities are observed to travel along the characteristics $x + \eta = \text{const.}$ and $x - \eta = \text{const.}$ Hence a singularity of the initial data at the point with coordinates $\xi = \xi_0$, $\eta = \eta_0$ in the plane $x = 0$ will appear in the real (x, ξ) plane as a singularity of the solution at the two points whose coordinates are $x = \eta_0$, $\xi = \xi_0$, and $x = -\eta_0$, $\xi = \xi_0$. Thus singularities of the initial data which occur for relatively small values of η should be avoided. Also, if we wish to alter slightly Eq. (6) of the given bow shock wave so as to approximate more accurately the flow past a prescribed obstacle, we should only make changes which remain small after analytic continuation into the portion of the (ξ, η) plane that projects along the characteristics onto the region of the (x, ξ) plane corresponding to actual flow.

We can now justify more rigorously our choice of the hyperbola (19) as an appropriate shape to take for the bow wave. In the case of the hyperbola, indeed, the only singularity whose existence is predicted by our method would occur at the focus if Eq. (18) were to have the same fixed complex characteristics as Laplace's equation, since the characteristics through the focus would then be tangent to the initial curve in the complex domain. As matters stand, the singularity should occur not too far from the focus, whereas we can expect to obtain a flow past a smoothly rounded obstacle which lies much closer than this to the hyperbola.

Our analysis indicates that quantities of physical significance such as the detachment distance h between the body and the shock wave depend on properties of the flow over the whole subsonic region. Thus we could not hope to obtain a reliable description of, for example, the dependence of h on the free-stream Mach Number M by a method which, unlike ours, did not use Cauchy data along the complete arc of the bow wave bordering the subsonic portion of the flow. Our technique based on the canonical system (37) determines the flow throughout the subsonic region, but not beyond, since the denominator in Eqs. (32), (33), (34), (35), and (36) vanishes on the sonic line. The location of the sonic line itself, however, can be found by using Eq. (37). In the supersonic region beyond the sonic line, the classical procedures for treatment of the initial value problem for a hyperbolic equation apply, and therefore we shall not concern ourselves in this paper with the apparently more routine difficulties which present themselves there.

Finite Difference Scheme

We are interested in giving a numerical solution of the initial value problem defined by Eqs. (28), (29), (30), (38), and (39). We shall outline briefly a finite difference procedure which is well suited for this purpose.

We denote by Δx and $\Delta\eta$ positive increments in the variables x and η, and for a given fixed value of ξ we set

$$\left.\begin{aligned} R_{m,\,n} &= R[(m\Delta x/2),\ (n\Delta\eta/2)] \\ B_{m,\,n} &= B[(m\Delta x/2),\ (n\Delta\eta/2)] \end{aligned}\right\} \tag{41}$$

where $R(x, \eta)$ and $B(x, \eta)$ stand for the vector and matrix appearing in Eq. (39), thought of now as functions of x and η. For our numerical analysis, we approximate the partial differential equation (39) by the difference equation

$$R_{m+1,\,n} = R_{m-1,\,n} + s \times [(B_{m,\,n+1} + B_{m,\,n-1})/2i]\,(R_{m,\,n+1} - R_{m,\,n-1}) \tag{42}$$

where $s = \Delta x/\Delta\eta$. Since the characteristic roots of the matrix B/i are 1, -1, and 0, the solution of the initial value problem for Eq. (42) is stable if and only if $s \leq 1$. Because central differences are used, the truncation error is of the order of magnitude of the square of the mesh size $\Delta\eta$.

In practice, it is only necessary to use values of m and n in Eq. (42) whose sum is even. Furthermore, since $R(x, 0)$ and $B(x, 0)$ have real elements, the Schwarz principle of reflection shows that

$$R_{m,\,-1} = \bar{R}_{m,\,1}, \quad B_{m,\,-1} = \bar{B}_{m,\,1} \tag{43}$$

where $\bar{R}_{m,\,1}$ and $\bar{B}_{m,\,1}$ denote the matrices whose elements are the complex conjugates of the elements of $R_{m,\,1}$ and $B_{m,\,1}$. This symmetry property permits us to solve the initial value problem for Eq. (42) using only mesh points with $n \geq 0$, since when $n \geq 1$ we do not need any mesh points in the lower half-plane in order to evaluate Eq. (42), while for $n = 0$ the mesh points in the lower half-plane can be eliminated from Eq. (42) by means of Eq. (43). Thus our numerical scheme will consist first in calculating $R_{0,\,n}$ for $n = 0, 2, 4, \ldots, 2N - 2$ from the initial conditions (28), (29), (30), and (38), then in calculating $R_{1,\,n}$ for $n = 1, 3, 5, \ldots, 2N - 3$ by means of Eq. (42) with $R_{-1,\,n}$ replaced by $(R_{0,\,n+1} + R_{0,\,n-1})/2$ and s replaced by $s/2$, and

finally in calculating through repeated application of Eq. (42) the remaining values of $R_{m,n}$ such that $m + n$ is even and does not exceed $2N - 2$. (See Fig. 2.)

The method which we have now presented for the determination of hypersonic flows with a detached shock past bluff bodies of revolution is based entirely on the sound principles of exact theory. It can hardly be considered to be elementary, however, since we have been obliged to introduce complex quantities in a physically irrelevant space of three dimensions. We proceed to demonstrate that the approach is nevertheless quite practical by giving explicit numerical examples computed in all detail on a high-speed electronic calculator.

Discussion of Numerical Computations*

The procedure we have outlined in the previous sections has been programed for the ERA 1103 electronic calculator at the Ramo-Wooldridge Corporation. The program is designed so that the physically significant parameters M, γ, and γ_1 can be varied freely as well as the geometrical parameters l, ξ, E_1, E_2, E_3, E_4 and the mesh size $\Delta\eta$. For a specific choice of these parameters, a typical run with the number N of grid points on the initial line equal to 36 takes less than one hour of machine time.

Alterations in l merely produce a change of scale in the physical plane, while through variation of ξ we can sweep out curves of data there which cover a complete region. The influence of the parameters E_1, E_2, E_3, and E_4 on the calculations is more subtle, and we shall subject it to a detailed analysis.

Let us suppose that we have carried out the computations for a series of values of ξ, with $E_2 = E_3 = 0$, $E_1 = E_4 = 1$, and with the remaining parameters held fixed. We are interested in estimating the changes which can be effected by introducing new values of E_1, E_2, E_3, and E_4 in Eq. (38). The original computations establish a relationship between points in the real (x, y) plane and points in the physical plane. Now an alteration in the form of the function F inserted in the initial condition (38) can be interpreted as the result of performing the conformal mapping $Y - iX = F(y - ix)$ in the (x, y) plane, since our derivation of the canonical system (32), (33), (34), (35), (36) is invariant under such conformal transformations. It follows that we should be able to determine the correspondence between points in the transformed (x, y) plane and points in the physical plane directly, without additional use of the system of partial differential equations. Indeed, if the point (X, Y) is the image of the point (x, y) under the conformal mapping $Y - iX = F(y - ix)$, and if the original solution of Eq. (39) with $E_1 = E_4 = 1$, $E_2 = E_3 = 0$ gave at (X, Y) the pair of coordinates (r, z) in the physical plane, then the solution with the new initial data $r = F(y)$ should yield these same coordinates (r, z) precisely at (x, y).

Since different choices of F correspond to different choices of a conformal transformation in the plane of the canonical coordinates (x, y), it is evident that for a given value of ξ we should be able to obtain a variety of curves of data in the physical plane by appropriate selection of the parameters E_1, E_2, E_3, and E_4. The solutions of Eq. (39) which we arrive at in this manner generate widely differing two-dimensional surfaces in the four-dimensional complex extension of the (r, z) plane. In the numerical applications of our method, we require an F such that the curves of data which sweep out the physical plane as ξ varies will not only cover the body behind our prescribed shock wave, but will also reach the sonic line. To achieve this objective, we have taken

$$F(y) = (Ey + y^3/9)/(E + y^2) \tag{44}$$

corresponding to Eq. (38) with $E_1 = 1/9$, $E_2 = 0$, $E_3 = 8E/9$, and $E_4 = E$. When F is given by Eq. (44), the images of the lines $y = \text{const.}$ under the conformal transformation $Y - iX = F(y - ix)$ are curves winding around a double critical point in the (X, Y) plane at $X = 0$, $Y = (E/3)^{1/2}$. We choose E so that this critical point maps into the sonic point on the shock wave in the physical plane, whence our curves of data bend around to meet the sonic line.

The expression

$$F(y) = Ey/(E + y^2) \tag{45}$$

yields another useful choice for F which results from Eq. (38) when we set $E_1 = E_2 = 0$, $E_3 = E_4 = E$. Since in this case the critical point in the (X, Y) plane, which occurs at $X = 0$, $Y = E^{1/2}/2$, is simple, data curves are obtained which bend less sharply than those generated by Eq. (44).

So far our discussion of selecting parameters has been confined to the problem of obtaining adequate data behind a fixed shock wave. We shall consider next a more general shock curve than Eq. (19), which is defined by

$$f(r^2) = l_2(l_1 + l_3 r^2), \quad z_0^2 = l_1 l_2 \tag{46}$$

This equation describes a conic section which can be either an ellipse or a hyperbola. We note that in the case of the ellipse, however, the formulas in this paper yield velocities which must be reversed in order to generate a properly oriented flow. We wish to establish here a qualitative analysis of the dependence of the shape of the body behind the shock (46) on the parameters l_1, l_2, and l_3.

Our conclusions in this direction are based on the remark that singularities of the flow can be expected to occur near the foci of the shock curve. Indeed, we have seen that if the stream function were to satisfy Laplace's equation instead of Eq. (18), a characteristic passing through a focus of Eq. (46) would be tangent to this initial curve in the complex domain. Thus, even in the case of Eq. (18), we anticipate that the stream function will be multiple-valued in the neighborhood of

* The authors wish to acknowledge their gratitude to Robert Beach, Kenneth Curewitz, Lynn Stoller, and Clyde Coller for their assistance in the preparation of this program.

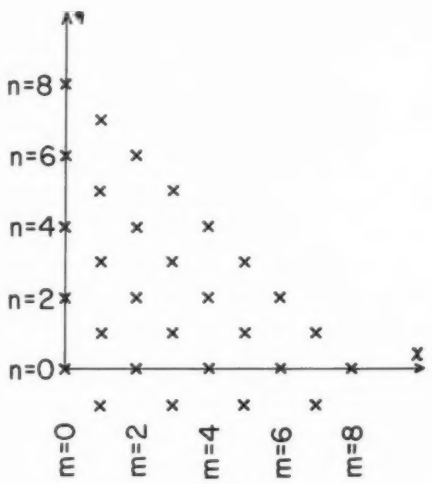

FIG. 2. Mesh points for the finite difference scheme.

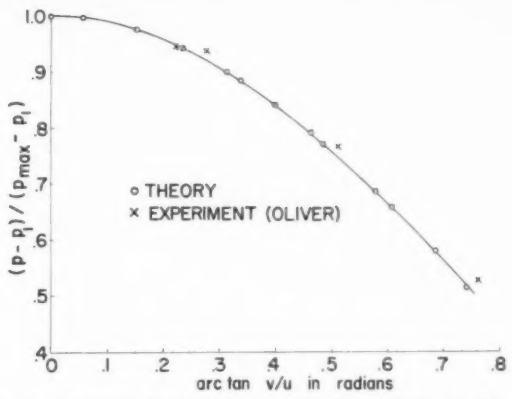

FIG. 4. Pressure distribution for the flow shown in Fig. 3.

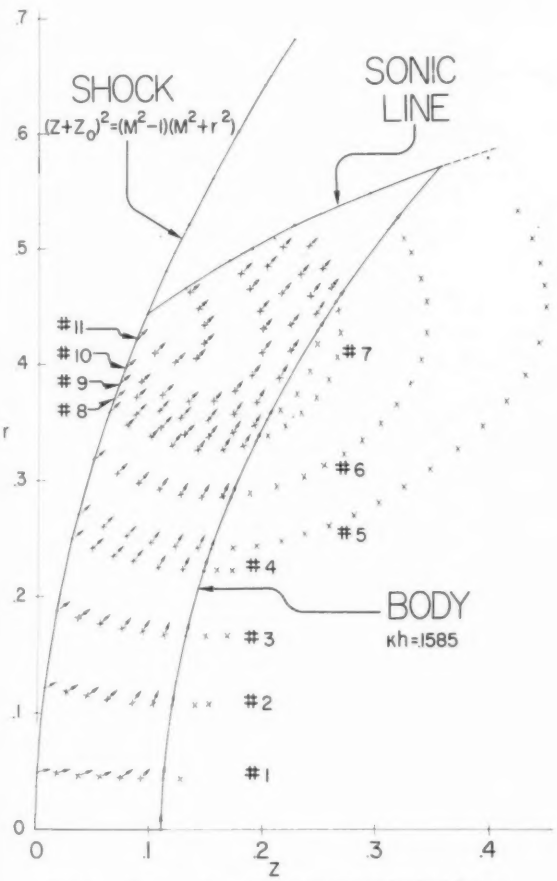

FIG. 3. Flow past an approximately spherical body.

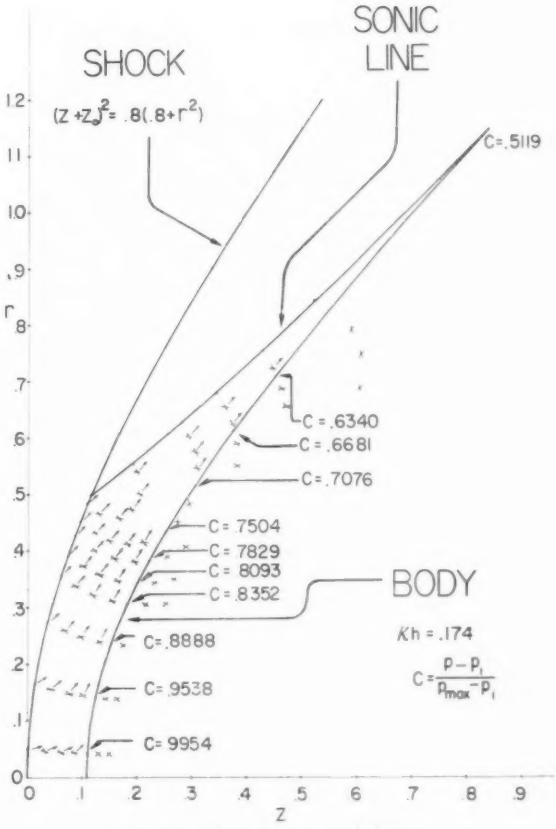

FIG. 5. Flow past a rounded cone.

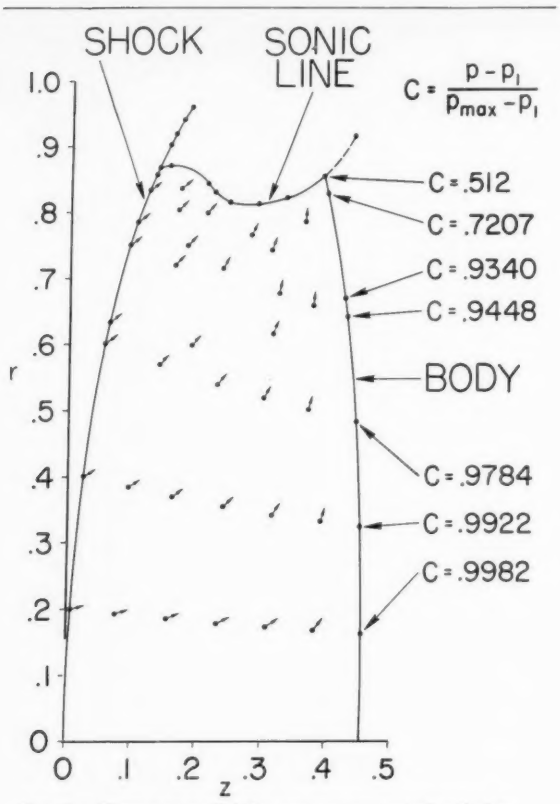

FIG. 6. Flow past a slightly concave truncated cylinder.

the focus and will have a branch point near by. A branch point is exactly the type of singularity exhibited by flow at a corner. Hence we should be able to achieve corners on the body behind the shock wave (46) by placing the foci of this conic section in the positions where we desire that the corners should appear. Thus to obtain flow past a rounded cone we should choose l_1, l_2, and l_3 so that Eq. (46) is a hyperbola with its focus just behind the stagnation point, whereas to obtain flow past a flat-nosed body of revolution we should take Eq. (46) to be an ellipse whose foci are located off the axis of symmetry near the points where the shoulder intersects the meridian plane. It is hoped that these comments might be helpful to investigators who wish to select curved shocks designed to generate a prescribed family of body shapes.

In this paper we present numerical examples which serve to establish the success of our method in practice. We have made our sample runs at free-stream Mach Number 5.8 with a ratio of specific heats $\gamma = \gamma_1 = 1.4$ in order to facilitate comparison with experimental data obtained in the hypersonic wind tunnel at the California Institute of Technology. The correlation between the theoretical and the experimental determinations of detachment distance and pressure distribution along the body is excellent, as is evident from a check of our tables and graphs against the results given by Oliver.[9, 10]

Our principal calculation has been made for the hyperbolic shock (19) with $l = M = 5.8$, $E_1 = 1/9$, $E_2 = 0$, $E_3 = 0.5163$, $E_4 = 0.5808$, and we have attempted to tabulate here enough of our data for this case to give the reader an accurate description of the information obtained. In the actual computations, complex floating-decimal arithmetic retaining eight digits was used. However, in our Tables we have rounded off the results so that only as many figures are listed as have been shown to be significant by truncation error tests based on variation of the mesh size. Roughly speaking, we had to take $N = 32$ grid points on the initial line in order to ensure getting four significant figures in the data along the body. This convergence deteriorates as we approach the sonic line because of the smallness there of the denominator $(ac - b^2)^{1/2}$ in Eqs. (32), (33), (34), (35), and (36). Thus our results along the sonic line have an accuracy of only two or three significant digits.

In Fig. 3 we present a detailed diagram of the flow just referred to. In this Figure the positions of the body and of the sonic line are shown, and velocity directions are indicated at sequences of points where runs of our program have punched out the flow data. The loci described by these points have nothing, of course, to do with physical properties of the flow, but depend rather upon the geometry associated with our method. We also include a graph of the pressure distribution along the body (see Fig. 4) and insert for purposes of comparison the corresponding experimental values due to Oliver[9, 10] for pressures on a sphere. The agreement is good when we take into account the differences in body shape between his work and ours.

Figs. 5 and 6 show two further diagrams of flows computed using a more general shock curve of the type (46). Fig. 5 corresponds to the values $l_1 = l_2 = 0.8$, $l_3 = 1$, $M = 5.8$, $\gamma = \gamma_1 = 1.4$ of our principal parameters and depicts flow in front of a rounded cone. Here all runs were made with $E_1 = E_2 = 0$, $E_3 = E_4 = 0.9746$, except for one with $E_1 = E_2 = 0$, $E_3 = E_4 = 1.456$. Fig. 6 was obtained with $l_1 = 1.095$, $l_2 = 0.0865$, $l_3 = -1$, $M = 5.8$, $\gamma = \gamma_1 = 1.4$, and, for the most part, with $E_1 = E_4 = 1$, $E_2 = E_3 = 0$. It represents a flow past a body with a quite flat nose. Our purpose is to demonstrate with these Figures how readily our analytical technique permits us to calculate hypersonic flows with a detached shock past a variety of bodies of the kind in common use. Values for the pressure distributions along these bodies have been presented directly on the diagrams in order to make possible a comparison with experimental data. Again, our results agree quite well with those compiled at the California Institute of Technology hypersonic wind tunnel.

EXPLANATION OF THE TABLES

In Tables 1, 2, and 3 we list data for the flow we have calculated with $M = 5.8$, $\gamma = \gamma_1 = 1.4$, $k = 0$, $s = 1$, $l = 5.8$, $E_1 = 1/9$, $E_2 = 0$, $E_3 = 0.5163$, $E_4 = 0.5808$. Since we have normalized so that the pressure p_1 and density ρ_1 in front of the shock are both unity, the values of p and ρ that we present are actually to be

TABLE 1

n	r	z	φ	u	v	p	ρ	M^2
			run no. 1, ξ = .05, $\Delta\eta$ = .002639					
0	.04981	.00122	.00851	.2716	1.3275	38.986	5.2220	.17566
10	.04829	.01797	.00687	.2643	1.1145	40.333	5.3488	.12427
28	.04704	.03465	.00542	.2585	.9121	41.414	5.4495	.08447
42	.04601	.05124	.00412	.2543	.7175	42.259	5.5275	.05413
56	.04519	.06772	.00294	.2517	.5282	42.888	5.5850	.03185
70	.04455	.08409	.00184	.2509	.3423	43.315	5.6237	.01670
84	.04408	.10035	.00079	.2520	.1575	43.547	5.6442	.00818
98	.04376	.11651	-.00023	.2553	- .0281	43.584	5.6467	.00611
			run no. 2, ξ = .125, $\Delta\eta$ = .005312					
0	.12810	.00734	.05115	.6574	1.3953	38.521	5.2138	.23000
10	.11708	.03047	.03774	.6339	1.1037	40.226	5.3659	.15436
20	.11329	.05341	.02650	.6175	.8328	41.438	5.4708	.10137
30	.11050	.07615	.01671	.6085	.5754	42.230	5.5363	.06568
40	.10857	.09868	.00786	.6076	.3259	42.639	5.5664	.04433
50	.10742	.12104	-.00049	.6159	.0794	42.682	5.5627	.03590
			run no. 3, ξ = .2, $\Delta\eta$ = .005938					
0	.18656	.00751	.12200	.9947	1.5043	37.773	5.2004	.31983
10	.18041	.04156	.08848	.9578	1.2012	39.396	5.3303	.22811
20	.17445	.06533	.06103	.9327	.9250	40.478	5.4105	.16475
30	.17023	.08885	.03750	.9196	.6668	41.111	5.4498	.12217
40	.16748	.11218	.01640	.9194	.4205	41.341	5.4525	.09629
50	.16608	.13537	-.00346	.9336	.1814	41.185	5.4199	.08503
			run no. 4, ξ = .28, $\Delta\eta$ = .00625					
0	.25041	.03087	.21517	1.2867	1.6412	36.833	5.1829	.43714
10	.23992	.05361	.15814	1.2412	1.3535	38.219	5.2743	.33245
20	.23231	.07592	.11230	1.2096	1.0972	39.104	5.3224	.25929
30	.22698	.09793	.07356	1.1917	.8625	39.586	5.3358	.20836
40	.22356	.11975	.03933	1.1877	.6441	39.713	5.3183	.17462
50	.22186	.14146	.00770	1.1965	.4386	39.511	5.2715	.15521
60	.22176	.16314	-.02282	1.2254	.2439	38.989	5.1951	.14858
			run no. 5, ξ = .31, $\Delta\eta$ = .01575					
0	.27089	.03612	.25180	1.3779	1.6931	36.477	5.1760	.48300
4	.25984	.05798	.18712	1.3308	1.4159	37.761	5.2529	.37518
8	.25185	.07933	.13540	1.2977	1.1710	38.573	5.2902	.29932
12	.24623	.10037	.09188	1.2782	.9486	39.011	5.2960	.24568
16	.24261	.12121	.05365	1.2721	.7434	39.122	5.2740	.20905
20	.24078	.14194	.01863	1.2800	.5526	38.933	5.2256	.18635
24	.24061	.16263	-.01478	1.3027	.3744	38.457	5.1513	.17577
56	.29993	.33484	-.35887	2.1295	- .4182	25.463	3.6091	.47682
88	.50492	.43554	-.50012	2.1940	1.3562	20.090	2.9642	.70115
90	.52909	.42344	-.40292	2.1997	1.5876	20.383	3.0529	.78731
			run no. 6, ξ = .39, $\Delta\eta$ = .01106					
0	.31807	.04979	.34715	1.5764	1.8236	35.581	5.1583	.60169
6	.30583	.06974	.26359	1.5264	1.5688	36.639	5.2018	.48587
12	.29711	.08893	.19820	1.4910	1.3498	37.283	5.2143	.40410
18	.29105	.10771	.14401	1.4687	1.1553	37.611	5.2027	.34500
24	.28720	.12626	.09718	1.4586	.9805	37.672	5.1699	.30279
30	.28532	.14464	.05520	1.4607	.8228	37.494	5.1176	.27402
36	.28525	.16290	.01630	1.4748	.6814	37.095	5.0463	.25647
42	.28692	.18105	-.02086	1.5008	.5564	36.492	4.9569	.24858
70	.31720	.26393	-.19351	1.7570	.2398	31.592	4.3403	.30859
98	.38780	.33189	-.33741	2.0204	.5682	26.390	3.7175	.44323
120	.48226	.33433	-.19327	2.0846	1.3863	25.322	3.7060	.65520
124	.50633	.32239	-.07968	2.1162	1.6159	25.544	3.8039	.75412
126	.52045	.31326	.00559	2.1451	1.7578	25.676	3.8732	.82876
			run no. 7, ξ = .48, $\Delta\eta$ = .0105					
0	.35684	.06336	.44183	1.7343	1.9468	34.736	5.1408	.71858
10	.34153	.08908	.30724	1.6663	1.6244	35.859	5.1562	.55619
20	.33152	.11304	.21304	1.6273	1.3725	36.320	5.1295	.45718

TABLE 1 (continued)

n	r	z	φ	u	v	p	ρ	M^2
30	.32665	.13623	.13962	1.6121	1.1666	36.319	5.0708	.39491
40	.32610	.15886	.07872	1.6182	1.0008	35.940	4.9842	.35860
50	.32949	.18082	.02603	1.6434	.8750	35.248	4.8733	.34233
60	.33668	.20186	-.02044	1.6846	.7926	34.309	4.7435	.34230
80	.36234	.23915	-.09265	1.7965	.7784	32.042	4.4624	.38134
100	.40385	.26350	-.10658	1.9122	1.0010	29.966	4.2457	.47116
110	.43138	.26646	-.06292	1.9677	1.2135	29.312	4.2088	.54812
116	.45061	.26354	-.00584	2.0049	1.3794	29.076	4.2249	.61466
120	.46493	.25891	.05244	2.0342	1.5103	28.990	4.2576	.67320
124	.48102	.25132	.13577	2.0706	1.6645	28.990	4.3142	.75023
128	.50048	.23888	.26491	2.1224	1.8625	29.029	4.4057	.86440
			run no. 8, ξ = .51, $\Delta\eta$ = .01335					
0	.36980	.06728	.46924	1.7745	1.9813	34.499	5.1358	.75825
10	.34969	.09738	.30597	1.6963	1.6108	35.688	5.1378	.56270
20	.33994	.12501	.19898	1.6593	1.3387	36.010	5.0872	.45864
30	.33743	.15154	.11869	1.6550	1.1323	35.745	4.9968	.40151
40	.34114	.17687	.05462	1.6788	.9880	35.024	4.8740	.37727
50	.35070	.20043	.00309	1.7250	.9107	33.975	4.7290	.37830
60	.36602	.22115	-.03435	1.7859	.9091	32.754	4.5782	.40095
78	.40870	.24511	-.03604	1.9084	1.1269	30.718	4.3718	.49933
84	.42769	.24672	-.00024	1.9518	1.2709	30.239	4.3490	.55725
90	.44968	.24324	.07017	2.0010	1.4583	29.918	4.3662	.63906
96	.47615	.23221	.20128	2.0656	1.7076	29.774	4.4426	.76552
100	.49980	.21646	.36857	2.1391	1.9577	29.645	4.5421	.92021
			run no. 9, ξ = .55, $\Delta\eta$ = .01742					
0	.38259	.07201	.50227	1.8202	2.0223	34.218	5.1297	.79271
14	.35506	.11968	.25269	1.7144	1.4790	35.568	5.0843	.52342
26	.35201	.15608	.13508	1.7069	1.2048	35.213	4.9565	.43885
38	.36294	.18856	.05903	1.7545	1.0772	34.039	4.7791	.42510
50	.38704	.21348	.02668	1.8373	1.1178	32.516	4.6009	.46147
62	.42491	.22368	.07751	1.9404	1.3580	31.202	4.5045	.57840
74	.48362	.20187	.36791	2.1014	1.9011	30.504	4.6352	.87155
			run no. 10, ξ = .6, $\Delta\eta$ = .01848					
0	.39594	.07712	.53792	1.8665	2.0656	33.919	5.1232	.83625
14	.36930	.12188	.28550	1.7650	1.5588	35.120	5.0636	.57107
28	.36940	.15983	.16250	1.7660	1.3045	34.617	4.9177	.48945
42	.38951	.18896	.11378	1.8351	1.2742	33.287	4.7458	.50824
56	.42941	.19895	.18424	1.9512	1.5163	31.936	4.6583	.63681
66	.47661	.17918	.44463	2.0929	1.9609	31.247	4.7683	.89656
			run no. 11, ξ = .75, $\Delta\eta$ = .0164175					
0	.42202	.08760	.61113	1.9528	2.1526	33.323	5.1099	.92598
14	.40389	.11203	.43634	1.8861	1.8588	34.093	5.0687	.74467
28	.40110	.13094	.35434	1.8726	1.7126	34.112	5.0105	.67562
42	.40957	.14431	.33048	1.8978	1.6853	33.722	4.9535	.67590
56	.42915	.14787	.38878	1.9595	1.7992	33.122	4.9314	.75256
68	.46052	.13371	.58614	2.0672	2.1042	32.292	4.9795	.95635

TABLE 2
Data on Body for Fig. 3

	r	z	u	v	p	ρ	M
stag. pt.	0	.11149	0	0	43.778	5.665	0
run no. 1	.04382	.11285	.2543	.01424	43.59	5.648	.07749
run no. 2	.10747	.11972	.6151	.09406	42.69	5.564	.18987
run no. 3	.16623	.13128	.9300	.2233	41.24	5.428	.29324
run no. 4	.22169	.14690	1.2036	.3888	39.41	5.255	.39036
run no. 5	.24048	.15341	1.2905	.4523	38.70	5.188	.42317
run no. 6	.28577	.17080	1.4848	.6250	36.86	5.009	.50192
run no. 7	.33294	.19241	1.6641	.8245	34.76	4.8045	.58352
run no. 8	.35158	.20198	1.7288	.9080	33.89	4.7185	.61579
run no. 8	.42779	.24671	1.9520	1.2716	30.24	4.3490	.74671
run no. 7	.45222	.26312	2.0081	1.3938	29.06	4.2277	.78791
run no. 6	.51961	.31386	2.1430	1.7491	25.67	3.8689	.90761
sonic pt.	.568	.356	2.22	2.02	22.9	3.59	1

TABLE 3
Data on Sonic Line for Fig. 3

	r	z	ψ	u	v	p	ρ
shock pt.	.443	.0965	.673	2.02	2.22	32.8	5.10
run no. 11	.465	.130	.624	2.09	2.16	30.1	4.98
run no. 10	.488	.169	.549	2.14	2.10	30.9	4.81
run no. 9	.499	.190	.499	2.16	2.08	30.2	4.69
run no. 8	.508	.208	.450	2.18	2.07	29.5	4.58
run no. 7	.518	.226	.408	2.18	2.06	28.9	4.48
run no. 6	.545	.293	.200	2.22	2.04	25.8	4.03
body pt.	.568	.356	0	2.22	2.02	22.9	3.59
run no. 5	.569	.395	-.174	2.30	2.02	20.7	3.20

interpreted as values of p'/p_1 and ρ'/ρ_1. Similarly, the velocity components u and v as we list them are really values of the dimensionless ratios $(\rho_1/p_1)^{1/2}u$ and $(\rho_1/p_1)^{1/2}v$. Table 1 represents flow quantities on the shock, in the interior of the shock layer, and, when ψ is negative, inside the body. Excerpts from each run of the program corresponding to a specific choice of ξ and $\Delta\eta$ are listed under a single heading, and the runs are numbered consecutively in the order of increasing ξ. With each entry is included the value of the index m in our finite difference scheme for which it was computed. The data in Table 2 is evaluated for points on the body by interpolation, and the run from which each point was obtained is identified. Table 3 was derived by extrapolation in a similar manner and describes the flow at points along the sonic line, including one point inside the body.

Fig. 3 is a diagram of the flow described in more detail in the tables. Velocity directions at a selection of points in the interior of the flow are marked, and the product of the detachment distance h times the curvature κ at the vertex of the body is listed. In Fig. 4 we compare graphically plots of the pressure distribution as a function of the angle of inclination of the body for this flow and for Oliver's experimental work with a sphere.

Fig. 5 shows the flow in front of a rounded cone obtained by running our program with $M = 5.8$, $\gamma = \gamma_1 = 1.4$, $k = 0$, $s = 1$, $l_1 = l_2 = 0.8$, $l_3 = 1$, $E_1 = E_2 = 0$, and with $E_3 = E_4 = 0.9746$ or $E_3 = E_4 = 1.456$. The positions of the body and of the sonic line are shown, together with flow directions at interior points, and we have included in the diagram values for the pressure along the body. Fig. 6 is a similar diagram for flow past a flat-nosed body of revolution and was derived by setting $M = 5.8$, $\gamma = \gamma_1 = 1.4$, $k = 0$, $s = -1$, $l_1 = 1.095$, $l_2 = 0.0865$, $l_3 = -1$, and, primarily, $E_1 = E_4 = 1$, $E_2 = E_3 = 0$ in our basic program.

REFERENCES

[1] Cabannes, H., *Contribution a l'Etude Theorique des Fluides Compressibles: Ecoulements Transsoniques. Ondes de Choc.*, Ann. Sci. Ecole Norm. Sup., Vol. 69, pp. 1–63, 1952.

[2] Courant, R., and Hilbert, D., *Methoden der Mathematischen Physik*, Vol. 2, Chap. 5, Berlin, 1937.

[3] Garabedian, P. R., *Numerical Construction of Detached Shock Waves*, Technical Report No. 55, Stanford University, September, 1956.

[4] Gilmore, F. R., *Equilibrium Composition and Thermodynamic Properties of Air to 24,000°K.*, RM-1543, The Rand Corporation, August, 1955.

[5] Heberle, J. W., Wood, G. P., and Gooderum, P. B., *Data on Shape and Location of Detached Shock Waves on Cones and Spheres*, NACA TN 2000, 1950.

[6] Hilsenrath, J., and Beckett, C. W., *Tables of Thermodynamic Properties of Argon-Free Air to 15,000°K.*, Arnold Engineering Development Center TN-56-12, September, 1956.

[7] Lewy, H., *Neuer Beweis des analytischen Charakters der Loesungen elliptischer Differentialgleichungen*, Math. Ann., Vol 101, pp. 609–619, 1929.

[8] Lin, C. C., and Rubinov, S. I., *On the Flow Behind Curved Shocks*, J. Math. Phys., Vol. 27, pp. 105–129, 1948.

[9] Oliver, R. E., *An Experimental Investigation of Flow About Simple Blunt Bodies at a Nominal Mach Number of 5.8*, Journal of the Aeronautical Sciences, Readers' Forum, Vol. 23, No. 2, pp. 177–179, February, 1956.

[10] Oliver, R. E., *An Experimental Investigation of Flow Over Simple Blunt bodies at a Nominal Mach Number of 5.8*, Memorandum No. 26, Guggenheim Aeronautical Laboratory, California Institute of Technology, June, 1955.

[11] Schwartz, R. N., and Eckerman, J., *Shock Location in Front of a Sphere as a Measure of Real Gas Effects*, J. Appl. Phys., Vol. 27, No. 2, pp. 169–174, February, 1956.

[12] O'Bryant, W. T., and Machell, R. M., *An Experimental Investigation of Flow Over Blunt-Nosed Cones at a Mach Number of 5.8*, Journal of the Aeronautical Sciences, Vol. 23, No. 11, pp. 1054–1055, November, 1956. See also GALCIT Hypersonic Wind Tunnel Memorandum No. 32, June, 1956.

[13] Long, J. E., *Supersonic Drag Coefficients of Circular Cylinders up to Mach Number 8*, NAVORD Report 4382, October, 1956.

[14] Liepmann, H. W., and Roshko, A., *Elements of Gasdynamics*, John Wiley and Sons, Inc., New York, 1957.

Change of Address

Since the Post Office Department does not as a rule forward magazines to forwarding addresses, it is important that the Institute be notified of changes in address 30 days in advance of publishing date to ensure receipt of every issue of the JOURNAL and REVIEW.

Notices should be printed legibly and sent directly to:

Subscription Department
Institute of the Aeronautical Sciences, Inc.
2 East 64th Street, New York 21, N.Y.

Effect of Quasi-Steady Air Forces on Incompressible Bending-Torsion Flutter†

J. DUGUNDJI*

Massachusetts Institute of Technology

SUMMARY

Explicit solutions are obtained for the bending-torsion flutter of a two-dimensional airfoil in incompressible flow under the assumptions that the Theodorsen function, $C(k)$ is set equal to a real constant, and the diagonal virtual mass terms are negligible. For the case of small bending to torsion frequency ratio, ω_h/ω_α, a comparison is made of these quasi-steady solutions with an earlier empirical expression suggested by Theodorsen and Garrick for the nonsteady case, and the effect of the $C(k)$ function is indicated. The importance of the c.g. location for these small ω_h/ω_α cases is re-emphasized, and the possibility of flutter at zero air speed is indicated.

DISCUSSION

THE EFFECT of aerodynamic lags as expressed by the Theodorsen function $C(k)$ plays an important role in flutter of airfoils in incompressible flow.[1, 2] It might be of general interest to examine this effect and indicate its magnitude for certain specific cases.

First, the flutter of an airfoil using quasi-steady air forces is to be determined (see, for example, Chap. 6 of reference 3). It has already been shown that in the high supersonic case where a quasi-steady theory (piston theory) is valid, rather simple closed form solutions result for the two-dimensional bending-torsion case.[4] Following a suggestion of Prof. H. Ashley, the incompressible quasi-steady theories are examined in a similar fashion to observe their forms and trends.

The equations of motion for the bending-torsion flutter of a two-dimensional airfoil in incompressible flow can be written in the Laplace transform, nondimensional form,

$$\{[\mu+1]p^2+2C(p)p+\mu(\omega_h/\omega_\alpha)^2k_\alpha^2\}\bar{h}+\big(\mu\bar{x}_\alpha p^2+\{1+2[(1/2)-a]C(p)\}p+2C(p)\big)\bar{\alpha}=0 \quad (1)$$

$$\{\mu\bar{x}_\alpha p^2-2[(1/2)+a]C(p)p\}\bar{h}+\big([\mu r_\alpha^2+a^2+(1/8)]p^2+\{(1/2)-a-2[(1/4)-a^2]C(p)\}p+\{\mu r\alpha^2-2[a+(1/2)]C(p)\}\big)\bar{\alpha}=0 \quad (2)$$

where

p = transform variable of Laplace transform taken with respect to $s = Vt/b$

$\bar{h}$, $\bar{\alpha}$ = Laplace transformed of h and α

$C(p)$ = transformed Theodorsen function

k = $\omega b/V$ (reduced frequency)

k_α = $\omega_\alpha b/V$

μ = $m/\pi\rho b^2$ (density ratio)

$\bar{x}_\alpha$ = $x_\alpha - (a/\mu)$

and the remaining symbols are as conventionally described in the literature.[1, 2, 3]

In all the developments that follow the density ratio, μ will be assumed high enough (say $\mu > 15$) to permit neglecting the virtual mass contribution to the hh and $\alpha\alpha$ terms, that is,

$$[\mu+1]\approx\mu, \quad [\mu r_\alpha^2+a^2+(1/8)]\approx\mu r_\alpha^2$$

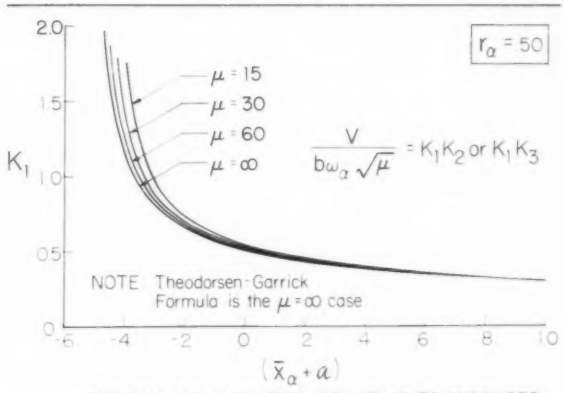

FIG. 1. Values of K_1.

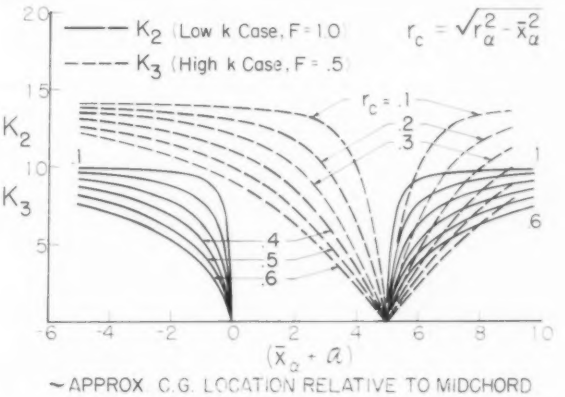

FIG. 2. Values of K_2 and K_3.

Received July 23, 1957.

† The author wishes to acknowledge helpful discussions with Drs. I. E. Garrick and H. Ashley in the preparation of this paper.

* Assistant Professor in Aeronautical Engineering.

One manner of evaluating the flutter frequency and speed is to first determine the characteristic equation of Eqs. (1) and (2), next assume harmonic motion ($p = ik$), then determine the values of k and k_α which make both the real and imaginary parts of the resulting equation equal to zero.

Low k Case

For the conventional quasi-steady case, one assumes $C(k) = 1$ which corresponds to the assumption that $k \to 0$. Expansion of the determinant and setting first the imaginary, then the real part equal to zero results in the following expressions for the flutter frequency and flutter speed:

$$\frac{\omega}{\omega_\alpha} = \Omega = \sqrt{\frac{r_\alpha^2 + (\omega_h/\omega_\alpha)^2[a - (1/2)]a}{r_\alpha^2 - \bar{x}_\alpha^2 + (\bar{x}_\alpha + a)^2 - (1/2)(\bar{x}_\alpha + a)}} \tag{3}$$

$$\frac{V}{b\omega_\alpha\sqrt{\mu}} = \sqrt{\frac{\Omega^2[r_\alpha^2 - \Omega^2(r_\alpha^2 - \bar{x}_\alpha^2)] - (\omega_h/\omega_\alpha)^2 r_\alpha^2(1 - \Omega^2)}{2\{\Omega^2[(1/2) + a + \bar{x}_\alpha - (1/\mu)] - (\omega_h/\omega_\alpha)^2[a + (1/2)]\}}} \tag{4}$$

For the important case where ω_h/ω_α is small ($\omega_h/\omega_\alpha \to 0$), the flutter speed reduces to

$$\frac{V}{b\omega_\alpha\sqrt{\mu}} = \sqrt{\frac{r_\alpha^2}{2[(1/2) + a + \bar{x}_\alpha - (1/\mu)]}}\sqrt{\frac{(\bar{x}_\alpha + a)^2 - (1/2)(\bar{x}_\alpha + a)}{r_\alpha^2 - \bar{x}_\alpha^2 + (\bar{x}_\alpha + a)^2 - (1/2)(\bar{x}_\alpha + a)}} \tag{5}$$

For the purpose of discussion, the first radical of Eq. (5) is designated K_1, and the second radical, K_2. It is to be noted that K_1 corresponds, for high μ, identically with an empirical formula suggested by Theodorsen and Garrick[2] in 1940. Theodorsen and Garrick's empirical formula was shown by comparison with calculations to be a reasonable approximation to the flutter speed including the $C(k)$ effect for the case of small ω_h/ω_α, for the range of $x_\alpha + a$ from -0.4 to 0.1, and for $\mu > 10$. The second radical, K_2, of Eq. (5) can therefore be looked upon as indicative of the effect of using quasi-steady rather than nonsteady air forces for the case where $\omega_h/\omega_\alpha \to 0$. Fig. 1 gives a plot of the radical K_1 versus the significant parameter, $\bar{x}_\alpha + a$, (roughly the c.g. location) for a typical value of $r_\alpha = 0.50$. Conversion to other values of r_α follows readily. In Fig. 2, the solid lines represent K_2 plotted versus $\bar{x}_\alpha + a$ for different values of $r_c = \sqrt{r_\alpha^2 - \bar{x}_\alpha^2}$ (roughly the nondimensional radius of gyration about the c.g.).

From Fig. 2, it appears that the use of quasi-steady air forces results in lower flutter speeds than when using nonsteady air forces, the discrepancy getting worse as the c.g. approaches the mid-chord and as r_c increases from zero. When $\bar{x}_\alpha + a = 0$, the quasi-steady flutter speed indeed drops to zero. For the range of $0 < \bar{x}_\alpha + a < 0.5$, it can be shown by examination of the coefficients of the characteristic equation of Eqs. (1) and (2) and its discriminant that the system is unstable for all air speeds greater than zero. For $\bar{x}_\alpha + a > 0.5$, the flutter speed increases again from zero. For values of $\bar{x}_\alpha + a$ below $-0.5 + (1/\mu)$, the flutter speed is infinite.

The reduced frequency, k, associated with these quasi-steady flutter speeds is readily obtained from Eqs. (5) and (3). This varies from $k = 0$ at $\bar{x}_\alpha + a = -0.5 + (1/\mu)$ to $k \to \infty$ at $\bar{x}_\alpha + a = 0$. It remains infinite for $0 < \bar{x}_\alpha + a < 0.5$ and then decreases again as the flutter speed increases for $\bar{x}_\alpha + a > 0.5$. It is interesting to note the great effect of the $C(k)$ function on flutter of airfoils whose c.g. location is near the mid-chord but the minor effect when the c.g. is near the quarter chord. Another interesting phenomenon, that of flutter at zero air speed and infinite k when the c.g. lies between the mid-chord and the three-quarter chord, is also to be noted. The introduction of some additional damping to the system would raise this zero flutter speed to some small finite value.

High k Case

The possibility of low-speed, high k flutter evidenced in the previous case leads naturally to another "quasi-steady" approximation—namely, setting $C(k) = 0.5$. This is the asymptotic value for $k \to \infty$ and corresponds to the low-speed flutter examined previously by Biot and Arnold.[5] Expansion of the determinant as before leads to

$$\frac{\omega}{\omega_\alpha} = \Omega = \sqrt{\frac{r_\alpha^2 + (\omega_h/\omega_\alpha)^2[a - (1/2)]^2}{r_\alpha^2 - \bar{x}_\alpha^2 + [\bar{x}_\alpha + a - (1/2)]^2}} \tag{6}$$

$$\frac{V}{b\omega_\alpha\sqrt{\mu}} = \sqrt{\frac{\Omega^2[r_\alpha^2 - \Omega^2(r_\alpha^2 - \bar{x}_\alpha^2)] - (\omega_h/\omega_\alpha)^2 r_\alpha^2(1 - \Omega^2)}{\Omega^2[(1/2) + a + \bar{x}_\alpha - (1/\mu)] - (\omega_h/\omega_\alpha)^2[a + (1/2)]}} \tag{7}$$

For small ω_h/ω_α, the flutter speed becomes

$$\frac{V}{b\omega_\alpha\sqrt{\mu}} = \sqrt{\frac{r_\alpha^2}{2[(1/2) + a + \bar{x}_\alpha - (1/\mu)]}}\sqrt{\frac{2[\bar{x}_\alpha + a - (1/2)]^2}{r_\alpha^2 - \bar{x}_\alpha^2 + [\bar{x}_\alpha + a - (1/2)]^2}} \tag{8}$$

The first radical in Eq. (8) is seen to be K_1, while the second radical is now designated K_3. As in the case of K_2, the quantity K_3 is a function only of $\bar{x}_\alpha + a$ and r_c and is shown plotted with the dashed lines in Fig. 2.

It can be seen that the zero air speed, infinite k flutter now only occurs when the c.g. lies at the three-quarter chord point. As the region near this point corresponds to high k where the approximation that $C(k) = 0.5$ is valid, the quasi-steady analysis gives an accurate picture of the nonsteady flutter speed in this region (the empirical Theodorsen-Garrick formula as expressed by K_1 was not intended to apply for $\bar{x}_\alpha + a$ much greater than 0.1). It is interesting to note that for this case of low ω_h/ω_α, the low-speed flutter of Biot and Arnold is independent of elastic axis position but depends rather on location of the c.g.

Other Quasi-Steady Cases

To account for actual lift-curve slopes, the factor $C(k)$ is sometimes replaced by some constant, F, generally smaller than unity. For these cases, the flutter frequencies and speeds become

$$\frac{\omega}{\omega_\alpha} = \Omega = \sqrt{\frac{r_\alpha^2 + (\omega_h/\omega_\alpha)^2[a - (1/2)]\{a - (1/2)[(1/F) - 1]\}}{r_\alpha^2 - \bar{x}_\alpha^2 + (\bar{x}_\alpha + a)^2 - (1/2F)(\bar{x}_\alpha + a) + (1/4)[(1/F) - 1]}} \tag{9}$$

$$\frac{V}{b\omega_\alpha\sqrt{\mu}} = \sqrt{\frac{\Omega^2[r_\alpha^2 - \Omega^2(r_\alpha^2 - \bar{x}_\alpha^2)] - (\omega_h/\omega_\alpha)^2 r_\alpha^2(1 - \Omega^2)}{2F\{\Omega^2[(1/2) + a + \bar{x}_\alpha - (1/\mu)] - (\omega_h/\omega_\alpha)^2[a + (1/2)]\}}} \tag{10}$$

and for small ω_h/ω_α,

$$\frac{V}{b\omega_\alpha\sqrt{\mu}} = \sqrt{\frac{r_\alpha^2}{2[(1/2) + a + \bar{x}_\alpha - (1/\mu)]}}\sqrt{\frac{(\bar{x}_\alpha + a)^2 - (1/2F)(\bar{x}_\alpha + a) + (1/4)[(1/F) - 1]}{F\{r_\alpha^2 - \bar{x}_\alpha^2 + (\bar{x}_\alpha + a)^2 - (1/2F)(\bar{x}_\alpha + a) + (1/4)[(1/F) - 1]\}}} \tag{11}$$

The values of the modifying constant in Eq. (11) corresponding to K_2 and K_3 have not been plotted on Fig. 2 for different values of F. However, it can be shown that they will lie somewhere in between the $F = 1$ and $F = 0.5$ cases considered previously. It is interesting to note that for conventional wings where the c.g. is generally forward of the mid-chord and $r_c \sim 0.5$, quasi-steady theory with F taken at some value between 0.5 and 1.0 can give a fair estimate of the flutter speed obtained from nonsteady theory.

For the sake of completeness, the divergence speed should also be investigated in any aeroelastic study. This static divergence case which is readily determined from Eqs. (1) and (2) results in the familiar equation

$$V/b\omega_\alpha\sqrt{\mu} = \sqrt{r_\alpha^2/2F[(1/2) + a]} \tag{12}$$

For certain parameters, this divergence speed may very well fall below the flutter speed of the airfoil.

References

[1] Theodorsen, Theodore, *General Theory of Aerodynamic Instability and the Mechanism of Flutter*, NACA TR 496, 1935.

[2] Theodorsen, Theodore and Garrick, I. E., *Mechanism of Flutter, A Theoretical and Experimental Investigation of the Flutter Problem*, NACA TR 685, 1940.

[3] Fung, Y. C., *An Introduction to the Theory of Aeroelasticity*, John Wiley & Sons, Inc., New York, 1955.

[4] Ashley, H. and Zartarian, G., *Piston Theory—A New Aerodynamic Tool for the Aeroelastician*, Journal of the Aeronautical Sciences, Vol. 23, No. 12, pp. 1109–1118, December, 1956.

[5] Biot, M. A. and Arnold, Lee, *Low Speed Flutter and its Physical Interpretation*, Journal of the Aeronautical Sciences, Vol. 15, No. 4, pp. 232–236, April, 1948.

Theory of Stagnation Point Heat Transfer in Dissociated Air

(*Continued from page 85*)

[12] Fay, J. A., Riddell F. R., and Kemp, N. H., *Stagnation Point Heat Transfer in Dissociated Air Flow*, Technical Notes, Jet Propulsion, Vol. 27, pp. 672–674, 1957.

[13] Fay, J. A., *The Laminar Boundary Layer in a Dissociating Gas*, Avco Research Laboratory TM-13, June, 1955.

[14] Kuo, Y. H., *Dissociation Effects in Hypersonic Viscous Flows*, Journal of the Aeronautical Sciences, Vol. 24, No. 5, pp. 345–350, May, 1957.

[15] Rose, P. H., and Stark, W. I., *Stagnation Point Heat-Transfer Measurements in Dissociated Air*, Journal of the Aeronautical Sciences, Vol. 25, No. 2, pp. 86–97, February, 1958.

An Investigation of Two-Dimensional Supersonic Base Pressures†

A. F. CHARWAT* AND J. K. YAKURA**
University of California at Los Angeles

SUMMARY

An investigation of the base pressure behind wedges at Mach Numbers 2 and 3 in the laminar and the transitional regime is reported. Temperature and velocity traverses through the mixing zone are shown and exploratory investigations of the wake vortex by use of hot wires and flow-visualization techniques are described. It is found that the laminar two-dimensional base pressure agrees well with Chapman's theoretical predictions. The shear layer exhibits gross velocity distributions characteristic of the free jet mixing zone, but also shows disturbances that originate in the expansion-turning of the oncoming boundary layer. An interesting trailing vortex is observed, which is explained in terms of nonuniform mixing rate in the wake.

INTRODUCTION

THE STRUCTURE of a wake at the base of a blunt body in supersonic flow is a particular case of a group of problems in which the field is determined by the interaction of a hyperbolic region with a region of dissipative flow. Another example of this class of problems is the separated boundary layer encountered in shock-boundary interactions. The particular importance of reaching a clear understanding not only of the phenomenological picture but also of its quantitative details stems from the characteristic sensitivity of the external supersonic flow to small changes in the shape of its boundary. The fine balance between two so different flow fields makes this case an exceptionally interesting one.

From the practical viewpoint, the pressure in the wakes of blunt bodies is of considerable importance because it can account for as much as one third of the drag of medium-range supersonic vehicles. The corresponding problem in two dimensions gained interest when it was shown that blunt trailing-edge airfoils can offer certain advantages. Besides the concern with the base pressure proper, the flow in the subsonic wake determines such critical phenomena as the heat-transfer rates and the cooling of jet nozzles located at the base of missiles, and many associated problems.

Accordingly, the supersonic wake (see Fig. 1) has received considerable attention. Early experiments led to an accumulation of data (summarized in references 1 and 2) which was found rather difficult to unify. The first analysis which explained (at least qualitatively) this complex phenomenon was due to Crocco and Lees.[3] Their formulation of the base flow structure emphasized for the first time the importance of the mixing process in determining the equilibrium between the external flow and the enclosed wake. Another approach was suggested by Chapman[4] and Korst[5] and also by Kirk,[6] but it is less general, although considerably simpler.

Crocco and Lees study the "free jet" at the edge of the supersonic flow downstream of the base. They use an integral approach whereby the essential momentum transfer is described by properly defined averages. The "dead air" region behind the base is thus energized until it can support the recompression necessary to turn the supersonic stream back to the direction of the mean flow. No account is taken of the existence of fluid in the wake.

The Chapman-Korst theory requires the conservation of mass within the wake, where momentum transfer from the external stream induces a circulatory motion. In their formulation these authors emphasize the dynamics of the streamline which divides the two flows and express the equilibrium condition by stating that the total pressure along that streamline must just suffice to support the recompression: the internal fluid is returned and conserved within the wake while the fluid external to that streamline escapes downstream.

The aforementioned model leads to a simple expression for the base pressure in two-dimensional flow,

$$\frac{P_B}{P_0} = \left\{ \frac{1 + [(\gamma - 1)/2]M_0^2}{1 + [(\gamma - 1)/2][M_0^2/(1 - U_*^2)]} \right\}^{\gamma/(\gamma-1)} \qquad (1)$$

where P_0 is the pressure downstream of the recompression region (equal, approximately, to the free-stream pressure for slender bodies) and $U_* = U/U_e$ is the velocity at the dividing streamline just ahead of the recompression referred to the external velocity. This, of course, does not constitute a solution because U_* is not known in general. However, some idealized models are available; Chapman uses his solution for laminar mixing supersonic jet free of boundary layer with stagnant air,[7] a similar solution which yields $U_* = 0.587$, and Korst attacks the problem of turbulent mixing by use of an eddy-viscosity concept. Korst's analysis is formulated in general, but carried out only for no oncoming boundary layer.

Received August 29, 1957.

† This investigation was supported by research funds of the Department of Engineering of the University of California at Los Angeles. The authors wish to thank Dr. L. L. Kavanau for his frequent and stimulating discussions.

* Associate Professor in Engineering.

** Graduate Student and Hughes fellow. Portions of the experimental program were taken from the author's M.S. thesis.

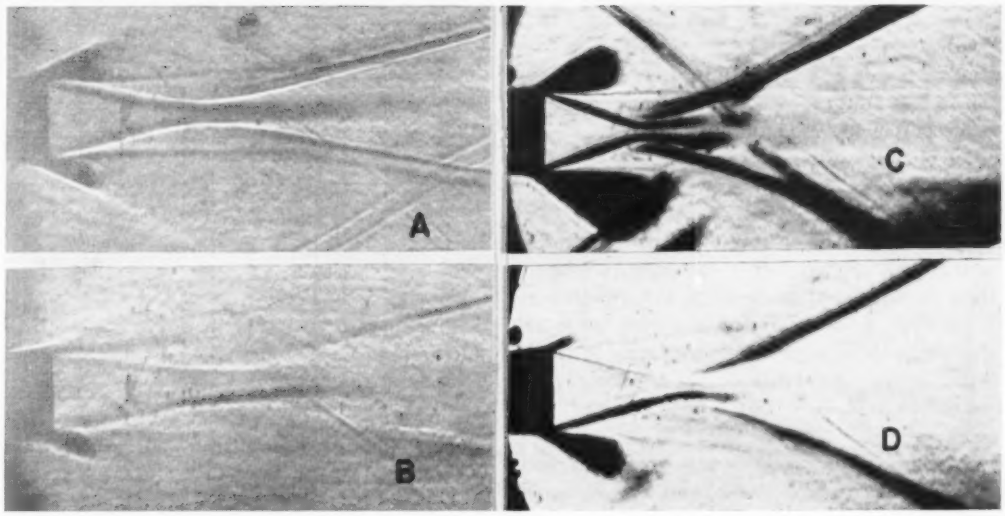

FIG. 1a. Schlieren photographs of the base wake. (A) $M = 2.8$, $R_c = 380{,}000$; (B) $M = 2.8$, $R_c = 155{,}000$; (C) $M = 2$, $R_c = 610{,}000$; (D) $M = 2$, $R_c = 130{,}000$.

Both analyses assume an isoenergetic and isobaric mixing process.

There seems little doubt that the outline of the flow field behind blunt-body bases described above is conceptually correct. However, there are many details which remain obscure. To begin with, the two-dimensional laminar wake which is solved most completely within the framework of these simplified theories has never been subject to experiment;* only the corresponding three-dimensional axisymmetric flow was studied in the laboratory.[8, 9] Furthermore, very little attention was devoted to discovering how the actual velocity distributions across the mixing layer compare with the simplified models. The only data known to the authors was obtained in reference 10, which became available during the course of the present investigations. This information is necessary to guide further work and refine the understanding of such problems as the effect of boundary layers on the structure of the inclosed "dead air" region. The experiments reported herein were designed to investigate some of these details.

Base Pressure Tests on Wedges

The base pressure measurements were conducted in a 3 by 3 in. tunnel at $M_0 = 1.98$ and $M_0 = 2.78$. The models were geometrically similar wedges with a 4:1 chord to base height ratio. The variation in Reynolds Number was obtained partly by varying the chord length of the models and partly by throttling the tunnel. The largest model had a 2-in. chord and an aspect ratio of 1.5, while the smallest chord was 0.3125 in. with an aspect ratio of 9.6. All models were cantilevered from one of the tunnel walls and spanned its width. The pressure taps in the model were brought out through the side wall at the model support. The entire assembly was two-dimensional.

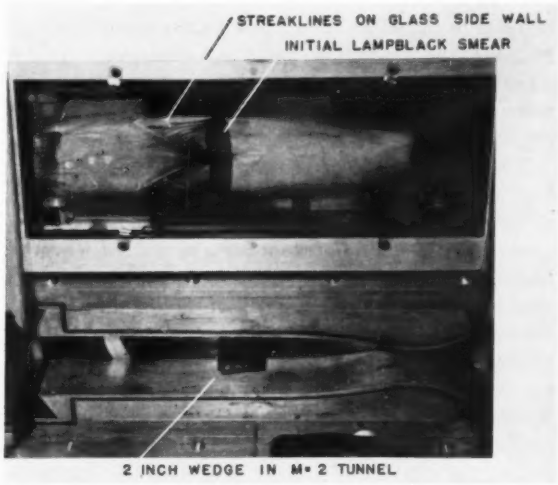

FIG. 1b. The model installed. Tunnel side wall raised showing turning of the flow and the recompression shock by lampblack streaks. Note interaction of recompression shock with tunnel floor boundary layer.

Preliminary tests were conducted to verify the uniformity of the flow and the pressure along the span of the two largest models. In both cases negligible differences existed along the entire length except very close to the wall. Both the base pressure and the surface pressure on the wedge just ahead of the base were checked. Additional flow-visualization tests showed that the boundary layer on the surface of the models was laminar and uniform throughout the range of investigation except at the tunnel wall; however, some interesting three-dimensional disturbances in the wake were observed. These are discussed in the last paragraph. Further measurements of the base pressure along the height of the bases were made, showing, in all

* Reference 4 reports data for a backward facing step. However, there exists some evidence that the base pressure is higher in that case than in the corresponding free wake.

cases, that it is uniform both in the turbulent and in the laminar regime.

The measurements of base pressure are reported in Fig. 2. The present data is extended into the turbulent regime by measurements of Gadd et al.[11] who used, at $M = 3$, the identical wedge geometry. At $M = 2$ Gadd's data is for a more slender wedge ($c/h = 8$). Noting the fairly well substantiated correlation of base pressure in the transitional regime with the parameter $\delta/h = c/h\sqrt{R_c}$ (see reference 4), it would appear that Gadd's data is displaced somewhat towards lower Reynolds Numbers in comparison with ours, such as would occur if the turbulence level were larger in their tunnel (see Fig. 4). Nonetheless, the agreement is good. For comparison, curves for a cone-cylinder[8] are also shown.

Without exception, all the evidence indicates the familiar rise in base pressure ratio from a (constant) "turbulent wake" value to a constant higher plateau for Reynolds Numbers below critical. This rise is explained by the motion of the transition to turbulence in the free jet, and the consequent variation in momentum transfer to the shear layer; below the critical Reynolds Number the transition point is presumably located downstream of the recompression region. This is the region to which Chapman's theory should apply most closely.

The scatter in the present measurements is small (at least two distinct tests are reported for each model) but there is a recurrent difference between the base-pressure ratios on different models at a fixed Reynolds Number. This difference is due, in part, to a slight change in Mach Number with Reynolds Number. It varied from 1.99 to 1.96 and from 2.78 to 2.66, respectively. A correction [using Eq. (1)] was tried, but it is too small to compensate for the observed differences. Special precautions had been taken to prevent non-uniformities in surface finish or leading-edge bluntness among the models. It seems justifiable to explain the discrepancy by a boundary-layer effect, the thickness of which (at a fixed length-Reynolds Number) is not reduced similarly to the model geometry.

The question of the appropriate boundary-layer correction remains uncertain. The thickness proper would appear to describe the oncoming velocity gradient and its effect on the expansion-turning of the flow at the edge of the base; to describe the increased resistance to momentum transfer from the mean flow, the momentum thickness would be more appropriate. The smoothing of disturbances in the profile along the mixing layer is function of X and $\sqrt{X}$ for laminar and turbulent jets respectively, where X is the distance along the wake. The base height (h) can be taken to be roughly proportional to X. In the transition regime Chapman's parameter δ/h, which correlates the data well, can be interpreted to represent a stability criterion for the boundary layer (function of its thickness) related to the distance along the shear layer available for transition. It does not follow that the same parameter should apply to the fully developed turbulent regime or

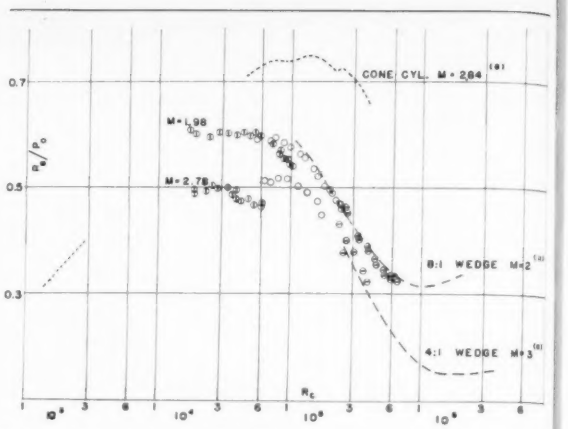

FIG. 2. Base pressure variation with Reynolds Number on 4:1 wedges.

⊖ Model chord = 2 in.
○ Model chord = 0.818 in.
① Model chord = 0.3125 in.

the pure laminar one. Fuller et al.[10] use a linear extrapolation of the momentum thickness to base height ratio to correct their data (turbulent wake) and compare it with Chapman's;[1] Gadd,[11] who used much smaller models for which the momentum thickness is essentially zero without correction, checks the aforementioned results very closely. It appears that for turbulent wakes the ratio θ/h is appropriate. The present data, in the laminar regime, is shown related to the parameters in question on Fig. 3. It is evident that the best correlation is obtained against the boundary-layer thickness proper. Moreover, the theoretical value of $U_* = 0.587$ for laminar mixing layer falls on the experimental curve.

A set of base-pressure measurements was obtained with the leading edge of the models roughened by attaching to it a strip of 00 emery cloth.

The roughened wedge surface tests were conducted on the smallest and the largest models. They are shown in Fig. 4. The effect on the base-pressure variation was to shift the curve towards lower Reynolds Numbers by increasing the tendency for turbulent transition. The final laminar base pressure became higher in accordance with the aforementioned boundary-layer effect. The turbulent wake flow regime seemed to be less affected.

The Mixing Layer

The key to the base-wake problem lies in the dynamics of the free mixing layer which separates the external flow from the internal vortex. It is necessary to know its mass and momentum distribution and its stability characteristics, as well as the influence of the oncoming boundary-layer parameters on its development.

Fig. 5 shows a number of successive traverses of the shear layer at two Mach Numbers and two Reynolds Numbers. The measurements were made with a flattened total-head tube (overall thickness 0.004 in.)

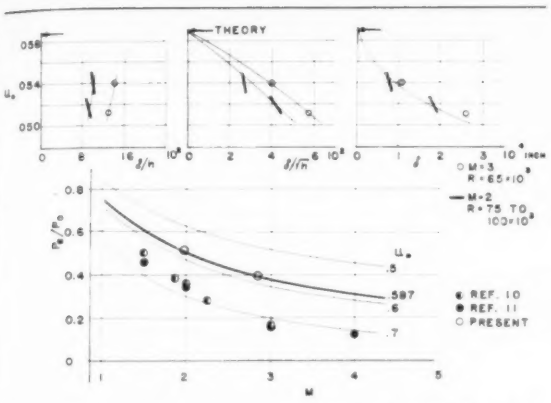

FIG. 3. Corrected mixing parameter U_* and correlations with boundary-layer parameters.

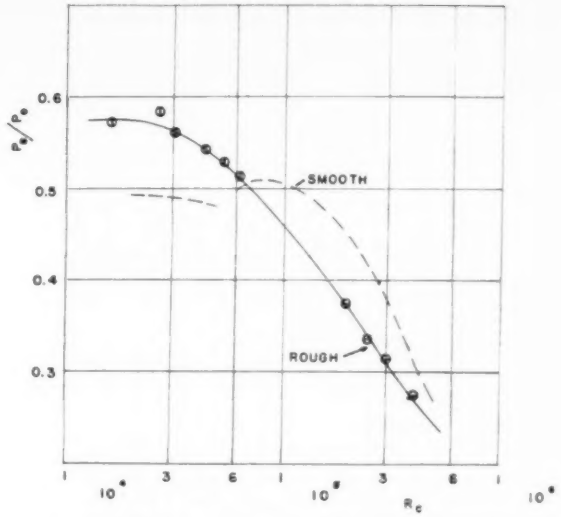

FIG. 4. The effect of surface roughness on base pressures at Mach Number 2.

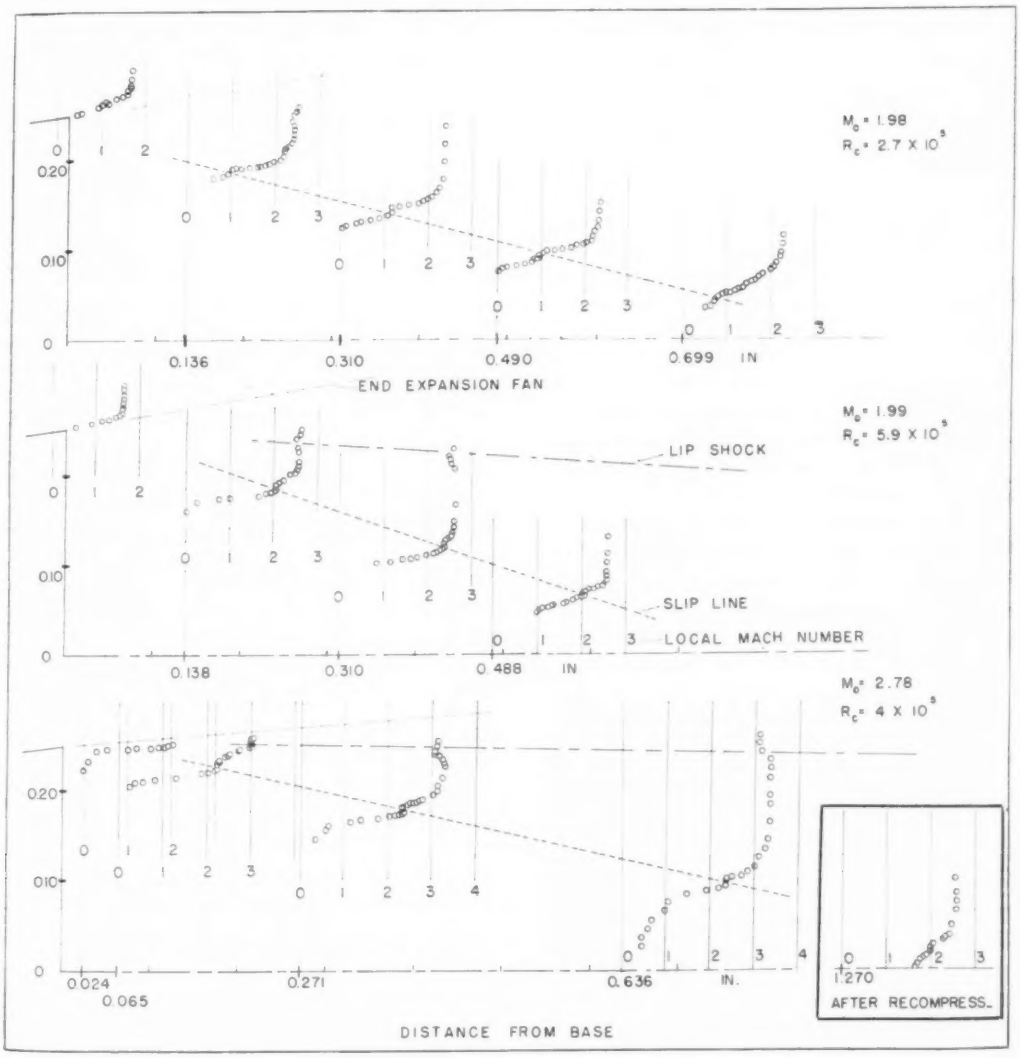

FIG. 5. The development of the mixing layer.

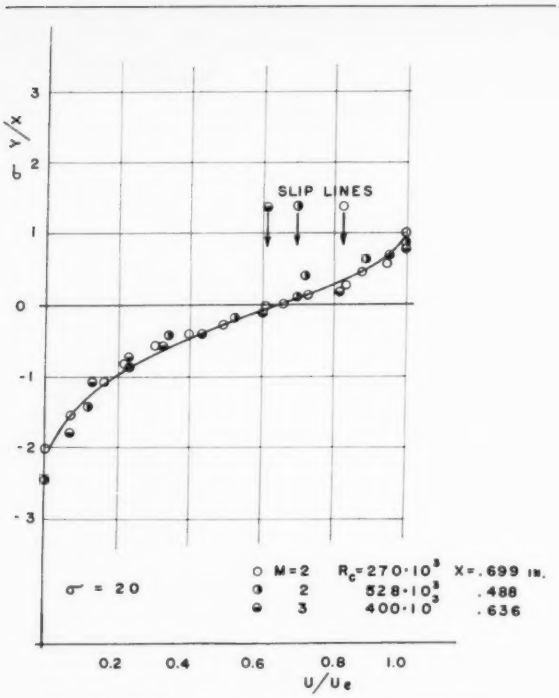

FIG. 6. Similarity test for the mixing-layer profiles.

which was lined up with the direction of the local flow in the shear layer by visual comparison on the schlieren screen. The data, which are reported in terms of local Mach Numbers, were computed on the assumption that the static pressure was constant and equal to the base pressure. This is meaningful only up to the lip shock or the base expansion fan. The structure of the hyperbolic flow, as indicated in Fig. 5, is selfconsistent, and the location of the measured dip in Mach Number at the outer edge of the layer coincides with the lip shock as viewed on the schlieren.

It is immediately evident that in the early stages of development, the shear layer resembles the theoretical profile only in its gross characteristics. In particular, a "cusp" in the velocity distribution is apparent. It diffuses but persists even across the recompression zone. This discontinuity is much stronger at the higher Mach Number. It is interpreted as follows. The oncoming supersonic flow is rotational and, in undergoing the expansion-turning at the base, a system of waves of both families is generated. When the Mach Number is greater than $\sqrt{2}$, that is, in the outer portions of the boundary layer, an expansion is reflected as an expansion into the slower layer and a compression wave is emitted into the faster one (away from the base). These shocklets coalesce to form the well known lip shock. However, when the Mach Number is less than $\sqrt{2}$, that is, in the inner portion of the rotational layer, an expansion wave is reflected inwards as a shock. The net effect of the waves reflected off the $M = \sqrt{2}$ layer (not a streamline) during the expansion is to form the slip-line noticed in the measurements.

Fig. 6 shows some profiles before recompression plotted against the turbulent similarity parameter. The origin was chosen so as to make $U_x = 0.65$ at $y = 0$. (For clarity, a limited number of specific points was plotted instead of the entire profile.) The value of the scale factor σ was chosen so as to make the inner boundary of the mixing region coincide approximately with that derived theoretically.[12] This value is $\sigma = 20.0$ for all three profiles shown in Fig. 5.

The incompressible mixing layer was found to follow the theoretical solution with σ between 12 and 14. Investigations of mixing[13] of compressible fluids at $M = 1.6$ proved that there is no essential difference between the incompressible and compressible profiles, particularly in the inner low-speed portion of the layer. The scale factor σ was found to be higher, approximately 15. The present magnitude of $\sigma = 20$ does not seem to constitute a serious difference. Note that—according to the mixing layer theory—the aforementioned factor is related to the "mixing length" as the inverse 3/2 power. Consequently a higher value of σ indicates a lower turbulence level; this may be associated with the increased stability of supersonic jets, or, more directly, with the fact that the Reynolds Number at which these profiles were measured was not yet high enough to place the flow in the "fully turbulent" regime.

For comparison, the profiles close to the base were also investigated. They were found to depart substantially from both the laminar and the turbulent distribution. A graphical comparison seems superfluous; it suffices to state that the profile has a thickness which substantially exceeds the turbulent and therefore also the laminar value. To fit it to theory in terms of the turbulent similarity parameter one would choose a value of σ in the neighborhood of 4. This fact can also be seen by inspection of Fig. 4. At $M = 3$ the profiles escape interpretation because of the proximity of the expansion fan, but they are well defined at $M = 2$; the shear layer does not grow as rapidly as would be expected.

Finally, it is worthy of note that the inflection in the boundary-layer profiles denoted before as the internal slipline finds itself located quite near the value of $U_* = U/U_e$ which corresponds to the "dividing-streamline." Since the dynamic energy of that streamline determines the recompression, the occurrence of this disturbance may bear on the resulting base pressure.

Unfortunately, we were unable to study the laminar mixing region profiles because of the small size of the model.

Flow in the Wake

The mass induced by the mixing is small, and therefore the velocities and energy levels in the recirculating flow are low and do not influence the dynamics of the field. The subsonic "base vortex" constitutes a separate problem determined entirely by the conditions at the boundary. An elegant analysis of flows with

closed streamlines was published recently[14, 15] and Batchelor[16] proposed a model of laminar wakes based on this theory. It predicts that the vorticity is constant in the region, that is, if a single stationary vortex existed there, it would be of the solid body type.

We conducted exploratory hot-wire traverses of the wake region which are given in Fig. 7 as ratios of the heat-transfer coefficient λ to its value at the centerline. We did not feel justified in reducing the data to velocities because of the uncertainty in the wire calibration. However, the relation between λ and U is monotonic, and the increase in λ can be interpreted as an increase in U. Thus no stagnation surface dividing the downstream flow from the reverse flow in the wake is evident from the measurement. The reason is that the measurements represent an average (root-mean-squared) velocity because the wake flow is unsteady. Observations near the inner edge of the mixing layer showed large aperiodic fluctuations even at the lower Reynolds Number. These waves of the boundary are imposed on the wake; their period is long with respect to the characteristic time of the shear layer (that is, they do not necessarily represent turbulence in the mixing layer) but short with respect to the slower wake flow, and they cause it to break up. An unstable vortex can also be inferred from observations of an aperiodic vortex shedding into the wake observed on spark-schlieren photographs by Chapman.[1] This situation probably persists to very low Reynolds Numbers, much below the critical, where the shear-layer proper is laminar.

It seemed interesting to verify the existence of the "recirculation" of mass in the wake. The base of the wedge was covered with a strip of a pH indicator and ammonia was admitted into the wake through a total pressure tube. When the tube mouth was brought forward past the wake "throat," the recirculation carried the vapors to the base as evidenced by a change in color of the indicator. The effect was roughly uniform over the base height; there was no time delay in color change near the edge as compared to the centerline. This also points to a high degree of turbulent mass-mixing in the wake. Incidentally, the region near the "throat" downstream of which the vapors would not penetrate into the wake at all coincided with the recompression region as viewed on the schlieren; thus the wake was closed.

Fig. 7 also shows a total temperature traverse of the wake. The wake recovery factor was found to be 0.945. This is high enough to justify the assumption of isoenergetic flow. The fact that the recovery temperature in the base wake is high and, also that the convective heat-transfer characteristics are poor suggests that the base region may lead to aerodynamic heating problems at hypersonic speeds which are at least as severe as in the forward stagnation region.

Particular attention was given to the study of the uniformity of the pressure along the height of the base. No significant pressure distribution was found in either the turbulent or the laminar regime. The same was

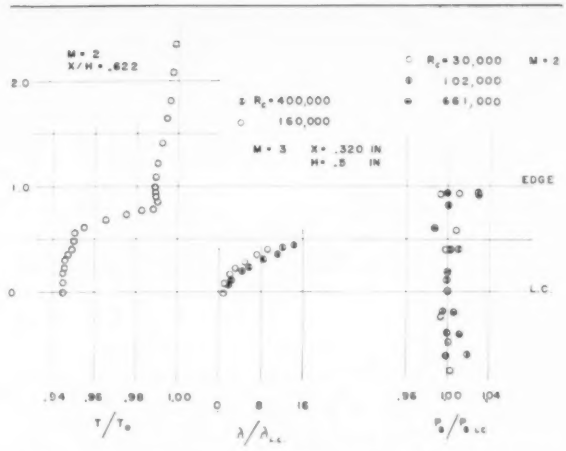

FIG. 7. Traverses across the mixing layer: (a) temperature to free-stream total temperature, (b) heat-transfer coefficient from 0.003-in. wires to its value at the wake centerline, (c) variation of base pressure across the base.

true for the pressure along the centerline in the stream direction except, of course, near the recompression region (incidentally, the data is not accurate there since significant disturbances are introduced by the probe). The two-dimensional wake is thus isobaric, which is not so in the case of bodies of revolution.[8] It would appear that the gradual recompression characteristic of converging conical flows, which is responsible for the higher mean value of base pressure, also gives rise to the radial distribution of pressure in axisymmetric wakes.

OBSERVATIONS OF NONUNIFORM WAKE MIXING

An interesting observation was made during attempts to visualize the flow pattern. Fig. 8 shows the streaklines over the base; these are lampblack deposits obtained by coating the base with a kerosene-lampblack suspension. A trailing vortex with the axis parallel to the flow is seen to be shed from the wake. For a short time before the kerosene evaporated we could actually observe the circulation. Note that there are actually 4 pairs of these vortices. A pair can be faintly seen at either end of the span. The other two pairs, of

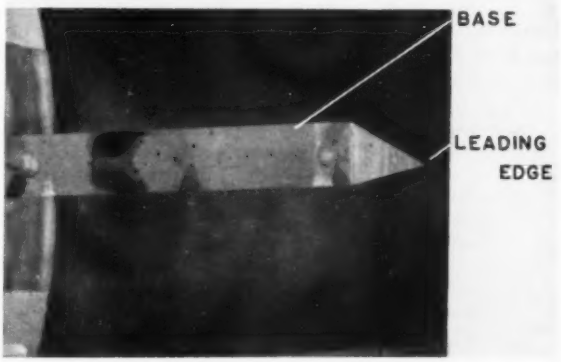

FIG. 8. Lampblack streaks evidencing the shedding of a vortex downstream from the base; $M = 2$, $R_c = 600{,}000$.

which only one was properly illuminated and registered clearly on the photograph, are located symmetrically on each side of mid-span.

The phenomenon, as well as the location of the vortices, was consistently reproducible at $M_0 = 2$. However, at higher Mach Number we were unable to observe any consistent flow structure whatever over the base. (It is possible that the violence of the starting shock and the higher shear rates tending to carry the fluid downstream prevented a successful application of this technique.)

The trailing vortex is a three-dimensional disturbance with its axis perpendicular to the mixing vortex; incidentally, the latter was also observed by lampblack streaklines formed on the tunnel side walls.

The shedding of vorticity occurred at the intersection of the base with the Mach line originating at the junction of the leading edge with the wall. It seemed that this slight disturbance (which did not affect the surface boundary layer or modify the surface pressure noticeably) was sufficient to alter the stability characteristics of the free-shear layer and induce an earlier transition. Thus the mixing in the free-shear layer was increased and resulted in a stronger (mixing) vortex in the affected portion of the wake span. The excess vorticity had to be shed at the junction of the disturbed and the undisturbed regions to satisfy vorticity conservation laws. This gave rise to the appearance of the trailing vortex. To verify this hypothesis we glued sandpaper strips over arbitrary portions of the span to artificially destabilize the boundary layer. Indeed, we found that a vortex was shed downstream at the edge of the disturbed region every time.

Despite the existence of this three-dimensional disturbance, the base pressure remained uniform across the span within the accuracy of the readings. The three-dimensional motion appeared to be too slow to affect the basic wake pattern. Still, to ascertain definitely that the pressures, and, principally, the critical Reynolds Number as determined by the stability of the mixing layer, were representative of truly two-dimensional flows, two thin plates were brought in from downstream against the base. These end plates (perpendicular to the span) effectively isolated the central undisturbed portion of the wake from the disturbed end-zones. The entire series of tests was repeated and it was found that neither the magnitude of the base pressure nor the critical Reynolds Number were altered.

It was concluded that the data presented in this paper were not vitiated by the existence of the three-dimensional trailing vortex. However, it is possible that such three-dimensional disturbances do affect transition in the wake over the local portion of the span where they occur. In our tests, the model used in the critical Reynolds Number region had so large an aspect ratio that the disturbance may not have diffused to the center of the span where the pressure tap was located.

References

[1] Chapman, Dean R., Wimbrow, William R., and Kester, Robert H., *Experimental Investigation of Base Pressure on Blunt-Trailing-Edge Wings at Supersonic Velocities*, NACA Report 1109, 1952.

[2] Love, S. E., *The Base Pressure at Supersonic Speeds on Two-Dimensional Airfoils and Bodies of Revolution Having Turbulent Boundary Layers*, NACA RM L53 CO2, 1953.

[3] Crocco, L., and Lees, Lester, *A Mixing Theory for the Interaction Between Dissipative Flows and Nearly Isentropic Streams*, Journal of the Aeronautical Sciences, Vol. 19, No. 10, pp. 649–676, October, 1952.

[4] Chapman, D. R., Kuehn, D. M., and Larson, H. K., *Investigation of Separated Flows in Supersonic and Subsonic Streams With Emphasis on the Effect of Transition*, NACA TN 3869, 1957.

[5] Korst, H. H., *A Theory for Base Pressures in Transonic and Supersonic Flow*, Nat. Conf. Appl. Mech., 1956, ASME Preprint 56-APM-30.

[6] Kirk, F. N., *An Approximate Theory of Base Pressure in Two-Dimensional Flow at Supersonic Speeds*, RAE Tech. Note Aero 2377, 1956.

[7] Chapman, D. R., *Laminar Mixing of a Compressible Fluid*, NACA TN 1800, 1949.

[8] Kavanau, L. L., *Results of Some Base Pressure Experiments at Intermediate Reynolds Numbers with $M = 2.84$*, Journal of the Aeronautical Sciences, Vol. 21, No. 4, pp. 257–260, 274, April, 1954.

[9] Van Hise, V., *Investigation of Variation in Base Pressure Over the Reynolds Number Range in Which Transition Occurs for Nonlifting Bodies of Revolution at Mach Numbers From 1.62 to 2.62*, NACA TN 3869, 1957.

[10] Fuller, L. and Reid, J., *Experiments on Two-Dimensional Base Flow at $M = 2.4$*, Brit. RAE Report Aero 2569, 1956.

[11] Gadd, G. E., Holder, D. W., and Regan, J. D., *Base Pressures in Supersonic Flow*, Brit. ARC Tech. Rep. CP No. 271, 1956.

[12] Tollmien, W., *Calculation of Turbulent Expansion Processes*, NACA TN 1085, 1945.

[13] Gooderum, P. B., Wood, G. P., and Brevoort, J., *Investigation With an Interferometer of the Turbulent Mixing of a Free Supersonic Jet*, NACA Rep. 963, 1950.

[14] Batchelor, G. K., *On Steady Laminar Flow With Closed Streamlines at Large Reynolds Numbers*, J. Fluid Mechanics, Vol. 1, p. 177, July, 1956.

[15] Wood, W. W., *Boundary Layers Whose Streamlines are Closed*, J. Fluid Mechanics, Vol. 2, p. 77, January, 1957.

[16] Batchelor, G. K., *A Proposal Concerning Laminar Wakes Behind Bluff Bodies at Large Reynolds Numbers*, Fluid Mechanics, Vol. 1, p. 388, October, 1956.

Readers' Forum

BRIEF REPORTS of investigations in the aeronautical sciences and discussions of papers published in the JOURNAL are presented in this special department. Entries must be restricted to a maximum of 1,300 words or the equivalent of one JOURNAL page including formulas and illustrations. Publication is completed as soon as possible after receipt of the material. The Editorial Committee does not hold itself responsible for the opinions expressed by the correspondents.

Contents

A Remark on Stability Equations ..... ERICH SPONDER 129

An Approximation of the Boundary of a Supersonic Axisymmetric Jet Exhausting Into a Supersonic Stream ..... E. S. LOVE 130

Estimating Aerodynamic Characteristic Times in Hypersonic Flow ..... SINCLAIRE M. SCALA 131

On the Conservativeness of Various Distributed Force Systems ..... SOL R. BODNER 132

A New Method for Computing Drag Coefficients from Ballistic Range Data ..... ALVIN SEIFF 133

On the Buckling Problem of Shallow Spherical Shells Under External Pressure ..... H. J. WEINITSCHKE 134

Effect of Dissolution on Oleopneumatic Shock-Strut Performance ..... CHARLES W. BERT 135

Analytical Results of Certain Nonlinear Flutter Problems ..... S. F. SHEN AND C. C. HSU 136

Stability Equations for Conical Shells ..... JOSEPH KEMPNER 137

Some Remarks on the Foundations of Piston Theory and Supersonic-Hypersonic Similarity ..... G. A. BIRD 138

On the Eigenvector Direction of Turboblading with Lashing Wire ..... MILOMIR M. STANIŠIĆ 139

Concerning the Rigidity of Elastic Structures ..... M. ZAID 141

The Effect of Internal Pressure on the Buckling Stress of Thin-Walled Circular Cylinders Under Combined Axial Compression and Torsion ..... LEONARD A. HARRIS, HERBERT S. SUER, AND WILLIAM T. SKENE 142

On Laminar Separation Bubbles ..... KENNETH R. CRAMER 143

A Remark on Stability Equations

Erich Sponder
Project Engineer, Bölkow-Entwicklungen, Stuttgart Airport, Germany

September 13, 1957

LET US CONSIDER the simplified case of a purely yawing airplane, as shown in Fig. 1. The airplane may proceed horizontally at constant speed without experiencing any drag, thrust, or side force but will experience a yawing moment N if there is generated an angle of sideslip β by a small disturbance. A damping in yaw, on the contrary, will not exist. Consequently, the flight path of the c.g. must be a straight line along which yawing oscillations may occur since the airplane is supposed to be statically stable: $\partial N/\partial\beta < 0$ (weathercock stability). With a moment of inertia I about the c.g., the equation for the yawing motion becomes

$$I(d^2\beta/dt^2) - (\partial N/\partial\beta)\beta = 0$$

which describes an undamped permanent oscillation.

Now, let us add a side force, or cross-wind force, Y, as indicated in Fig. 2. After a disturbance in yaw, the side force $Y = (\partial Y/\partial\beta)\beta$ (where $\partial Y/\partial\beta > 0$) pushes the airplane off its course to the right, so that there will be a small departure from the original direction of the c.g. (dashed line). The description of the ensuing motion now has to distinguish carefully among the three angles β, χ, and ψ, where $\psi = \beta + \chi$. Again, a damping in yaw will be left out. Then we have

$$I(d^2\psi/dt^2) - (\partial N/\partial\beta)\beta = 0$$

different from the former expression, and, with the mass m of the airplane and its speed V,

$$mV(d\chi/dt) = (\partial Y/\partial\beta)\beta$$

Writing the term $I(d^2\psi/dt^2)$ of the first equation as $I[(d^2\beta/dt^2) + d^2\chi/dt^2]$, we can eliminate $d^2\chi/dt^2$ by differentiating the

Contributors Please Note

Readers' Forum items must be confined to the equivalent of one page in the *Journal*. Contributions that exceed this limit will be returned to the authors for condensation and rewrite. To avoid inconvenience and delay, please adhere to the following specifications:

(1) Five, double-spaced, typewritten, manuscript pages ($8^1/_2$ by 11 in.), including wide margins, formulas, and headings equal one printed page.

(2) For every illustration, deduct at least one-half or as much as one manuscript page, depending on the size of the illustration.

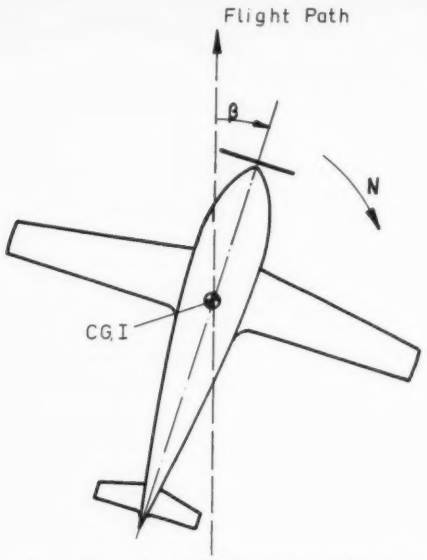

FIG. 1. A purely yawing airplane along a rigid, straight flight path.

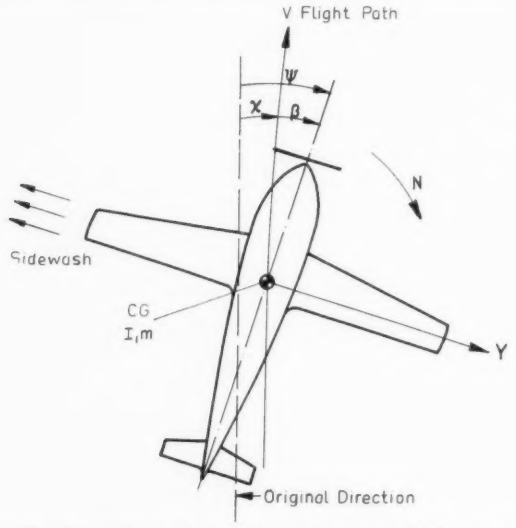

FIG. 2. A purely yawing airplane along a yielding, curved flight path.

second equation; hence

$$I(d^2\beta/dt^2) + (\partial Y/\partial\beta)\,(I/mV)\,(d\beta/dt) - (\partial N/\partial\beta)\beta = 0$$

This result is quite remarkable. Although no damping in yaw was introduced at all, the β oscillation of the airplane about its curved flight path will gradually disappear since the coefficient of $d\beta/dt$ is essentially positive.

This is the formal result of a treatment which proceeds from simplified to more complicated modes of motions as is usual in lateral dynamics. Yet, it doesn't help to give a clear physical understanding of this particular damping effect. In order to shed some light on this question, one may try to compare the curved flight path of the yawing airplane with the motion of a solid body which slides horizontally without friction along a curved wall. But such attempts cannot yield any similar results, because no energy is dissipated.

The correct explanation of this damping effect seems to be quite obvious when it is found by closer examination. The side force Y can be produced only if there is an equivalent amount of momentum imparted to the surrounding air in the opposite direction. And this "sidewash," as it is named in Fig. 2, carries away some energy which clears up the decrease of the yawing oscillation.

A complete treatment of the airplane dynamics contains, of course, terms of the same significance, though in a more involved form. An inspection of the stability quartics shows them distinctly in the coefficient B (see Durand, *Aerodynamic Theory*, vol. V, p. 171 for the longitudinal motion, and p. 186 for the lateral motion). The shortened notations z_w and y_v mean exactly the slopes of the lift curve and of the side-force curve respectively.

Besides, Fig. 1 corresponds to an experimental investigation of the yawing mode by a wind-tunnel test, while Fig. 2, with one more lateral degree of freedom, better approaches the airplane's motion in free flight. Since this effect is of the same nature as an induced drag, which is necessarily connected with a lift, any sideslipping, pitching, or reeling motion of airplanes, projectiles, and the like, will experience a damping which sometimes may be considered as a desirable gift for some improvement of the dynamic stability.

An Approximation of the Boundary of a Supersonic Axisymmetric Jet Exhausting Into a Supersonic Stream

E. S. Love
Head, Hypersonic Tunnels Branch, Langley Aeronautical Laboratory, NACA, Langley Field, Va.
September 20, 1957

SYMBOLS

M_∞	=	free-stream Mach Number
M_j	=	jet Mach Number immediately ahead of exit
β	=	boat-tail angle
θ	=	semidivergence angle of conical nozzle
r_j	=	radius of jet at exit
r	=	distance normal to jet axis
x	=	distance from plane of jet exit measured parallel to jet axis
p_j	=	jet static pressure immediately ahead of jet exit
p_∞	=	free-stream static pressure
γ	=	ratio of specific heats

INTRODUCTION

FOR SHORT DISTANCES DOWNSTREAM of the exit of an axisymmetric supersonic jet exhausting into a supersonic stream—i.e., distances of the order of one jet exit radius—the boundary between the jet and the stream may be satisfactorily predicted by the use of the boundary of the jet that exhausts into still air at a pressure ratio which produces the same initial inclination of the boundary as the jet exhausting into the supersonic stream. However, for appreciable distances downstream of the jet exit, a satisfactory prediction of the boundary necessitates, at present, a tedious application of the method of characteristics. The need for a simpler solution stimulated the examination of an approximate method summarized in this note.

DISCUSSION

The approximate method is proposed for flows in which the local Mach Numbers on either side of the boundary are sufficiently high to permit use of shock-expansion techniques. The method is restricted to the portion of the boundary ahead of the maximum diameter of the free jet (the method falls apart at the maximum diameter and beyond), to positive initial inclinations of the boundary, and, probably, to moderate static pressure ratios. Both the expansive turning and the compressive turning of flow adjacent to the boundary that occurs after the boundary has reached its initial inclination are assumed to be isentropic. The problem of calculating the boundary shape is simplified by

considering the shape to be determined by only three effects. These are: an expansion of the ambient flow by turning along the boundary, a compression of the jet flow by turning along the boundary, and an effective expansion of the overall jet flow in proceeding downstream that is governed by the change in cross-sectional area of the jet flow. The latter two effects are counteracting but produce a resulting effect which, within this approximation, must equal the expansive effect of the ambient flow.

The initial calculations follow a conventional characteristics solution: the initial inclination of the boundary is calculated and assumed to hold over a short distance downstream of the jet exit (for 0.1 r_j in these calculations), and the initial properties of the flow on either side of the boundary are determined. At this point the approximate method is introduced. It is a step-by-step procedure in which a small change in the slope of the boundary is introduced and the values of x/r_j and r/r_j satisfying this change in slope by means of the aforementioned effects are calculated from one-dimensional relations and Prandtl-Meyer turning. A standard change-in-slope increment of 1/2° was used in the examples to follow; other calculations showed that 1° increments changed the approximate solution negligibly, while 2° increments were unsatisfactory. Details of the calculations will be omitted; briefly, a typical step in the calculations involves the calculation of the change in pressure of the ambient flow at the boundary in expanding 1/2°, the change in pressure of the jet flow at the boundary in compressing 1/2°, and the change in area of the jet flow (expansion of the jet flow) that is necessary to create a pressure balance at the boundary. From this newly determined area and the slope of the boundary, the values of x/r_j and r/r_j may be calculated. Throughout the calculations the effective throat area that is used to determine the values of r is that given by the Mach Number of the jet flow at the point where the approximate method is first applied (at $x/r_j = 0.1$ in these calculations). The use of conventional flow tables simplifies the calculations.

Comparisons of the theoretical exact boundary, given by the method of characteristics, and the approximate boundary are shown in Fig. 1. The exact boundary for Fig. 1(b) was obtained from reference 1; the value of γ for the jet flow and ambient flow of this calculation was 1.405. For the remaining boundaries, γ was 1.400. This small difference in γ is of no consequence in the comparisons. For Fig. 1(a) the Mach Numbers of the jet flow and ambient flow adjacent to the boundary just downstream of the exit are 3.30 and 3.57, respectively. For Fig. 1(b) these Mach Numbers are 2.62 and 1.72, respectively. In view of the lower Mach Numbers involved, it is not surprising to find that the agreement between the exact and the approximate boundary is poorer for Fig. 1(b). To facilitate this comparison, portions of the boundaries of Fig. 1(a) have been presented in Fig. 1(c) to the same scale as those in Fig. 1(b).

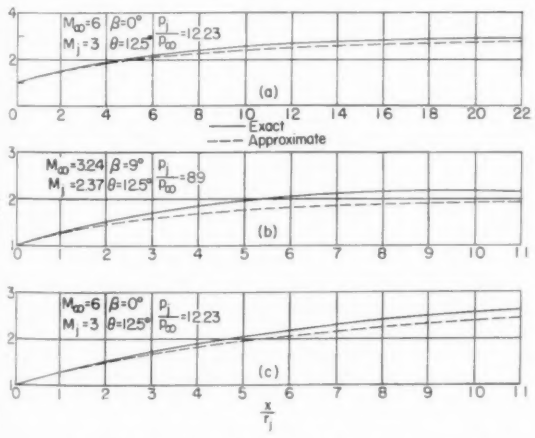

FIG. 1. Comparison of exact boundary with approximate boundary.

In spite of the gross simplifications involved, the approximate method yields a fair prediction that may be useful in engineering applications. A manual calculation of the approximate boundary requires about 1 hour (with the aid of flow tables) as compared to several days for a manual calculation of the exact boundary. In all cases examined, the approximate boundary falls beneath the exact boundary.

REFERENCE

[1] Schäfer, M., *Steady Supersonic Flows*, Reports and Translations No. 996, British M.A.P. Völkenrode, May 1, 1948.

Estimating Aerodynamic Characteristic Times in Hypersonic Flow

Sinclaire M. Scala
Missile and Ordnance Systems Department, General Electric Company, Philadelphia, Pa.
September 23, 1957

ONE OF THE MAJOR PROBLEMS associated with the flight of an object at hypersonic speed is the determination of the effect of the shock wave on the air so that the state of the dissociated and ionized gas may be evaluated in the vicinity of the body.

If one wishes to determine whether thermochemical equilibrium exists at a particular region in the flow field, for example, at the outer edge of the boundary layer, not only must the rates be known at which an equilibrium state is approached, but the aerodynamic characteristic times must also be known for each point in the region. The aerodynamic characteristic time is defined as the time required for a gas particle to pass through the shock and reach a particular point in the flow field.

The presence of a blunt body completely distorts the velocity field downstream from the shock so that the aerodynamic characteristic time is a function of the particle path selected and does not vary linearly with distance. Hence, the treatment in reference 1 cannot be used directly to determine the departure from equilibrium at the outer edge of the boundary layer. Note that the latter must be known if one is to apply the outer boundary conditions properly to a heat-transfer analysis.

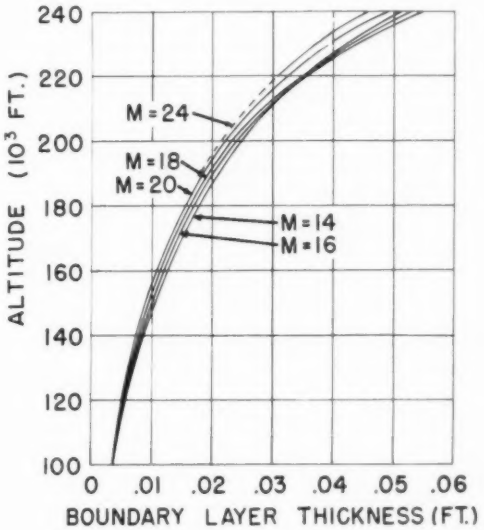

FIG. 1. Nominal boundary-layer thickness.

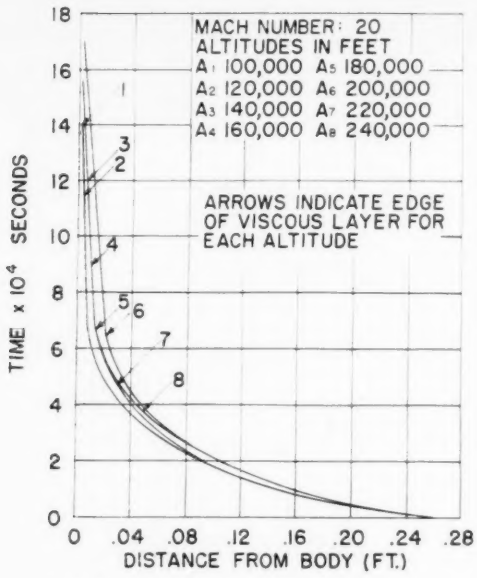
MACH NUMBER: 20
ALTITUDES IN FEET
A1 100,000 A5 180,000
A2 120,000 A6 200,000
A3 140,000 A7 220,000
A4 160,000 A8 240,000
ARROWS INDICATE EDGE OF VISCOUS LAYER FOR EACH ALTITUDE
TIME x 10^4 SECONDS
DISTANCE FROM BODY (FT.)
0 .04 .08 .12 .16 .20 .24 .28
0 2 4 6 8 10 12 14 16 18
1 2 3 4 5 6 7 8

FIG. 2. Aerodynamic characteristic times.

This note concerns itself with some first estimates of the aerodynamic characteristic times in the vicinity of the stagnation point. In Fig. 1 are shown nominal boundary-layer thicknesses, computed for a 2-ft. radius sphere. These thicknesses were computed over a wide range of altitudes and Mach Numbers on the assumption that chemical reactions are frozen and that the flow is laminar.[2] It appears that the nominal boundary-layer thickness is a sensitive function of altitude but is relatively insensitive to Mach Number.

For the sake of simplicity, the thermochemical problem is split from the gas-dynamics problem. It is further assumed that the structure of the velocity field, at least at the stagnation point, may be determined from a hypersonic approximation.[3] Note that the detachment distance has been assumed to be given by $\delta/R_B = 0.13$, which seems to be in agreement with recent theory and experiment.[4] Fig. 2 then follows directly.

For the characteristic times indicated, it appears that there may be insufficient time for thermochemical equilibrium to be established at the stagnation point at the higher altitudes.

References

[1] Wood, G. P., *Calculations of the Rate of Thermal Dissociation of Air Behind Normal Shock Waves at Mach Numbers of 10, 12, and 14*, NACA TN 3634, April, 1956.

[2] Scala, S. M. and Sutton, G. W., *The Temperature and Concentration Profiles in a Hypersonic Boundary Layer with Combustion, Blowing, or Sublimation at the Wall*, General Electric Co. T.I.S. 57SD406, February 4, 1957.

[3] Li, Ting Yi, and Geiger, R., *Stagnation Point of a Blunt Body in Hypersonic Flow*," Journal of the Aeronautical Sciences, Vol. 24, No. 1, pp. 25–32, January, 1957.

[4] Heybey, W. H., *Shock Distances in Front of Symmetrical Bodies*, Navord Report 3594, December, 1953.

On the Conservativeness of Various Distributed Force Systems

Sol R. Bodner

Assistant Professor of Engineering, Brown University, Providence, R. I.

September 23, 1957

THE NECESSITY of determining the conservativeness of force systems in instability problems is discussed in reference 1. It is shown that, whereas kinetic methods are generally applicable for the determination of instability loads, the statical methods usually employed are valid only for conservative and nongyroscopic systems. Small changes in the character of the loading could make an otherwise conservative system nonconservative and cause a large change in the magnitude of the buckling load. The buckling load of the cantilever column example in reference 1 is, for tangential end loading, eight times that for conservative, constant directional loading.

Two papers have appeared recently[2, 3] which have treated the buckling of circular rings (or infinitely long cylindrical shells) under various distributed force systems. Different values of the instability load were obtained for the various systems. Since there appears to be only slight differences in the character of these systems, it is of interest to examine them in regard to their conservativeness and their properties with respect to the ring buckling problem. These force systems are: (1) hydrostatic pressure, (2) constant directional pressure, and (3) centrally directed pressure. The magnitude of the pressure is assumed to be constant during buckling. Since a circular ring buckles in an inextensional mode, the magnitude of the total applied force also remains constant. The direction of the resultant force on each ring element does change for systems 1 and 3. It is this change in force direction that accounts for the difference in buckling loads between the systems.

Hydrostatic Pressure

The work done by a constant hydrostatic pressure p acting upon an enclosed volume as the volume contracts by an amount ΔV is $p\Delta V$. A proof of this expression as well as a proof that such a system is conservative appears in texts on hydrodynamics —e.g., pp. 13, 14 of reference 4. This system is also conservative for variable pressure if the pressure can be expressed as a continuous and single-valued function of the volume.

The buckling load of a circular ring under hydrostatic pressure is, in usual notation,

$$q = 3\,EI/R^3 \tag{1}$$

where q is the load per unit circumferential length. The work done by the hydrostatic force system during buckling involves linear and higher terms in the buckling displacements and their derivatives. The linear terms must cancel out in the expression for the total energy since the buckled mode is an equilibrium position, and it is the quadratic terms that enter into the buckling criterion. The quadratic terms in the work done by the hydrostatic force system are given on p. 142 of reference 2.

On the basis of physical reasoning, it seems that the work done by the hydrostatic force system during ring buckling would be greater than that of any other conservative system. (A system in which the force is defined to be in the direction of the instantaneous motion of the element on which it acts would depend upon the path and hence be nonconservative.) The ring buckling load for hydrostatic pressure would therefore be expected to be lower than that for other uniformly distributed conservative force systems.

Constant Directional Pressure

The constant directional pressure force system is defined as one in which the direction of the pressure remains constant irrespective of any changes in the position of the elements. Since the work done by a force that is constant in direction and magnitude depends only upon the initial and final configurations, this system is conservative. Although such a force field is easily defined, it would be difficult to devise an experimental setup in which such a field is applied to a ring.

During ring buckling due to this force system the force vector on each ring element translates but does not rotate. The expression for the work done therefore involves only linear terms in the displacements and their derivatives since the quadratic terms arise due to rotation of the elements. These linear terms, as stated previously, do not enter into the buckling criterion. Buckling in

this case, as in the Euler column, is governed only by the energy of the induced bending stresses and the part of the work done by the prebuckling membrane stresses which involves nonlinear displacement terms.

The instability load of a circular ring subjected to a uniform circumferential pressure of the kind considered here is given by Eq. (24) of reference 2 (upon setting $\nu = 0$) as

$$q = 4EI/R^3 \tag{2}$$

Centrally Directed Pressure

This force system has been used in reference 3 in relation to the ring buckling problem. During buckling the force vector on each ring element remains directed toward a common pole (the ring center) and therefore both translates and rotates. The work done by such a unit force during buckling is the product of the force and the change in the distance of the element from the pole. The work is therefore independent of the path so that the force field is conservative. If the force intensity were not constant but depended in a continuous and single valued manner upon the displacement from the pole, then the system would still be conservative—e.g., the general central force problem.

The buckling load for centrally directed pressure is given by Eq. (37) of reference 3 as

$$q = 4.5\ EI/R^3 \tag{3}$$

The part of the work done by this force system which involves quadratic displacement terms is negative for the ring buckling displacements. (Eq. (15) of reference 3 is actually a potential energy expression and hence is the negative of the corresponding work term.) The buckling load for this case can therefore be expected to be greater than that of case 2. It is of interest to note that the quadratic terms in the expression for the work done by the external force system are positive for case 1, zero for case 2, and negative for case 3.

References

[1] Ziegler, H., *Linear Elastic Stability*, ZAMP, Vol. 4, 1953.

[2] Pearson, C. E., *General Theory of Elastic Stability*, Quart. Appl. Math., Vol. 14, No. 2, p. 133, July, 1956.

[3] Boresi, A. P., *A Refinement of the Theory of Buckling of Rings under Uniform Pressure*, J. Appl. Mech., Vol. 22, No. 1, p. 95, March, 1955.

[4] Milne-Thomson, L. M., *Theoretical Hydrodynamics*, 2nd Ed.; Macmillan and Co., Ltd., London, 1949.

A New Method for Computing Drag Coefficients from Ballistic Range Data

Alvin Seiff

Aeronautical Research Scientist, Ames Aeronautical Laboratory, NACA, Moffett Field, Calif.

September 26, 1957

Presently available methods for computing the drag coefficient from time-distance data obtained in ballistics ranges are satisfactory but laborious. The drag force cannot be regarded as constant over long intervals of model flight because of the variation in dynamic pressure with model velocity. The resulting deviation from uniformly decelerated motion has led to one procedure in which the time-distance record is represented by a power series expansion which is fitted to the data by least squares[1] and another in which iterations are performed starting with uniformly decelerated motion as a first approximation.[2]

Some of the author's associates were using a graphical procedure for a first check on time-distance data from the Ames supersonic free-flight wind tunnel. Average velocities in successive intervals were plotted as a function of distance to determine the smoothness of the data. Some of the curves were remarkably linear, and this suggested that one should simply take the slope of the line as a measure of the drag coefficient. However, the equation of decelerating motion

$$C_D(1/2)\rho V^2 A = -m(dV/dt) = -mV(dV/dx) \tag{1}$$

shows that dV/dx will not be constant except in the limit of vanishing velocity loss, so this procedure will have shortcomings for cases where the velocity loss is very large. It should be noted that the variations in dV/dx are about half as great as the variations in dV/dt so that the plot of velocity against distance does have merit compared to the plot of velocity against time.

These observations caused the author to look for some presentation of the data that would be linear even in the case of large velocity loss and such a presentation was quickly found. By expressing Eq. (1) as

$$d(\ln V)/dx = -KC_D \tag{2}$$

where

$$K = \rho A/2m$$

it can be seen that $\ln V$ is linear in x as long as C_D is constant. Thus, a plot of $\ln V$ against x should give a straight line whose slope is $-KC_D$ in which K is known. This method of data analysis seemed to offer the advantages of simplicity and exactness (within the limit of the assumption of constant C_D) in that no terms of a series were neglected. However, the time-distance data must be converted to velocity-distance data which involves a hidden pitfall. The velocity obtained by dividing a given distance interval by the corresponding time interval is not the velocity at the center of the interval because velocity is not linear with distance.

The point within the interval at which the average velocity in the interval equals the local velocity must, therefore, be found. We integrate Eq. (2) to obtain

$$V = V_i e^{-KC_D x} \tag{3}$$

where V_i is the initial velocity. A second integration over the length and duration of the interval, X and T, gives

$$T = (1/KC_D V_i)\ (e^{KC_D X} - 1) = (1/KC_D)\ [(1/V_f) - (1/V_i)] \tag{4}$$

With this, we can form the average velocity, X/T, and set it equal

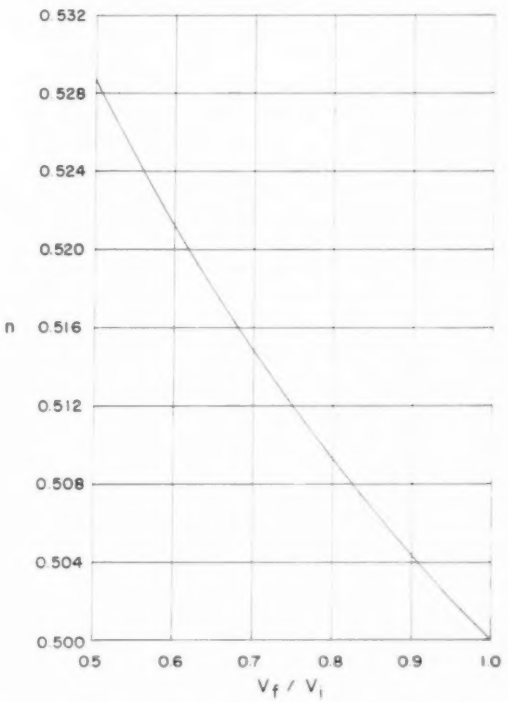

Fig. 1 Fraction of the distance interval at which $\bar{V} = V$.

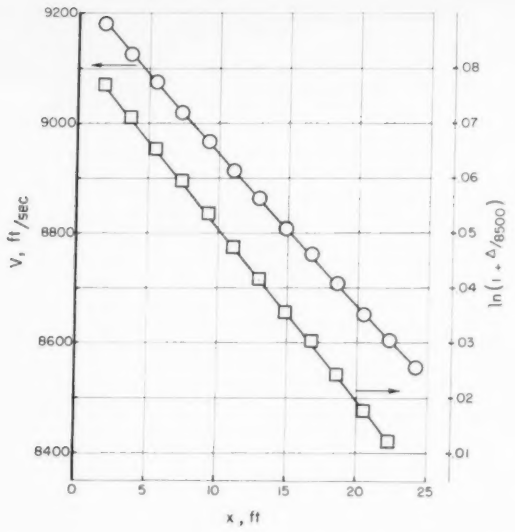

FIG 2. One set of data showing the variation of V and $ln\ [1 + (\Delta/V_r)]$ with x.

to the local velocity at the point nX where n is to be determined. (For constant deceleration, n would be equal to 1/2.)

$$\bar{V} = X/T = KC_DX/[(1/V_f) - (1/V_i)] = V_ie^{-KC_DnX} \quad (5)$$

Solving for n, we obtain

$$n = \frac{ln\{[V_i/V_f - 1]/ln(V_i/V_f)\}}{ln(V_i/V_f)} \quad (6)$$

which has been plotted in Fig. 1.

To compute a drag coefficient from range data, we would then proceed as follows. Choose a set of intervals of equal length, for which n is nearly constant, and plot V as a function of x, assuming n equals 1/2. (The effect of this assumption for equal intervals is primarily to translate the data along x.) Now, reading the velocity ratios from this curve, obtain the exact values of n and make the plot of $ln\ V$ against x to obtain the straight line whose slope equals $-KC_D$. An example is given in Fig. 2. Least-squares fitting of the data to the straight line may be easily accomplished when desired. Experience has shown that this method offers considerable advantage over those used earlier, particularly when the velocity variation in the range is large.

A final point concerns computative accuracy. Because $ln\ V$ changes very slowly with V when V is large, we express V in terms of a reference velocity and an increment

$$V = V_r + \Delta = [1 + (\Delta/V_r)]\,V_r$$

and note that the slope of the line $ln\ [1 + (\Delta/V_r)]$ versus x is the same as that of the line $ln\ V$ versus x.

$$ln\ V = ln\ [1 + (\Delta/V_r)] + ln\ V_r$$

$$d(ln\ V)/dx = d\{ln[1 + (\Delta/V_r)]\}/dx$$

Since Δ/V_r is small compared to 1, the logarithm of $1 + (\Delta/V_r)$ is sensitive to changes in Δ, and this fact is of some value in further improving the ease of calculation.

It has been called to our attention that a somewhat similar drag reduction procedure was applied in Germany around 1911 to the study of the drag of airships in coasting flight.[3] Time rather than distance was selected for the independent variable, and, by plotting $1/V$ as a function of time, a straight line was obtained. It can be readily demonstrated that such a presentation will give a straight line if C_D is constant. In reference 3, velocity and time were the measured quantities, so that the conversion of time-distance data and the calculation of the factor n were not required. Such a conversion could be made along the lines described herein if the velocity-time coordinates were for any reason preferred to velocity-distance coordinates.

REFERENCES

[1] Kelley, J. L., and McShane, E. J., *On the Motion of a Projectile with Small or Slowly Changing Yaw*, BRL Report No. 446, Aberdeen Proving Ground, Md., January 29, 1944.

[2] Seiff, Alvin, *A Free-Flight Wind Tunnel for Aerodynamic Testing at Hypersonic Speeds*, NACA Report 1222, 1955. (Supersedes NACA RM A52A24).

[3] Munk, Max M., *The Drag of Zeppelin Airships*. NACA Report 117, 1921.

On the Buckling Problem of Shallow Spherical Shells Under External Pressure*

H. J. Weinitschke
Department of Mathematics, Massachusetts Institute of Technology, Cambridge, Mass.
October 8, 1957

THE SUBJECT of the buckling of shallow spherical shells subjected to uniform normal pressure was recently considered in several papers. Two different interpretations of the apparent scattering in test data for the critical load q_c were given. In a paper by Klein,[1] it was suggested to attribute this scatter to initial irregularities of the specimen. On the other hand, it was attempted by Reiss[2] to interpret the scatter solely on the basis of sudden changes in the shape of the normal deflection of the shell. More precisely, it was observed that there is an oscillating behavior of the dimensionless buckling load $p_c(\mu^2) = q_c/Q_c$, where Q_c is the buckling pressure of the complete spherical shell as given by the linear theory and μ^2 is defined by Eq. (2), with sharp peaks at certain transition values, μ_k^2 ($k = 2, 3, \ldots$), to be defined below. The latter interpretation is supported by a recent theoretical investigation by Reiss, Greenberg, and Keller.[3] The purpose of this note is to present some results that differ from those obtained by previous approximate solutions and that tend to support the remarks in reference 1.

The differential equations for finite deflections of shallow spherical shells of uniform thickness h, if restricted to axisymmetrical modes of deformation, can be written in the following dimensionless form[4, 5]

$$\left.\begin{aligned} LF + \mu^2G - 2x + \gamma FG/x = 0 \\ LG - \mu^2F - \gamma F^2/2x = 0 \end{aligned}\right\} \quad 0 \le x \le 1 \quad (1)$$

where $LV = d[x^{-1}d(xV)/dx]/dx$, and x, F, and G/x are the dimensionless polar angle, angular deflection of the middle surface, and meridional stress resultant, respectively. The geometrical parameter μ^2 whose value is zero for a flat plate, and the load parameter γ, proportional to the external pressure q ($q > 0$ inward), are defined in terms of the radius of the middle surface a, the opening angle 2α, and the elastic constants E and ν as follows

$$\gamma = [12(1 - \nu^2)]^{3/2}\,a^4\alpha^4q/4Eh^4, \quad \mu^2 = [12(1 - \nu^2)]^{1/2}\,a\alpha^2/h \quad (2)$$

At the edge, the shell is assumed to be either simply supported (Case S) or clamped (Case C), which can be expressed in terms of F and G as follows:

$$F'(1) + \nu F(1) = G'(1) - \nu G(1) = 0 \quad \text{Case S} \quad (3)$$

$$F(1) = G'(1) - \nu G(1) = 0 \quad \text{Case C} \quad (3)$$

In both cases the conditions of symmetry require

* The present note is a report on work done under the sponsorship of the Office of Naval Research, carried out at the Computation Center of the Massachusetts Institute of Technology, and supported, in part, by the International Business Machines Corporation.

The writer wishes to express his appreciation to Professor Eric Reissner for his helpful advice and guidance during the course of the work.

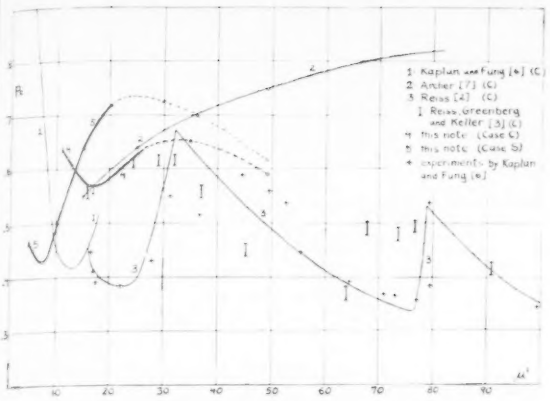
1 Kaplan and Fung [6] (C)
2 Archer [7] (C)
3 Reiss [2] (C)
4 Reiss, Greenberg and Keller [3] (C)
this note (Case C)
this note (Case S)
experiments by Kaplan and Fung [6]

FIG. 1. Dimensionless buckling loads $p_c(\mu^2)$.

$$F(0) = G(0) = 0 \tag{4}$$

Approximate solutions of this nonlinear boundary value problem were obtained in Case C by Kaplan and Fung[6] and by Archer[7] on the basis of perturbation methods. The "exact" solutions reported in this note have been obtained by assuming power series expansions for F and G, $F = \Sigma_1^{\infty} F_n x^n$, $G = \Sigma_1^{\infty} G_n x^n$. By applying an iterative technique[1] to suitably chosen initial approximations, it was possible to get solutions of a prescribed accuracy (0.01 per cent) for a wide range of the parameters γ and μ^2. The results are given in more detail elsewhere,[8] and the following discussion is restricted to the determination of the dimensionless buckling load p_c as a function of μ^2.

For small μ^2—i.e., $0 \leq \mu^2 \leq \mu_1^2$—the shell deforms similarly to a flat plate with a monotone increasing load deflection curve $q = q(W)$ (W = normal displacement of the middle surface at the apex $x = 0$). If μ^2 is in the interval $\mu_1^2 \leq \mu^2 \leq \mu_2^2$, the load deflection curve $q = q(W)$ possesses a relative maximum at $W = W_c$ and a relative minimum at $W = W_m > W_c$. According to the "classical" buckling criterion, the critical load is given by $q_c = q(W_c)$. More generally, we define the buckling load q_c as the largest load for which the boundary value problem constituted by Eqs. (1), (3), and (4) for fixed μ^2 has more than one solution. If μ^2 is in the interval $\mu_2^2 \leq \mu^2 \leq \mu_3^2$, the shape of the load deflection curve $q = q(W)$ is more complicated. Moreover, the normal deflection $w(x)$ changes its "mode," that is, the maximum of $w(x)$ does not occur at the apex, as is the case for $\mu^2 \leq \mu_2^2$.

For a limited range of μ^2—i.e., for $\mu^2 < 20$ in Case S and for $\mu^2 < 16$ in Case C—load deflection curves $q = q(W)$ were obtained also in the post-buckling region—i.e., for deflections $W > W_c$ and even for loads $q > q_c$. For $\mu^2 = 20$ (Case S) and $\mu^2 = 25$ (Case C), the results obtained for $q < q_c$ allow making a fairly accurate estimate of q_c by extrapolation. However, to determine q_c for larger values of μ^2—e.g., $\mu^2 = 49$, Case C—calculations must be carried out for values of γ of the order of magnitude 1000, which in the present method of solution would require retention of a number of terms in the power series that would exceed the capacity of the computer (Whirlwind-I). Dimensionless buckling loads $p_c = q_c/Q_c = \gamma_c/\mu^4$ obtained for $\mu^2 \leq 20$ (Case S) and for $\mu^2 \leq 25$ (Case C) are plotted against μ^2 in Fig. 1. The broken lines indicate the largest values $p = q/Q_c$, $p < p_c$, for which calculations have been successful by the present method for $\mu^2 > 25$, and which must therefore be considered as lower bounds for the actual values p_c. Note that some of the values given in reference 3 are considerably below these bounds.

Although further computations would be necessary to extend the curves $p_c(\mu^2)$ beyond $\mu^2 = 25$, the results show that the oscillatory behavior of $p_c(\mu^2)$ with maxima near $\mu^2 = \mu_k^2$ ($k \geq 1$) is certainly not as pronounced as is assumed in reference 2. It seems somewhat fortuitous that the peaking behavior due to the experimental scattering shows the same trend as the theoretical values p_c given in reference 3, which in turn appear to be, at least in part, a result of the failure of the computing process to converge to an expected solution.

REFERENCES

[1] Klein, B., *Further Remarks on the Collapse Pressures of Uniformly Loaded Spherical Shells*, Journal of the Aeronautical Sciences, Reader's Forum, Vol. 24, No. 4, p. 309, April, 1957.

[2] Reiss, E. L., *On the Nonlinear Buckling of Shallow Spherical Domes*, Journal of the Aeronautical Sciences, Reader's Forum, Vol. 23, No. 10, pp. 973–975, October, 1956.

[3] Reiss, E. L., Greenberg, H. J. and Keller, H. B., *Nonlinear Deflections of Shallow Spherical Shells*, Journal of the Aeronautical Sciences, Vol. 24, No. 7, pp. 533–543, July, 1957.

[4] Simons, R. M., *A Power Series Solution of the Non-linear Equations for Axisymmetrical Bending of Shallow Spherical Shells*, Journ. Math. Phys., Vol. 35, pp. 164–176, 1956.

[5] Reissner, E., *On Axisymmetrical Deformations of Thin Shells of Revolution*, Proc. of Sympos. in Appl. Math., Vol. 3, pp. 27–52, 1950.

[6] Kaplan, A., and Fung, Y. C., *A Non-linear Theory of Bending and Buckling of Thin Elastic Shallow Shells*, NACA, T.N. 3212, 1954.

[7] Archer, R. R., *The Post-Buckling Behavior of Shallow Spherical Shells*, Ph.D. Thesis in Mathematics, Massachusetts Institute of Technology, June, 1956.

[8] Weinitschke, H. J., *On the Non-linear Theory of Shallow Spherical Shells*, submitted to J. Soc. Indust. and Appl. Math.

Effect of Dissolution on Oleopneumatic Shock-Strut Performance*

Charles W. Bert
Principal Mechanical Engineer,
Battelle Memorial Institute, Columbus, Ohio

October 14, 1957

IN AN OLEOPNEUMATIC aircraft-landing-gear strut, damping is provided by forcing oil through an orifice, and springing is achieved by compressing a volume of air. There has been good agreement between pneumatic load-stroke performance predicted by simple air-compression theory and actual performance under rapid loading, such as experienced in landings and drop tests at high sinking speeds.[1] However, there has been a discrepancy between theory and experiment for static and slowly applied loading, such as found in gentle landings and taxiing.[2] An analysis which accounts for this discrepancy is presented here.

A useful relation between the instantaneous absolute pressure p and the corresponding density ρ of a constant mass of air in a cylinder is the familiar equation

$$p/\rho^n = \text{constant} \tag{1}$$

where n = polytropic-process exponent = unity for static loading. Walls[1] found that the dynamic value of n varied from 1.01 to 1.10.

It is well known that in a hydraulic oil system under pressure, a certain portion of any air present in the system becomes dissolved in the oil after a sufficient length of time. This phenomenon may be visualized physically by thinking of some of the air molecules being interspersed between the oil molecules. Because of the presence of air and oil in physical contact with each other in a shock strut, it is reasonable to expect dissolution to take place there also.

The dissolved air volume V_d is a function of pressure p, oil volume V_o, temperature, and time of exposure of the two fluids to each other. Campbell[3] presented the following expression for the saturation value of V_d, measured at standard temperature and pressure,

$$V_d = K V_o p \tag{2}$$

where K = a constant depending upon temperature.

In using Eq. (2), it is assumed that the oil contains all of the

* This problem was suggested by J. D. Stites, Fairchild Aircraft Division, Fairchild Engine and Airplane Corp., Hagerstown, Md.

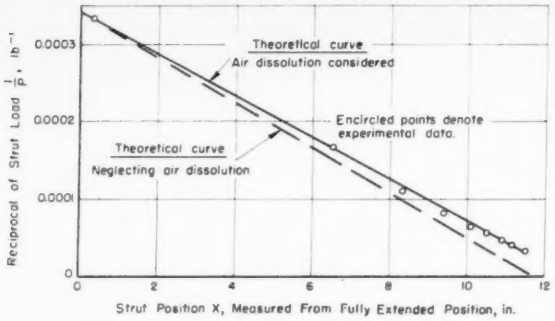

FIG. 1. Static load-stroke curve for a typical shock absorber.

air which can be dissolved at any particular pressure. Thus, the time lag between air compression and dissolution, or between air expansion and effervescence of the dissolved air, is assumed to be negligible. This is probably not valid for rapid loading, as shown by data obtained by Walls on air compression in which the total loading time was less than 0.25 sec. However, there are indications that dissolution may be taking place in some gentle drop tests,[2] and data to be presented later verify that this effect takes place in static loading.

The total mass m of air, including both gaseous and dissolved phases, in the cylinder is given by

$$m = \rho_s V_s + \rho_s V_{dn} = \rho_s (V_s + K V_o p_s) \tag{3}$$

where subscript s denotes quantities at standard conditions.

When the cylinder is under a pressure p, the density ρ of the air in the gaseous phase is

$$\rho = (m - \rho_s K V_o p)\ (1/V) \tag{4}$$

where V = air-space volume corresponding to pressure p.

After substituting the right-hand side of Eq. (3) for m in Eq. (4) and applying Eq. (1) with $n = 1$ to the air in the gaseous phase at pressures p and p_s, the following result is obtained:

$$pV = p_s[V_s - K V_o (p - p_s)] \tag{5}$$

The pressure p_{fe} and air-space volume V_{fe} at the fully extended strut position may be substituted into Eq. (5) to yield

$$V_s = V_{fe}\ (p_{fe}/p_s) + K V_o (p_{fe} - p_s) \tag{6}$$

Substitution of V_s from Eq. (6) into Eq. (5) gives

$$p = [(V_{fe} + K V_o p_s)/(V + K V_o p_s)]\, p_{fe} \tag{7}$$

Now, A = piston area, and x = any strut position, measured from fully extended position. Substitution of $(V_{fe} - Ax)$ for V and strut loads P and P_{fe} for pressures p and p_{fe} in Eq. (7) results in

$$P = [(V_{fe} + K V_o p_s)/(V_{fe} - Ax + K V_o p_s)]\, P_{fe} \tag{8}$$

Although Campbell gave 0.0073 psi^{-1} for K for saturation of air in oil, he gave no information on the time required for saturation or the effect of temperature. Therefore, the static value of K was determined during compression loading of a strut in a universal testing machine. Design data included: A = 10.31 sq.in., V_o = 167.3 cu.in., V_{fe} = 121.5 cu.in., P_{fe} = 2,940 lbs. Test results, plotted as the reciprocal of the load versus the stroke, are given by the encircled points in Fig. 1. It is to be noted that they fall very close to a straight line which differs significantly from simple air-compression theory. The straight line fitted through the data points was used in conjunction with the design parameters given above to determine the effective value of K in this test, 0.0038 psi^{-1}. Although considerable dissolution took place, the amount was less than Campbell's saturation value. This difference may have been due to a difference in the temperature of the tests.

REFERENCES

[1] Walls, James H., *Investigation of the Air-Compression Process During Drop Tests of an Oleo-Pneumatic Landing Gear*, NACA TN 2477, 1951.

[2] *German Landing Gear Design and Testing*, Aircraft Eng., Vol. 20, pp. 134–136, 150, May, 1948.

[3] Campbell, James E., *Investigation of the Fundamental Characteristics of High Performance Hydraulic Systems*, AF TR 5997, Air Materiel Command, Wright-Patterson AFB, June, 1950.

Analytical Results of Certain Nonlinear Flutter Problems

S. F. Shen* and C. C. Hsu**
Department of Aeronautical Engineering, University of Maryland, College Park, Md.
October 9, 1957

THE RECENT WORKS of Woolston et al.[1,2] reported on the behaviors of wing-control surface flutter systems with several kinds of structural nonlinearity as solved by an analogue computer. A number of interesting phenomena were noted such as the occurences of "limited amplitude flutter," "violent flutter," and "divergent flutter" depending upon the system and the amplitude of the motions. It is felt that apparently if the nonlinear flutter problem can be handled analytically, even in an approximate manner, much light will be shed on the roles of the various types of nonlinearity in producing the exhibited nonlinear effects.

We have applied the well-known theory of Kryloff and Bogoliuboff[3] in nonlinear mechanics to some of the flutter problems treated in references 1 and 2. Essentially, at flutter, a steady oscillation is assumed. The nonlinear element will generate higher harmonics in addition to the component of the fundamental frequency. By balancing the fundamental harmonic only, the problem is reduced to an equivalent linear one with certain elements depending on the amplitudes of motion as parameters. This is nothing but the simplified version of the "principle of harmonic linearization" of Kryloff and Bogoliuboff.

By such procedure, all the structural nonlinearities (except hysteresis) of references 1 and 2 are equivalent to linear stiffnesses which, however, vary with the amplitudes of motion. The flutter speed and frequency, therefore, can be directly determined on the basis of the usual linear analysis. The result naturally depends upon the amplitudes of motion. In the hysteresis case, the equivalent linear stiffness is complex—i.e., a certain amount of structural damping occurs. Again, both the real and imaginary parts vary with the amplitude.

* Professor of Aeronautical Engineering.
** Research Assistant.

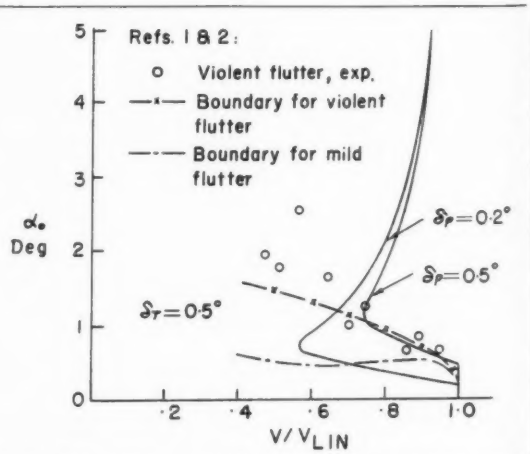

FIG. 1. Bending-torsion flutter with free play and preload in the torsional stiffness.

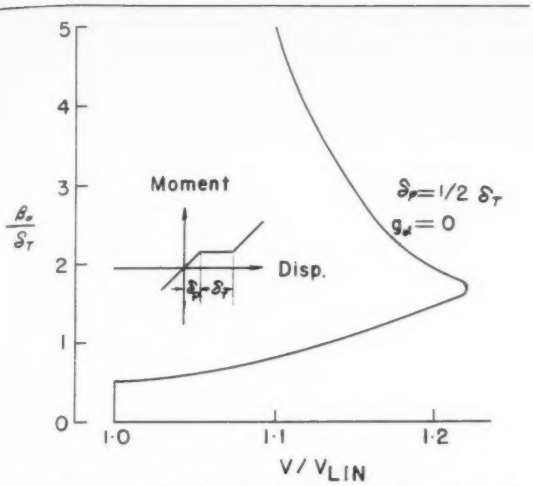

FIG. 2. Wing-control surface flutter with free play and preload in the aileron stiffness.

A few of the cases in references 1 and 2 are worked out by the present method in reference 4. The case of wing bending-torsion flutter with free play and preload in the torsional stiffness is shown as Fig. 1. The exact value of δ_p was not given in references 1 and 2. We have computed for $\delta_p = 0.2°$ and 0.5°; δ_T is kept at 0.5° as in the original references. The nonsymmetric stiffness property with regard to the direction of motion causes a steady deviation, effectively moving the neutral position during oscillation a small distance toward the "soft" side. It does not affect the flutter determination.

According to Fig. 1, our analysis indicates that for $V/V_{\text{Lin}} < 1.0$ the system is stable for small amplitudes but may assume very large amplitudes if the ratio is increased toward unity. Such behavior seems to agree with the description of references 1 and 2. However, the flutter boundary of Woolston et al. (Fig. 1 of reference 2) as superposed on Fig. 1 is seen to be rather different in character. We are quite certain that, as the amplitude increases much larger than the value δ_T, the system certainly should behave again as the linear one in the manner predicted by our analysis.

In Fig. 2 we show our results for the case of bending-torsion control surface flutter with free-play and preload in the control stiffness. The ratio of δ_p/δ_T again was not given in reference 2; our curve is for $\delta_p/\delta_T = 0.5$. The region to the left of the boundary is stable, to the right, unstable. For $1.2 > V/V_{\text{Lin}} > 1.0$, we see that the system is unstable for small amplitudes but will stabilize at an amplitude of $\beta_0/\delta_T < 2$; yet, by further increasing the amplitude, divergent motion occurs. Beyond $V/V_{\text{Lin}} \cong 1.2$, the system is unstable for all amplitudes. This prediction also agrees well qualitatively with the result of reference 2 (Fig. 6). Again the nature of the flutter boundary is quite different. To us, ours seems to be more convincing. In fact, it appears questionable whether the scale for β_0/δ_T of Fig. 6, reference 2, might not be erroneous. For β_0/δ_T of the order of 30, reference 2 indicated a much stronger nonlinear effect than our prediction for β_0/δ_T of the order of 5. To us, such a persistence of the nonlinear effect is rather difficult to accept.

In reference 4, the case (A) of Fig. 5, reference 2, was also examined. While qualitatively in agreement with our analysis, in this case at least, the numbers given by reference 2 must not be accepted without reservation. Even for $\beta_0/\delta_T = 0$, the value of V/V_{Lin} was given as approximately 1.75, in contrast to the value 1.46 directly obtainable from reference 5.

REFERENCES

[1] Woolston, D. S., Runyan, H. L., and Byrdsong, T. A., *Some Effects of System Nonlinearities in the Problem of Aircraft Flutter*, NACA TN 3539, 1955.

[2] Woolston, D. S., Runyan, H. L., and Andrews, R. E., *An Investigation of Effects of Certain Types of Structural Nonlinearities on Wing and Control Surface Flutter*, Journal of the Aeronautical Sciences, Vol. 24, No. 1, pp. 57–63, January, 1957.

[3] Kryloff, N., and Bogoliuboff, N., *Introduction to Non-linear Mechanics*, a free translation by S. Lefschetz, Princeton Univ. Press, Princeton, 1947.

[4] Hsu, C. C., *Analysis of Flutter Problems with Certain Types of Non-linearity*, M.S. Thesis, Dept. of Aero. Engrg., Univ. of Maryland, College Park, Md., 1957.

[5] Theodorsen, T., and Garrick, I. E., *Flutter Calculations in Three Degrees of Freedom*, NACA TR 741, 1942.

Stability Equations for Conical Shells*

Joseph Kempner

Professor of Aeronautical Engineering, Polytechnic Institute of Brooklyn, Brooklyn, N.Y.

October 9, 1957

ON P. 47 OF REFERENCE 1 Vlasov presents equations suitable for stability analyses of arbitrary thin-walled shells of constant thickness. For conical shells of circular cross section, these equations† become

$$D\nabla^4 w - (F_{,xx}/x)\cot\alpha - N^0{}_x w_{,xx} - N^0{}_\vartheta[(w_{,\vartheta\vartheta}/x^2\sin^2\alpha) + (w_{,x}/x)] - 2N^0{}_{x\vartheta}(w_{,\vartheta}/x\sin\alpha)_{,x} + Xw_{,x} + \Theta(w_{,\vartheta}/x\sin\alpha) = 0 \quad (1)$$

$$\nabla^4 F + (w_{,xx}/x)Eh\cot\alpha = 0 \quad (2)$$

Here w is taken as the component of the buckling displacement normal to the median surface and directed toward the axis of the cone whose apex angle is 2α and wall thickness is h; x is a coordinate measured from the apex along a generator of the median surface; and ϑ is an angular coordinate measured in planes normal to the axis (x, ϑ, and the inner normal form a right-handed coordinate system). $N^0{}_x$, $N^0{}_\vartheta$, and $N^0{}_{x\vartheta}$ are the membrane stress resultants prior to buckling (their sign convention corresponds to that of elasticity theory). X and Θ, respectively, are distributed surface loads fixed in the axial and circumferential directions (together with applied radial and edge loads which do not appear explicitly in Eqs. (1) and (2), they are considered in determining solutions of the membrane equations mentioned previously). $D = (1/12)Eh^3/(1-\nu^2)$, where E is Young's modulus and ν Poisson's ratio. The operator ∇^4 is defined as $\nabla^4 = \nabla^2\nabla^2$, where $\nabla^2(\ ) = (1/x)[x(\ )_{,x}]_{,x} + (1/x^2\sin^2\alpha)(\ )_{,\vartheta\vartheta}$ and the stress function F is related in the following manner to the increments in the stress resultants arising from the buckling displacements:

$$N_x = (F_{,\vartheta\vartheta}/x^2\sin^2\alpha) + (F_{,x}/x); \quad N_\vartheta = F_{,xx}; \quad N_{x\vartheta} = -(F_{,\vartheta}/x\sin\alpha)_{,x}$$

It can be readily shown that

$$(1/x^5)(x^4\nabla^4 F)_{,xx} = H(F_{,xx}) \quad (3)$$

in which H is an operator defined by

$$H(\ ) = (1/x)\nabla^4(\ ) + (8/x^2)(\ )_{,xxx} + (24/x^3)(\ )_{,xx} + (8/x^4)(\ )_{,x} + (8/x^4\sin^2\alpha)(\ )_{,x\vartheta\vartheta}$$

Eqs. (2) and (3) yield

$$H(F_{,xx}) = -(1/x^5)(x^3 w_{,xx})_{,xx} Eh\cot\alpha \quad (4)$$

and, therefore, from Eqs. (1) and (4)

* This work was performed under a consulting contract with the General Electric Company, Missile and Ordnance Systems Department, Philadelphia, Pa.

† After typographical errors on p. 47 of reference 1 are removed, the coefficients of the first quadratic form are taken as $A = 1$ and $B = x\sin\alpha$, and it is assumed that the stress system prior to buckling is governed by the well-known membrane equations for conical shells.

$$H\{x\nabla^4 w - (x/D)\{N^0_x w_{,xx} + N^0_\vartheta[(w_{,\vartheta\vartheta}/x^2 \sin^2\alpha) + (w_{,x}/x)] + 2N^0_{x\vartheta}(w_{,\vartheta}/x \sin\alpha)_{,x} - Xw_{,x} - \Theta(w_{,\vartheta}/x \sin\alpha)\}) + (Eh/D)\cot^2\alpha[(x^3 w_{,xx})_{,xx}/x^5] = 0 \quad (5)$$

This eighth-order equation in w can be considered to replace Eq. (1) which is coupled in w and F. An equation similar to Eq. (5) was derived by Seide in reference 2, but his equation differs from the present one in several terms in H. It is believed that this is simply due to an error made in the determination of a relation in reference 2 similar to Eq. (3).

At times, it is convenient to have the stability equations in terms of the buckling displacements. From pp. 32 and 47 of reference 1 it can be shown that the following two equations represent conditions for equilibrium of the membrane stress resultants arising during buckling.

$$v_{,x\vartheta} - [(3-\nu)/(1+\nu)](v_{,\vartheta}/x) = -[2/(1+\nu)]\{[x^3(u/x)_{,x}]_{,x}/x\} \sin\alpha - [(1-\nu)/(1+\nu)](u_{,\vartheta\vartheta}/x \sin\alpha) + [2/(1+\nu)][\nu w_{,x} - (w/x)]\cos\alpha \quad (6)$$

$$u_{,x\vartheta} + [(3-\nu)/(1+\nu)](u_{,\vartheta}/x) = -[2/(1+\nu)][(v_{,\vartheta\vartheta}/x \sin\alpha) - [(1-\nu)/(1+\nu)]\{[x^3(v/x)_{,x}]_{,x}/x\} \sin\alpha + [2/(1+\nu)](w_{,\vartheta}/x)\cot\alpha \quad (7)$$

in which u and v, respectively, are median-surface buckling displacements in the x and ϑ directions. Eq. (1) represents a third equation in the buckling displacements since

$$F_{,xx} = N_\vartheta = [Eh/(1-\nu^2)][(1/x \sin\alpha)(v_{,\vartheta} + u \sin\alpha - w\cos\alpha) + \nu u_{,x}]$$

in accordance with reference 1.

If it is assumed that

$$u_{,x} >> (u/x) = (\tan\alpha/r)u, \quad v_{,x} >> (v/x) = (\tan\alpha/r)v \quad (8)$$

where r is that principal radius of curvature of the median surface which lies in a plane normal to a generator, Eqs. (6) and (7) can be readily transformed into more convenient expressions. The assumptions made in Eqs. (8) are certainly reasonable for thin-walled, truncated cones of small apex angle (see reference 3); furthermore, as $\alpha \to (\pi/2)$ the cone approaches a flat circular plate and only Eq. (1) (which becomes independent of F and, hence, of u and v) is required.

If Eqs. (8) are applied, Eqs. (6) and (7) reduce to

$$v_{,x\vartheta} = -[2/(1+\nu)](x \sin\alpha\, u_{,x})_{,x} - [(1-\nu)/(1+\nu)] \times (u_{,\vartheta\vartheta}/x \sin\alpha) + [2/(1+\nu)][\nu w_{,x} - (w/x)]\cos\alpha \quad (9)$$

$$u_{,x\vartheta} = -[2/(1+\nu)](v_{,\vartheta\vartheta}/x \sin\alpha) - [(1-\nu)/(1+\nu)](x \sin\alpha\, v_{,x})_{,x} + [2/(1+\nu)](w_{,\vartheta}/x)\cot\alpha \quad (10)$$

With a procedure analogous to that given in reference 3, these equations transform into

$$H_1(v) = \cos\alpha\{(2+\nu)x(xw_{,x\vartheta})_{,x}\sin^2\alpha + w_{,\vartheta\vartheta\vartheta} + [(1+\nu)/(1-\nu)]xw_{,x\vartheta}\sin^2\alpha\} \quad (11)$$

$$H_1(u) = \cos\alpha \sin\alpha\{\nu x[x(xw_{,x})_{,x}]_{,x}\sin^2\alpha - xw_{,x\vartheta\vartheta} - x(xw_{,x})_{,x}\sin^2\alpha - [2/(1-\nu)]w_{,\vartheta\vartheta}\} \quad (12)$$

in which H_1 is an operator defined by

$$H_1(\ ) = x(x\{x[x(\ )_{,x}]_{,x}\}_{,x})_{,x}\sin^4\alpha + 2x[x(\ )_{,x\vartheta\vartheta}]_{,x}\sin^2\alpha + (\ )_{,\vartheta\vartheta\vartheta\vartheta}$$

(see reference 3). Except for the existence of the last term within the braces in Eq. (11) and the last two terms within the braces of Eq. (12), these equations are the same as the corresponding equations of reference 3.

Expressions relating membrane, bending, twisting, and transverse shear stress resultants to the displacements u, v, and w can readily be obtained from pp. 27, 28, and 32 of reference 1. These relations (together with Eqs. (8) if Eqs. (11) and (12) are used) must be considered when boundary conditions are enforced.

Eq. (11) which relates v and w, and Eq. (12) relating u and w, together with Eq. (5), represent equations alternative to those formulated previously in terms of w and F. Of course, Eqs. (11) and (12) depend upon the suitability of the assumptions represented by Eqs. (8), while Eq. (5) remains as originally derived. Inasmuch as experience with buckling problems of circular cylinders indicates that u and v play a minor role compared to that of w, it is believed that little accuracy is sacrificed if Eqs. (11) and (12) are employed.

References

[1] Vlasov, V. S., *Basic Differential Equations in General Theory of Elastic Shells*, NACA TM 1241, February, 1951.

[2] Seide, Paul, *A Donnell-Type Theory for Asymmetrical Bending and Buckling of Thin Conical Shells*, Guided Missile Research Division, The Ramo-Wooldridge Corp., Report No. GM-TM-103, July 13, 1956. (Also J. Appl. Mech. Paper No. 57-APM-42).

[3] Hoff, N. J., *Thin Circular Conical Shells Under Arbitrary Loads*, J. Appl. Mech., Vol. 22, No. 4, pp. 557–562, December, 1955.

Some Remarks on the Foundations of Piston Theory and Supersonic-Hypersonic Similarity*

G. A. Bird
Aerodynamics Division, Weapons Research Establishment, Salisbury, South Australia
October 14, 1957

HAYES[1] SHOWED THAT when the velocity changes in the free-stream direction are small in comparison with those in the transverse directions the equations of motion of steady compressible flow approximate those of unsteady flow having one less dimension. Considering the hypersonic flow past a two-dimensional airfoil, the above condition is nearly satisfied and the flow pattern becomes analogous with that produced by a piston in the distance-time plane. The nondimensional piston velocity corresponding to a given flow deflection angle (δ) and free-stream Mach Number (M) is $M \tan\delta$ (or $M\tau$) which is the similarity parameter proposed by Hayes and, prior to him, by Tsien.[2]

However, the approximation made by Hayes can be avoided in some cases since the equations of motion of two-dimensional steady flow reduce to those of one-dimensional unsteady flow if the velocity component in *any* direction remains constant throughout the flow field. When such a direction exists, the equivalent piston velocity is in a direction normal to it and of magnitude such that the body boundary condition is satisfied. The nondimensional piston velocity which is the ratio of the piston velocity to the speed of sound in the undisturbed gas then serves as a similarity parameter for the steady flow.

In the case of the basic two-dimensional flows (oblique shock waves and Prandtl-Meyer expansions) which consist essentially of two regions of uniform flow separated by a transition region, a direction in which the velocity component is unchanged does exist outside the transition region and in the oblique shock case it is, of course, the direction of the shock front. It should therefore be possible to find for these flows an exact similarity parameter which holds for low as well as high supersonic speeds and for large as well as small deflection angles.

Considering first oblique shock waves (Fig. 1) with the axes as shown, the flow is analogous to the flow in the (x, t) plane which would be produced by a piston moving with uniform velocity along the line AB. The boundary condition is satisfied if the ratio of the piston velocity (U) to the free-stream flow veloc-

* Acknowledgment is made to the Chief Scientist, Department of Supply, Australia, for permission to publish this article.

ity (q) is made equal to the ratio of the length of AB to that of OA in Fig. 1—i.e.,

$$U/q = AB/OA = (U/a)/M$$

Therefore

$$U/a = M \sin \delta/\cos (\alpha - \delta) \qquad (1)$$

where a is the speed of sound in the undisturbed gas and α is the direction in which the flow velocity remains constant.

For Prandtl-Meyer expansions (Fig. 2), if the convention is adopted that angles are positive when measured counterclockwise from the free-stream direction, it is found that the nondimensional piston velocity is again given by Eq. 1.

Hence for both cases the exact similarity law becomes

$$p/p_1 = f_1[M \sin \delta/\cos (\alpha - \delta)]$$

Unfortunately, α cannot be simply expressed as an explicit function of M and δ for either of the flows. However, the angle of inclination of an oblique shock wave to the body surface is very nearly equal to the free-stream Mach angle (μ), so that the replacement of $\alpha - \delta$ by μ is a good approximation for oblique shock waves. Fortunately, it is also a reasonable approximation for Prandtl-Meyer expansions. The similarity parameter then becomes,

$$p/p_1 = f_2(M \sin \delta/\cos \mu) = f_2(M^2 \sin \delta/\sqrt{M^2 - 1})$$

or in terms of thickness-chord ratio and Mach Number,

$$p/p_1 = f_2(M^2\tau/\sqrt{M^2 - 1}\sqrt{\tau^2 + 1})$$

It has been shown[3] that the replacement of M by $M^2/\sqrt{M^2 - 1}$ in the conventional hypersonic parameter M tan δ increases the accuracy at low supersonic Mach Numbers and the use of sin δ instead of tan δ greatly increases the accuracy at large deflection angles.

Piston theory may also be applied to axisymmetric flows and the flow over a cone becomes analogous with the flow produced by a uniformly expanding cylindrical piston. However, the shock wave produced by a cone does not separate two regions of constant flow velocity and direction, and there is no direction in which the velocity component is unchanged, so that an exact similarity parameter does not follow. The direction of the surface of the cone is found to be the closest simple approximation to such a direction, and, when the expanding cylinder analogy is applied in this direction, the similarity parameter M sin δ is obtained.

Van Dyke[4] has proposed the similarity parameter $C_p = \tau^2 f_3 \times (\tau\sqrt{M^2 - 1})$ as a combined supersonic-hypersonic rule. He noted that $p/p_0 = f_4(M^2\tau/\sqrt{M^2 - 1})$ had also been proposed as a combined similarity parameter and states that it is restricted to planar systems. Further, he remarked that hypersonic and combined similarity rules apply to rather thick bodies if τ is taken to be the sine of the maximum angle of inclination of the body surface. This note gives a simple explanation in terms of piston theory of both these observations.

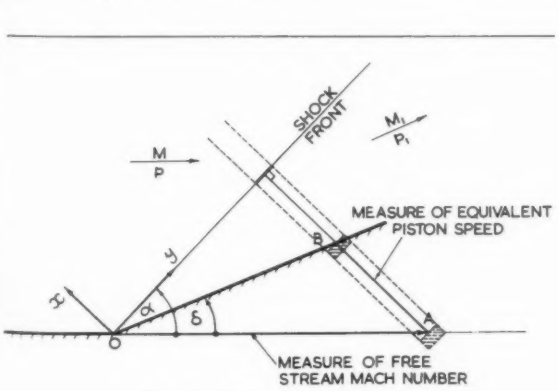

FIG. 1. Oblique shock wave.

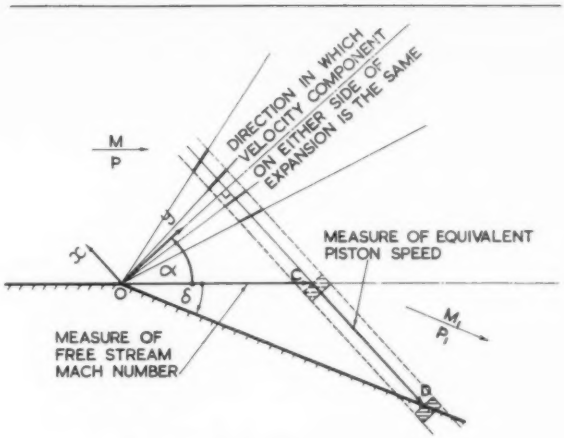

FIG. 2. Prandtl-Meyer expansion.

REFERENCES

[1] Hayes, W. D., *On Hypersonic Similitude*, Quart. Appl. Math., Vol. 5, No. 1, pp. 105, 106, April, 1947.

[2] Tsien, H. S., *Similarity Laws of Hypersonic Flows*, J. Math. & Phys., Vol. 25, No. 3, pp. 247–251, October, 1946.

[3] Bird, G. A., *A New Approach to Supersonic-Hypersonic Similarity*, Weapons Research Establishment, High Speed Aerodynamics, TN 32, April, 1957.

[4] Van Dyke, M. D., *The Combined Supersonic-Hypersonic Similarity Rule*, Journal of the Aeronautical Sciences, Vol. 18, No. 7, pp. 499, 500, July, 1951.

On the Eigenvector Direction of Turboblading with Lashing Wire

Milomir M. Stanišić
Associate Professor of Engineering Sciences, Purdue University, Lafayette, Ind.

October 14, 1957

SUMMARY

The variational principle of strain energy is used in order to determine, when the turbine is at rest, the direction of the eigenvector in which a group of blades with constant cross section and twisted along their length vibrate in the fundamental bending mode when they are tied together with one lashing wire. Investigation shows that in the case of one connection the eigenvector direction almost coincides with the direction of the axis of maximum moment of inertia.

DISCUSSION

AN IMPORTANT PART concerning the blading problems in turbodesign belongs to the determination of the angle in which vibration of a group of blades occurs when the turbine is either at rest or in motion. Such an angle is called the vibration angle, β, and is measured with respect to the major axis of inertia. In the literature, the investigation of this problem is due to the work of Geiger[1] and Stanišić.[2, 3] Mathematical interpretation of this problem implies two separate coordinate systems, namely, Ogx and Okx, with O at the intersection of the principal axis. From this, g-g and k-k are axes of maximum and minimum moment of inertia, respectively; y-y, direction of the blade perimeter; z-z, direction of the turbine axis, and x-x, direction of the blade axis; α, angle of twist; and ϑ, angle between plane of load and g-g axis. For all other symbols see Figs. 1, 2, and 3.

Assume that the actual angle of vibration of blade at rest coincides with that generated when the blade carries a uniform load P in addition to a single load Q acting at the place where the lashing wire is hard-soldered to the blade. Then, the strain energy of the system under consideration is:

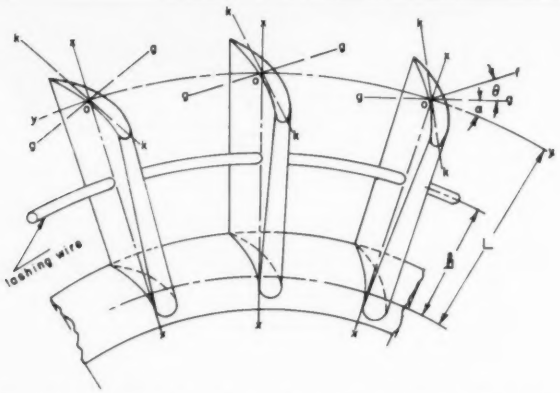

FIG. 1. Group of the blades interconnected with lashing wire.

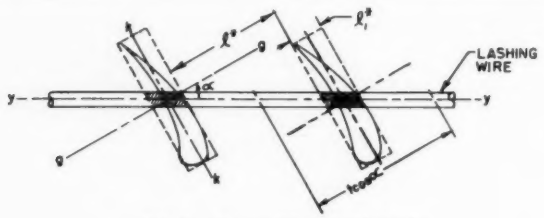

FIG. 2. Geometry of lashing wire.

$$A(\vartheta) = A_g + A_k + A_B \tag{1}$$

where

$$A_g = (EI_g/2)\left[\int_0^{l_1} g_{1,\,xx}{}^2(x,\vartheta)dx + \int_{l_1}^{L} g_{2,\,xx}{}^2(x,\vartheta)dx\right] \tag{2}$$

$$A_k = (EI_k/2)\left[\int_0^{l_1} k_{1,\,xx}{}^2(x,\vartheta)dx + \int_{l_1}^{L} k_{2,\,xx}{}^2(x,\vartheta)dx\right] \tag{3}$$

are the strain energies of the blade corresponding to the bending about g-g and k-k axes, $g_i(x,\vartheta)$, $k_i(x,\vartheta)$ are the corresponding deflections with respect to each axis, index 1, 2 refer to the domains $0 \le x \le l_1$, $l_1 \le x \le L$ as shown in Fig. 1. And

$$A_B = M_B k_{1,\,x}(l_1,\vartheta) \tag{4}$$

is strain energy introduced by the bending moment transferred to each blade by the lashing wires on both sides. Note that $\mu = Q/P$.

Then, using ordinary flexural theory one obtains for $0 \le x \le l_1$

$$g_1(x,\vartheta) = (x^2/2EI_g)P\{(L/12)[6 - 4(x/L) + (x/L)^2] + \mu[l_1 - (x/3)]\}\sin\vartheta \tag{5}$$

$$k_1(x,\vartheta) = (x^2/2EI_k)\big(P\{(L/12)[6 - 4(x/L) + (x/L)^2] + \mu[l_1 - (x/3)]\}\cos\vartheta - 2M_B\big) \tag{6}$$

and for $l_1 \le x \le L$:

$$g_2(x,\vartheta) = (x^2/2EI_g)P\{(L/12)[6 - 4(x/L) + (x/L)^2] + \mu(l_1/x)^2[x - (l_1/3)]\}\sin\vartheta \tag{7}$$

$$k_2(x,\vartheta) = (x^2/2EI_k)\big(P\{(L/12)[6 - 4(x/L) + (x/L)^2] + \mu(l_1/x)^2[x - (l_1/3)]\}\cos\vartheta - 2M_B\big) \tag{8}$$

From Figs. 2 and 3 it follows that

$$k_{1,\,x}(l_1,\vartheta) = 2(f_1 + f_2)/t\cos\alpha \tag{9}$$

Evidently

$$f_1 = M_B l^{*3}/12tEI_B \tag{10}$$

$$f_2 = (1/2)t\sin\alpha g_{1,\,x}(l_1,\vartheta) \tag{11}$$

From Eqs. (6), (9), (10), and (11) it follows that

$$M_B = \Lambda[(I_B/I_k)\cos\vartheta\cos\alpha - (I_B/I_g)\sin\vartheta\sin\alpha] \tag{12}$$

where

$$\Lambda = \frac{3LP[1 + (l_1/L)(\mu - 1) + (1/3)(l_1/L)^2]}{(l^{*3}/l_1t^2) + 12(I_B/I_k)\cos\alpha} \tag{13}$$

Hence, Eq. (1) can now be evaluated. It follows that

$$A(\vartheta) = R_1\sin^2\vartheta + R_2\cos^2\vartheta + R_3\sin 2\vartheta \tag{14}$$

where

$$R_1 = (L^3P^2/8EI_g)\{(1/5) + (l_1/L)^2[2 - (4/3)(l_1/L) + (1/3)(l_1/L)^2]\mu + (4/3)(l_1/L)^3\mu^2\} \tag{15}$$

$$R_2 = (L^3P^2/8EI_k)\{(1/5) + (l_1/L)^2[2 - (4/3)(l_1/L) + (1/3)(l_1/L)^2]\mu + (4/3)(l_1/L)^3\mu^2\} - (P\Lambda L/2EI_k)\times (I_B/I_k)\{l_1[1 + (l_1/L)(\mu - 1) + (1/3)(l_1/L)^2] - (2/3)L[1 + 3\mu(l_1/L)^2]\}\cos\alpha \tag{16}$$

$$R_3 = (P\Lambda L/2EI_k)(I_B/I_g)\{(1/3)L[1 + 3\mu(l_1/L)^2] - (1/2)l_1[1 + (l_1/L)(\mu - 1) + (1/3)(l_1/L)^2]\}\sin\alpha \tag{17}$$

Note $f(x,\vartheta)$ resulting deflection of the blade, then

$$f^2(L,\vartheta) = g_2{}^2(L,\vartheta) + k_2{}^2(L,\vartheta) \tag{18}$$

or

$$f^2(L,\vartheta) = U_1\sin^2\vartheta + U_2\cos^2\vartheta + U_3\sin 2\vartheta \tag{19}$$

where

$$U_1 = (L^3P\epsilon/2EI_g)^2 + (L^2\Lambda/EI_k)^2(I_B/I_g)^2\sin^2\alpha \tag{20}$$

$$U_2 = (L^3P\epsilon/2EI_k)^2 + (L^2\Lambda/EI_k)^2(I_B/I_k)^2\cos^2\alpha - [L^5P\Lambda\epsilon/(EI_k)^2](I_B/I_k)\cos\alpha \tag{21}$$

$$U_3 = (1/2)\{[L^5P\Lambda\epsilon/(EI_k)^2](I_B/I_g)\sin\alpha - (l^2\Lambda/EI_k)^2(I_B{}^2/I_gI_k)\sin 2\alpha\} \tag{22}$$

$$\epsilon = (1/4) + \mu(l_1/L)^2[1 - (1/3)(l_1/L)]$$

Now the strain energy per unit deflection can be obtained. The necessary condition from which the deflection angle ϑ can be obtained follows from the variational principle of the strain energy per unit deflection in the system—i.e.,

$$A(\vartheta)/f^2(L,\vartheta) = \text{Minimum} \tag{23}$$

or

$$A_\vartheta(\vartheta)f^2(L,\vartheta) - f_\vartheta{}^2(L,\vartheta)A(\vartheta) = 0 \tag{24}$$

Eqs. (14), (19), and (24) lead to

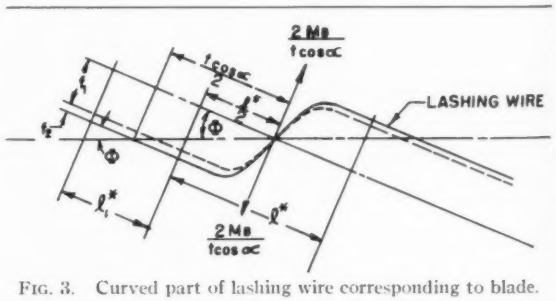

FIG. 3. Curved part of lashing wire corresponding to blade.

TABLE 1

Geometrical Characteristics of Turboblades for Driving the Compressors J-33, J-35, and J-40

	L (in.)	l_1 (in.)	t (in.)	l^* (in.)	F (in.²)	F_B (in.²)	I_g (in.⁴)	I_k (in.⁴)	I_B (in.⁴)	α (°)	ϑ (rad.)	β (rad.)
J-33	4.00	2.66	1.12	0.80	0.279	0.020	$10^{-6}\times 87210$	$10^{-6}\times 482$	$10^{-6}\times 30$	25°20′	0.00198	0.00
J-35	3.50	2.33	0.58	0.29	0.197	0.020	$10^{-6}\times 28230$	$10^{-6}\times 369$	$10^{-6}\times 30$	20°	0.00442	0.00
J-40	3.62	2.42	0.62	0.22	0.138	0.020	$10^{-6}\times 16216$	$10^{-6}\times 162$	$10^{-6}\times 30$	40°35′	0.00825	0.00

$$2\tau_1 \sin 2\vartheta + (\tau_2 + \tau_3)\cos 2\vartheta + (\tau_3 - \tau_2) = 0 \quad (25)$$

where $\tau_1 = U_2R_1 - U_1R_2$, $\tau_2 = 2(U_1R_3 - U_3R_1)$, $\tau_3 = 2(U_2R_3 - U_3R_2)$. From Eq. (25) it follows that

$$\vartheta = \sin^{-1}\left\{\frac{2[(\tau_2 + \tau_3)\sqrt{\tau_1^2 + \tau_2\tau_3 + \tau_1(\tau_2 - \tau_3)}]}{4\tau_1^2 + (\tau_2 + \tau_3)^2}\right\} \quad (26)$$

But at the end of the blade, the following relation exists:

$$f(L, \vartheta) = g_2(L, \vartheta)\sin\beta + k_2(L, \vartheta)\cos\beta \quad (27)$$

Then, the vibration angle is given by

$$\beta = \sin^{-1}[g_2(L, \vartheta)/f(L, \vartheta)] \quad (28)$$

Table 1 shows the results obtained for turboblades for driving the compressors J-33, J-35, and J-40, at the laboratory of the School of Aeronautical Engineering at Purdue University. The results show that in the case of one connection the eigenvector direction almost coincides with the direction of the axis of maximum moment of inertia.

References

[1] Geiger, J., *Über Schwingungen von Turbinenschaufeln*, Schiff u. Werft, Vol. 44, No. 24, p. 49–58, 217–224, 1943.

[2] Stanišić, M. M., *Beitrag zur Bestimmung der Schwingungsrichtung bei ruhenden Dampfturbinenschaufeln mit Deckband*, Forschung Gebiete Ing., Ausg. A., Vol. 20, No. 4, p. 108, 1954.

[3] Stanišić, M. M., *Über die Schwingungsrichtung bei umlaufenden Dampfturbinenschaufeln mit Deckband*, Forschung Gebiete Ing., Ausg. A., Vol. 21, No. 6, p. 189, 1955.

Concerning the Rigidity of Elastic Structures

M. Zaid

Scientific Research Staff, Republic Aviation Corporation, Farmingdale, N.Y.

September 16, 1957

IT IS THE PURPOSE of this note to state and examine some limitations of a theorem often used intuitively by the stress and vibration analyst. This theorem can be expressed as follows.

Adding material to any traction-free subsurface of a complex elastic structure which is acted upon by a system of external forces results in a decrease in the deflection under each load, and vice versa. This theorem is often used intuitively when the design engineer "beefs up" a structure to make it more rigid.

Biezeno and Grammel[1] have introduced the above as an auxiliary principle necessary for the deduction of Saint-Venant's Principle. However, instead of the actual displacement, they use an "average" displacement which is not clearly defined. The theoretical development leading to inequality (5) of this note is different from their physical reasoning and in addition deals explicitly with the actual deformation and stress fields.

Let us consider a general structure (structure 1) as shown in Fig. 1, excluding region A having external tractions T_i^*. The associated internal stresses and strains are given by σ_{ij}^* and ϵ_{ij}^*. Further let us consider a second structure (structure 2) which is identical to that indicated above but in addition has material added to some traction-free surface of structure 1 (say region A). The tractions, stresses, and strains in this second structure are designated by T_i^*, σ_{ij}, and ϵ_{ij}, respectively.

Let us consider fictitious stress and strain fields σ_{ij}^{**} and ϵ_{ij}^{**} in structure 2, made up as follows:

$$\left.\begin{aligned}\sigma_{ij}^{**} &= \sigma_{ij}^*\\ \epsilon_{ij}^{**} &= \epsilon_{ij}^*\end{aligned}\right\} \text{in the region circumscribed by structure 1} \quad (1)$$

$$\left.\begin{aligned}\sigma_{ij}^{**} &= 0\\ \epsilon_{ij}^{**} &= 0\end{aligned}\right\} \text{in region A} \quad (2)$$

It can be easily shown that σ_{ij}^{**} is in equilibrium throughout the body, even across the traction-free subsurface S. ϵ_{ij}^{**} satisfies Hooke's law everywhere but will in general violate the conditions of compatibility.

Subject to the above conditions there results,[2]

$$\int_2 \sigma_{ij}^{**}\epsilon_{ij}^{**}dv - \int_2 \sigma_{ij}\epsilon_{ij}dv \geq 0 \quad (3)$$

where the integration is over structure 2.

This is valid even for the discontinuous stress and strain distribution σ_{ij}^{**} and ϵ_{ij}^{**}, the only requirement on continuity being that equilibrium is satisfied over the entire volume.

Introducing the stress and strain distributions—Eqs. (1) and (2)—inequality (3) becomes,

$$\int_1 \sigma_{ij}^*\epsilon_{ij}^*dv - \int_2 \sigma_{ij}\epsilon_{ij}dv \geq 0 \quad (4)$$

This inequality furnishes a comparison of the total internal energies of structures 1 and 2.

Since the stresses and strains in inequality (4) are the actual values associated with the corresponding structures, they satisfy equilibrium and compatibility. Hence, applying the theorem of virtual work there results,

$$\int_s T_i^*(u_i^* - u_i)dS \geq 0 \quad (5)$$

where u_i^* and u_i are the associated generalized displacements in the direction of the external tractions T_i^*.

The following general results can be deduced directly from inequality (5) without further calculation:

1. For the system with a single concentrated generalized load, adding material decreases the associated deformation under that load, and vice versa. Stated differently, the system becomes stiffer when material is added.

2. For the system with a distributed external traction that is either zero or constant everywhere else, the average deformation over the loaded area in the direction of the traction ($\int_S u_i dS/S$) decreases with an increase of material.

The results given in 1. above cannot be generalized to hold for an arbitrary variable traction or combination of concentrated tractions. To illustrate the impossibility of such a generalization, examples and counterexamples will be shown for some simple structures. As a result of this conclusion, each complex loading or class of loading will have to be investigated as a special case for the particular class of structures under consideration.

Fig. 2, illustrates a simple support beam with all external loads in the same direction. It is apparent that increasing material on a traction-free surface will decrease the deformation under each load.

Fig. 3 illustrates a clamped beam with a slot parallel to the neutral axis. Increasing the slot length L is equivalent to removing material, and, decreasing L is equivalent to adding material. For the case of $P_1 \gg P_2$, there exists a slot length L such

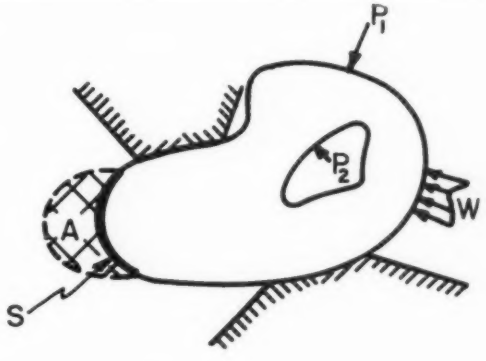

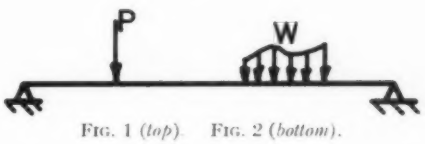

FIG. 1 (*top*). FIG. 2 (*bottom*).

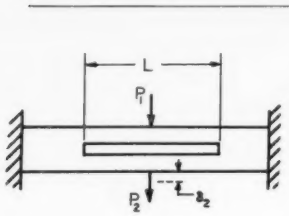

FIG. 3

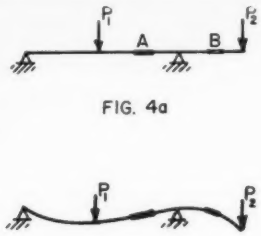

FIG. 4a

FIG. 4b

that increasing L will decrease δ_2, and conversely, decreasing L will increase δ_2. Thus even though removal of material will increase the total work it will not increase all deflections in this case.

Fig. 4a illustrates a structure that furnishes both an example and counterexample. For the proper ratio of P_1/P_2 and rigidities on each side of the right hand support, the deflections can both be made positive as shown in Fig. 4b. Increasing the rigidity in region B has the effect of decreasing δ_2 without affecting δ_1. Increasing the rigidity in region A has the effect of increasing δ_2 while decreasing δ_1.

References

[1] Biezeno, C. B., and Grammel, R., *Engineering Dynamics*, Vol. I, p. 104; Blackie and Son Limited, London, 1955.

[2] Hill, R., *Plasticity*, p. 61; Oxford at the Clarendon Press, 1950.

The Effect of Internal Pressure on the Buckling Stress of Thin-Walled Circular Cylinders Under Combined Axial Compression and Torsion†

Leonard A. Harris*, Herbert S. Suer*, and William T. Skene**
Missile Development Division, North American Aviation, Inc., Downey, Calif.

October 17, 1957

MODERN AIRCRAFT and missiles often incorporate pressurized circular, cylindrical, monocoque fuel or instrument compartments in their fuselage structures. Even though these compartments may not be pressurized for structural purposes, systems requirements often dictate the use of internal pressure. If internal pressure is present, it behooves the structures engineer to account for the increased stability of the shell (and the subsequent increase in the strength-weight ratio) caused by pressurization. Although previous investigations have been made of pressurized cylinders loaded in axial compression alone[1,2,3] or in torsion alone,[4,5] no information has been published on the stability of pressurized cylinders under combined axial compression and torsion.

For circular cylinders which are not internally pressurized, an empirical interaction curve for combined compression and torsion has been suggested[6] in the form

$$R_c + R_t^2 = 1 \qquad (1)$$

where

R_c = critical compressive stress under combined load divided by critical compressive stress under compression alone

R_t = critical shear stress under combined load divided by critical shear stress under torsion alone

The theoretically derived interaction curve obtained by solving Donnell's equation is almost a straight line[6] and has been found to be too conservative when compared with test results. As a consequence, the empirical curve is generally accepted provided the values used for pure compression and pure torsion in the stress ratios are determined from empirically defined design curves or from tests.

For pressurized cylinders under combined compression and torsion, a theoretical interaction curve cannot be derived from Donnell's equation because small deflection theory does not indicate the stabilizing effect of internal pressure on the compressive buckling stress. To further complicate the problem, no experimental data for pressurized cylinders under combined loads have been available in the literature to date. It is the purpose of the present note to show that the shape of the empirically defined interaction design curve given by Eq. (1) is valid for pressurized circular cylinders under combined compression and torsion.

To obtain test data on the buckling of pressurized cylinders under combined loads, a series of tests of circular cylinders was performed in the Structural Test Laboratory of the Missile Development Division. A total of 28 pressurized cylinders were tested, 10 in axial compression, 6 in torsion, and 12 in combined axial compression and torsion. The test cylinders were fabricated from 0.0032-, and 0.0087-in.-thick, half-hard, 18–8 stainless steel. The cylinders were prepared with a length of 21.5 in., a radius of 8.75 in., and had r/t ratios of approximately 1,000 and 2,730. The cylinders were internally pressurized to 8.4 psi. Most of the cylinders were fabricated by wrapping the sheet and adhesive bonding a single 3/8 in. wide longitudinal seam with Epon VI adhesive. Some of the later cylinders were fabricated by seam welding which proved to be a faster and simpler technique.

The test cylinders were clamped by straps to the 3-in.-thick circular aluminum head plates of the test jig (see Fig. 1 of reference 3). The straps prevented slippage and leakage between the heads and the cylinder. Internal pressure was pneumatically

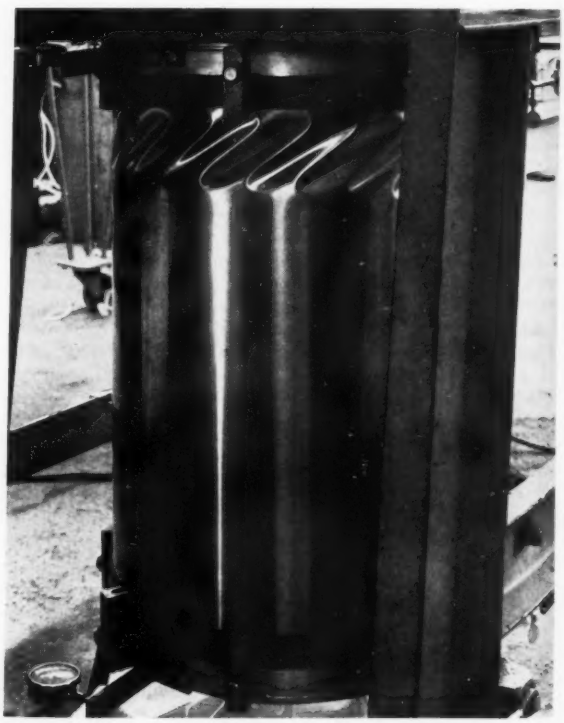

FIG. 1. Typical buckle pattern for pressurized cylinders under combined loads.

† The authors gratefully acknowledge the assistance of the personnel of the Structural Test Laboratory of the Missile Development Division who conducted the test program.

* Senior Structures Engineer.

** Group Leader, Structures Data and Methods.

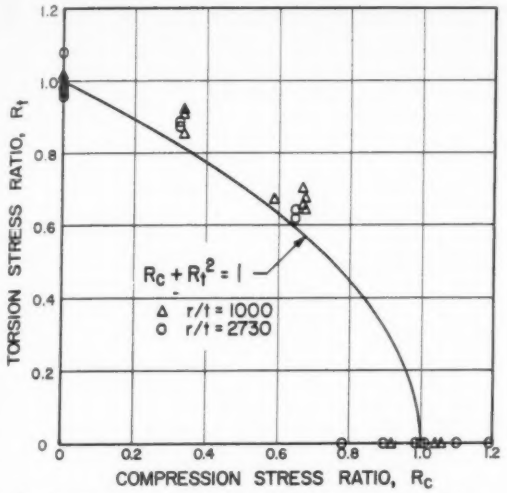

FIG. 2. Interaction curve for pressurized cylinders under combined compression and torsion.

supplied, but, for reasons of safety the cylinders were partially filled with water. A mercury manometer was used to measure the internal pressure. The axial compressive load was applied by a hydraulic strut and measured with an SR-4 load cell. The torsion load was applied by a hydraulic strut which was attached to the lower head by two cables. The torsion load was also measured by an SR-4 load cell.

The buckling loads of the test specimens were determined visually, which was a relatively simple task because the buckles often snapped into position. Occasionally, buckles appeared to grow out of relatively large initial irregularities. The order of application of the compression and torsion loads did not affect the magnitude of the critical stresses. A photograph of a typical buckle pattern in one of the specimens subjected to a combined load is shown in Fig. 1.

The test data are plotted in Fig. 2 in terms of the nondimensional stress ratios R_c and R_t. The stress ratios are defined as in Eq. 1, but the critical stresses are those obtained with internal pressure present. In order to plot the combined loads data, the average of the experimental buckling stresses for the cylinders loaded in compression alone and those loaded in torsion alone have been used as the denominators of the stress ratios. Shown in Fig. 2 is the interaction relationship defined by Eq. (1) which has been suggested for unpressurized cylinders. It can be observed that this interaction curve is a suitable lower bound to the test data. Based on these tests, it is concluded that the same shape design curve adequately describes the behavior of both pressurized and unpressurized circular cylinders under combined compression and torsion. For the design of pressurized cylinders, the stress ratios in Eq. (1) should be used with the critical buckling stress for pressurized cylinders under compression alone or under torsion alone determined from empirical curves.

It should be remembered that the above conclusions are based on tests of cylinders at only two values of the pressure parameter, $(p/E)\ (r/t)^2$. It is conjectured that the interaction curve would be the same for any long pressurized cylinder; however, additional tests should be performed to verify this assumption.

REFERENCES

[1] Fung, Y. C., and Sechler, E. E., *Buckling of Thin Walled Circular Cylinders Under Axial Compression and Internal Pressure*, Journal of the Aeronautical Sciences, Vol. 24, No. 5, pp. 351–356, May, 1957.

[2] Lo, H., Crate, H., and Schwartz, E. B., *Buckling of Thin-Walled Cylinders Under Axial Compression and Internal Pressure*, NACA TN 2021, January, 1950.

[3] Harris, L. A., Suer, H. S., Skene, W. T., and Benjamin, R. J., *The Stability of Thin-Walled Unstiffened Circular Cylinders Under Axial Compression Including the Effects of Internal Pressure*, Journal of the Aeronautical Sciences, Vol. 24, No. 8, pp. 587–596, August, 1957.

[4] Hopkins, H. G., and Brown, E. H., *The Effect of Internal Pressure on the Initial Buckling of Thin-Walled Circular Cylinders Under Torsion*, British Aero. Research Council R&M No. 2423, January, 1946.

[5] Crate, H., Batdorf, S. B., and Baab, G. W., *The Effect of Internal Pressure on the Buckling Stress of Thin-Walled Circular Cylinders Under Torsion*, NACA ARR L4E27, May, 1944.

[6] Batdorf, S. B., Stein, M., and Schildcrout, M., *Critical Combinations of Torsion and Direct Axial Stress for Thin-Walled Cylinders*, NACA TN 1345, June, 1947.

On Laminar Separation Bubbles

Kenneth R. Cramer
Aeronautical Research Engineer, Aeronautical Research Laboratory, WADC, ARDC, Wright-Patterson Air Force Base, Ohio

October 18, 1957

SYMBOLS

d	=	step height
l	=	bubble length
n	=	number of δ_s*
R_{δ_s}*	=	$U_a\delta_s$*/ν
U_a	=	free-stream velocity at reattachment
U_s	=	free-stream velocity at separation
x_a	=	distance from leading edge to reattachment
x_s	=	distance from leading edge to separation
α	=	angle of attack of airfoil
δ_a*	=	displacement thickness at reattachment
δ_s*	=	displacement thickness at separation
ν	=	kinematic viscosity

DISCUSSION

SINCE THE ADVENT of airfoil shapes having thin leading edges, attention has been focused on the attendant leading-edge separation bubbles since they may greatly affect the downstream boundary layer as well as the airfoil lift characteristics.

Owen and Klanfer,[1] based on the results of experimental investigations, presented a correlation of nondimensional bubble lengths with a Reynolds number based on the displacement thickness and the free-stream velocity at the separation point. They observed, from this correlation, that the bubble lengths divided into two general groups. The short "turbulent" type bubbles occurred for $R_{\delta_s}* > 500$ while the longer, "laminar" type occurred for $R_{\delta_s}* < 500$.

Due to the complex nature of these separation bubbles, only a limited number of incomplete theoretical descriptions have been published, for example, references 2 through 4. Thus, in an attempt to obtain a theoretical basis for Owen and Klanfer's correlation for laminar bubbles, a rather idealized model is postulated, (see Fig. 1).

It is assumed that the flow over this stepped flat plate is incompressible and the usual laminar boundary-layer assumptions are applicable. It is further assumed that for a small step height,

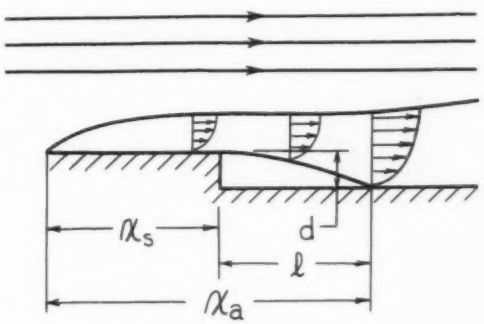

FIG 1. Stepped plate model.

TABLE 1
Laminar Bubble Lengths l/δ_s^*

n \ $R_{\delta_s^*}$	350	400	450	500
1	350	400	450	500
2	933	1066	1199	1333
3	1750	2000	2250	2500
4	2800	3200	3600	4000
5	4182	4666	5250	5833
6	5500	6400	7200	8000
7	7350	8400	9450	10500
8	9310	10666	12000	13333
9	11560	13200	14850	16500
10	14000	16000	18000	20000

NACA 64A-006

α	l/δ_s^*	$R_{\delta_s^*}$
5°	2144	401
5.5°	4990	312
6°	5440	393
7°	8800	406
8°	12890	378
9°	22980	389

the air in the bubble is stagnant and the flow downstream of the step and previous to attachment will be essentially a boundary-layer type flow. The growth of this viscous region is in the direction of the wall in the manner of a spreading jet. The free-stream velocity is assumed to be constant along the entire plate length.

With this model, the growth of the displacement thickness can be predicted on the basis of Blasius' results, Eq. (1).

$$\delta^* = 1.732\sqrt{\nu x/U} \tag{1}$$

Employing the definition of R_δ^* and Eq. (1) there results:

$$x_s/\delta_s^* = (1/3)R_{\delta_s^*}, \quad x_a/\delta_a^* = (1/3)R_{\delta_a^*}$$

Furthermore, since $l = x_a - x_s$ and with the above, one easily obtains Eq. (2).

$$l/\delta_s^* = (1/3)R_{\delta_s^*}[(\delta_a^*/\delta_s^*)^2 - 1] \tag{2}$$

Originally it was assumed that the separated viscous region grows in the wall direction, thus $\delta_a^* = \delta_s^* + d$ and letting $d = n\delta_s^*$ then $\delta_a^* = (n + 1)\delta_s^*$. Upon substitution of this relation into Eq. (2) the final equation results.

$$l/\delta_s^* = R_{\delta_s^*}\{[(n + 1)^2 - 1]/3\} \tag{3}$$

Values of l/δ_s^* for several $R_{\delta_s^*}$ and a range of n's are listed in Table 1 with the experimental results from reference 1, for comparison.

It is seen from these results that the bubble length grows with an increasing step height as did the bubble length in the experimental results for an increasing angle of attack. Direct comparisons cannot be made since in the experiments diffusion existed in the free stream which resulted in comparatively shorter bubbles. A more direct comparison might be made, however, if the analysis were based on the growth of the displacement thickness over a circular cylinder, for example.

It is also seen that the bubble length grows for an increasing $R_{\delta_s^*}$ in contrast to the decreasing lengths exhibited in reference 1 for the turbulent type bubbles. This result appears physically reasonable if one considers the flow over two plates of different initial length at the same free-stream velocity such that the separation displacement thicknesses are equal and only the viscosities are different, for example, due to a different temperature. In this case, a smaller kinematic viscosity, and thus a larger $R_{\delta_s^*}$, would tend to lengthen the separated region due to a decrease in the viscous growth in the wall direction. The turbulent bubble decreases with increasing $R_{\delta_s^*}$ due to the increase in turbulent diffusion of the viscous region.

While admittedly, this model is a simplification of the actual case, certainly such flows exist, and thus it would be interesting to test the validity of these results by suitable experiments. If reasonable agreement were ascertained, then it is possible that this type of boundary-layer analysis could be employed as the basis for attacking a more realistic but more difficult case. For example, one could employ a relation for the displacement thickness growth over a curved surface that approximates the free-stream velocity variation over a separated region.

REFERENCES

[1] Owen, P. R. and Klanfer, L., *On the Laminar Boundary Layer Separation from the Leading Edge of a Thin Airfoil*, Royal Aircraft Establishment Report No. Aero. 2508, October, 1953.

[2] Squire, H. B., *Note on the Motion Inside a Region of Recirculation (Cavity Flow)*, J. RAeS., Vol. 60, No. 543, pp. 203–205, March, 1956.

[3] Batchelor, G. K., *On Steady Laminar Flow, with Closed Streamlines at Large Reynolds Number*, Journal of Fluid Mechanics, Vol. 1, Part 4, October, 1956.

[4] Crabtree, L. F., *Effects of Leading-Edge Separation on Thin Wings in Two-Dimensional Incompressible Flow*, Journal of the Aeronautical Sciences, Vol. 24, No. 8, pp. 597–604, August, 1957.

An Authorized Binding for
Journal of the Aeronautical Sciences

Arrangements have been made by the Institute of the Aeronautical Sciences for members and subscribers to have their Journals bound carefully and economically. Simply write for details to:

Publishers' Authorized Bindery Service

5809 West Division St. Chicago 51, Ill.